SIMULATION OF HORIZONTAL WELL TESTS

by

Nasser S. AL-Mohannadi

A thesis submitted to the Faculty and Board of Trustees of the Colorado School of Mines in partial fulfillment of the requirements for the degree of Doctor of Philosophy (Petroleum Engineering).

Golden, Colorado

Date_______________

Signed: _________________________

Nasser S. Al-Mohannadi

Approved:________________

Dr. Erdal Ozkan

Thesis Advisor

Golden, Colorado

Date_______________

____

Dr. Craig W. Van Kirk

Professor and Head,

Department of Petroleum

Engineering

ABSTRACT

Well testing is one of the powerful tools to identify the features and properties of the reservoir, predict the future performance, and find ways to increase the ultimate recovery. Well-test results can be interpreted by using analytical well-test solutions for relatively simple reservoir architectures and well geometry. In more complex cases, numerical simulation can be used to compute the pressure-transient responses to match with the field test. The existing numerical simulation packages are for prediction purposes and long-time production periods. Therefore, these packages may not be suitable for well test purposes because of the unsteady pressure-transient behavior during the early period of the test.

The most difficult task of numerically simulating well-tests is the treatment of the bottom-hole flowing pressure. Because of the more complex geometry of the well and 3-D flow convergence, representing horizontal wells in grid blocks is a challenging task. Building models with conventional well indices need more grid refinements around the well with small time steps, which will increase the computational time. One remedy for this problem is to use the transient well indices.

Most analytical and numerical models used for pressure transient analysis consider slab reservoirs with straight horizontal wells. In reality, however the most common traps for hydrocarbons are anticlines or salt domes and the horizontal wells are not exactly straight but may be concave upward, concave downward, or undulating. Therefore, the overall objective of this Ph.D. research is to investigate the pressure-transient performance of horizontal wells with complex geometries in complex structures. The scenarios considered include straight horizontal wells in anticlinal structures and curved wells in horizontal slab reservoirs under single- and two-phase fluid flow conditions. In

order to accomplish this objective, an efficient numerical computation technique should be developed. This requires the improvement of the representation of horizontal wells in grid blocks.

Several tasks are involved in this development: (1) Generating three-dimensional, general numerical reservoir models for different reservoir and well structures, (2) incorporating existing techniques to represent horizontal wells in the reservoir, (3) investigating the application of transient well indices for horizontal wells, (4) documenting the effects of grid size and time step with different productivity indices, (5) studying the pressure-transient responses of horizontal wells in anticlinal structures and curved wells in horizontal slab reservoirs for single- and two-phase fluid flow.

The results of the study indicate that the conventional well index should be used with log-distributed grid and time steps to obtain closer match to the analytical solution at early times. It has been observed that there is a limit to grid refinement beyond which the results do not improve. On the other hand, transient well index with coarse grids improves the match with the analytical solution at early times. The use of the fine grid with transient well index, however, causes deviation from the analytical results. Because the modeling of the complex well and reservoir geometries considered in this study requires the use of finer grids, transient well index and conventional well index yield comparable results. Based on the results of the sensitivity runs, it is observed that the effect of the structure becomes noticeable at later times (linear flow and beyond) where both transient well index and conventional well index yield accurate simulations. Therefore, conventional well index with grid refinement is used in this study to investigate the pressure-transient performances.

It is shown that, in the absence of gas cap, conventional horizontal-well models may be used to approximate the flow characteristics of the systems where the trajectory of the well does not conform to the curvature of the producing structure. If a gas cap is present, however, the unconformity of the well trajectory and curvature of the producing layer manifests itself especially on derivative characteristics when the gas saturation increases around the well. In general, the most significant deviations from the conventional horizontal-well behavior are observed during the buildup periods following long drawdowns. In these cases, the pressure-transient analysis is complicated and requires detailed numerical modeling of the well and reservoir curvature in the vertical plane.

TABLE OF CONTENTS

LIST OF FIGURES

Page No.

LIST OF TABLES

Page No.

ACKNOWLEDGEMENTS

First, I would thank GOD for helping and giving me patience in this work. Also, I would like to express my genuine appreciation to Dr. Erdal Ozkan for his support and guidance, to Dr. Hossein Kazemi for his assistance and cooperation and to my other committee members for their collaboration.

This work is dedicated to my parents whom without their support, I would not be able to reach this far.

Dad and Mom thank you.

Chapter 1
INTRODUCTION

Identifying the properties and geological features of a reservoir is crucial to predict the future performance and find ways to increase the ultimate recovery. There are different ways and tools to obtain these parameters and properties. Well testing is one of the powerful tools.

The pressure-transient (early-time) response of a well is measured during a well test. The description of the field is obtained from the analysis of the well-test data based on the flow characteristics during the test. Conventional horizontal-well pressure-transient models assume that well is straight and parallel to the top and bottom boundaries of the reservoir. Horizontal wells, however, may not be straight and may be concave upward, concave downward, or undulating in predominantly horizontal strata. In addition, the structure of the reservoir may not be a horizontal slab but may be more complex like anticlines.

Reservoir engineers usually apply analytical well-test solutions to analyze the well-test results for relatively simple reservoir architectures. Analytical solutions, however, are not suitable for heterogeneous reservoirs with complex boundaries and well geometry. In these cases, numerical simulation may be the only way to compute the pressure-transient responses to match the field test. Numerical modeling also is needed to incorporate pressure-transient data into geostatistical modeling, which is widely used to fill in reservoir simulation grids.

A reliable and accurate representation of wells in numerical models is, therefore, essential to evaluate their pressure-transient responses and overall performances in heterogeneous reservoir. The most difficult task of numerical simulation of well tests is the treatment of the bottom-hole flowing (BHF) pressure. Standard finite-difference reservoir simulators use the Peaceman[1] well index called numerical productivity index (WI), which is based on the solution of single-phase, steady-state incompressible flow. Steady-state incompressible flow assumption is known to work reasonably well at later times for prediction runs when the pressure perturbation reaches several grid-blocks around the well. It is not valid for the early times of a well-test simulation.

There are two common approaches to solve this problem. One of these approaches is to use very fine grids around the well and extremely small time steps especially at early times. This approach is inefficient because of excessive computational times and increased potential of numerical errors. The second approach is to define a transient well index[2] (TWI) to replace Peaceman-type representation of wells in grid blocks. This approach has been shown to be accurate and efficient for vertical wells but very little information is available for horizontal wells. One of the major problems of defining a transient well index for horizontal wells is the need to account for various transient flow periods.

Therefore, the overall objective of the Ph.D. research is to model complex horizontal well geometries in complex structures and to improve numerical simulation for these systems. To clarify the terminology used in this study, we define a horizontal well as a borehole which has a predominantly horizontal orientation between its two tips. With this convention, wells that are concave upward, concave downward or undulating will be referred to as horizontal wells.

1.1 Objective of the Study

The main objective of this Ph.D. research is to investigate the pressure-transient responses of horizontal wells with complex geometries in complex structures. The investigation covers straight horizontal wells in anticlinal structures and curved wells in horizontal slab reservoirs under single- and two-phase fluid flow conditions.

An efficient numerical computation technique should be developed to achieve this objective. In addition, improvement of the presentation of wells in grid blocks and the appropriate selection of the time steps is needed for the simulation models.

Several Tasks are completed to accomplish this objective:

(1) Building three-dimensional, general numerical reservoir models for different reservoir and well structures using synthetic data.

(2) Applying existing techniques to represent horizontal wells in the reservoir.

(3) Examining the application of transient well indices (TWI) for horizontal wells.

(4) Documenting the effects of grid size and time step with different well indices on the pressure-transient behavior.

(5) Studying the pressure-transient responses of horizontal wells in anticlinal structures and curved wells in horizontal slab reservoirs for single- and two-phase fluid flow.

1.2 Literature Review

In this section an overview of pertinent literature is presented. The literature review is divided into four different categories to show the previous studies and researches that are related to the objective of this Ph.D. project.

1.2.1 Well and Reservoir Curvature

Several papers have considered different reservoir shapes in the context of horizontal wells; infinite slab,[3-9] cylinder,[10-11] rectangular parallelepiped,[10-13] vertical no-flow boundary at an arbitrary orientation.[12] The common assumption of these reservoir models is the flat top and bottom boundaries. Although the top and bottom boundaries strongly influence the pressure-transient characteristics of horizontal wells,[3-5,14] the effect of the curvature of these boundaries, as in anticlines and domes, has not been discussed in the literature.

The curvature of horizontally oriented wells has not attracted much attention in the pressure-transient analysis literature. Likewise, the curvature of the top and bottom boundaries has not been discussed. Specifically, two studies addressed this issue. Azar-Nejad et al.[15] studied a curved well which was a quarter of a circle (from vertical to horizontal) in a slab reservoir. They concluded that the pressure-transient response of the curved well could not be approximated by that of a straight horizontal well of equal drilled length especially in anisotropic reservoirs. On the other hand, they did not address the issue of effective well length and the effect of the aspect ratio (the ratio of the distance from the well to the closest boundary and thickness of the formation).

Another common problem for horizontal wells, undulations was addressed by Goktas and Ertekin.[16] They showed that undulations might influence the characteristics of pressure-transient responses when the vertical window of undulations becomes comparable to the formation thickness. For practical windows of unintentional undulations, however, the pressure-transient responses could be closely approximated by that of a straight horizontal well. It must be mentioned that the conclusions of Goktas and Ertekin,[16] were different from that of Azar-Nejad et al.[15] The difference was because of the different definitions of horizontal well length in these two studies. To compare undulating and straight wells, Ref. 15 used the total drilled length whereas Ref. 16 used the straight distance between the tips.

1.2.2 Existence of a Gas Cap

Another issue that has not been sufficiently discussed in the literature is the analysis of horizontal-well pressure-transient responses in the presence of a gas cap. Based on buildup test data of fractured, vuggy, carbonate reservoirs that have large gas caps, Fleming et al.[17] and Fleming et al.[18] have noted that the existence of a gas cap would cause oscillations on the derivatives of pressure buildup responses of horizontal wells. Numerical studies were conducted also to support their arguments.

1.2.3 Representation of Wells in Grid Blocks

In the literature, several papers have conducted different studies to improve the numerical simulation of well tests. They considered the issue of the treatment of bottom-hole flowing (BHF) pressure, the productivity index with steady state assumption, and improper treatment of the wellbore flow and reservoir-wellbore interaction. The existing literature mainly shows the implementation of a local grid refinement method into a three-dimensional simulator to model flow performances of wells. Transient well index for numerical well test analysis was also discussed in the literature. Most of these studies are concerned with vertical wells. Below an account of the relevant literature is given.

Peaceman[1] showed that integration over a circle with an area equal to that of the block (assuming negligible r_w) gives the average pressure,

$$\bar{p} = p_{wf} + \frac{141.2qB\mu}{2\pi kh}\left[ln\frac{r_b}{r_w} - \frac{1}{2}\right], \tag{1-1}$$

where $\Delta x = \Delta y$ and

$$r_b = \frac{\Delta x}{\sqrt{\pi}}. \tag{1-2}$$

Peaceman[1] also concluded that steady state well block pressure P_b computed by a square grid-block system is the same as that for a dummy well of radius r_o given by $r_0 = 0.198 \times \Delta L$. This is for a vertical well produced at constant flow rate. It is shown also that the BHF pressure can be obtained using a conventional well index (WI) according to

$$p_{wf} = p_0 - \frac{q}{WI}, \tag{1-3}$$

where p_o is the grid block pressure, p_{wf} is the BHF pressure, q is the well flow rate and

$$WI = \frac{2\pi \times \Delta z_i k}{\mu \, ln\left(\frac{r_w \times e^{-s}}{r_0}\right)} . \tag{1-4}$$

Peaceman[1] showed when pseudo-steady state flow regime is reached near the well, r_0 can be given by

$$r_0 = \Delta L\left[4t_D \, exp\left(-\gamma - 4\pi p_{Db}\right)\right] \tag{1-5}$$

where γ is Euler's constant,

$$t_D = \frac{k}{\phi \mu c_t \Delta L^2} \times t , \tag{1-6}$$

and

$$p_D = \frac{kh}{q\mu} \times p . \tag{1-7}$$

Peaceman[19] derived an equivalent wellbore radius for an isotropic reservoir and non-square grid blocks. The equivalent wellbore radius formula is given by

$$r_0 = 0.14\left(\Delta x^2 + \Delta y^2\right)^{\frac{1}{2}} . \tag{1-8}$$

He showed that the equivalent radius of a wellblock for a horizontal well in an anisotropic reservoir should be given by

$$r_0 = 0.28 \frac{\left[\left(\frac{k_y}{k_z}\right)^{\frac{1}{2}} (\Delta z)^2 + \left(\frac{k_z}{k_y}\right)^{\frac{1}{2}} (\Delta y)^2\right]^{\frac{1}{2}}}{\left[\left(\frac{k_y}{k_z}\right)^{\frac{1}{4}} + \left(\frac{k_z}{k_y}\right)^{\frac{1}{4}}\right]} . \tag{1-9}$$

This formula assumes non-square grid blocks and the well is not located near any grid boundary.

Babu et al.[20] determined the equivalent radius of a wellblock for horizontal wells. The following form of equivalent wellblock radius equation was obtained by using the graphical methods with curve fitting techniques applied to their analytical solution.

$$r_0 = (0.14)(k_y k_z)^{\frac{1}{4}} \left[\frac{\Delta y^2}{k_y} + \frac{\Delta z^2}{k_z} \right]^{\frac{1}{2}} \times \left[\frac{1 + exp\left(2.215 - 3.88 \dfrac{n_y n_z}{\alpha}\right)}{1 + 0.533\left(\dfrac{\alpha}{n_z}\right)} \right], \tag{1.10}$$

where

$$\alpha = \left(\frac{\Delta y}{\Delta z}\right) \sqrt{\frac{k_z}{k_y}} \,. \tag{1.11}$$

Ding et al.[21-23] proposed a new method for improving the well modeling in nonstandard configurations such as nonuniform Cartesian grids, flexible grids, and off-center wells. Their main objective is to improve the flow representation around the well by modifying the transmissibility in the near-well region. They used the following transmissibilities instead of the conventional ones for homogenous and isotropic reservoir: (see Fig. 1-1)

$$T_{eq,i} = k \Delta z_i \frac{\Delta y_0}{L_{eq,i}}, \tag{1-12}$$

with

$$L_{eq,i} = \Delta y_0 \frac{ln\left(\dfrac{\Delta x_{1/2}}{r_0}\right)}{\theta_i} \,. \tag{1-13}$$

for $i = 1$ and 3, and

$$T_{eq,i} = k \Delta z_i \frac{\Delta x_0}{L_{eq,i}}, \tag{1-14}$$

with

$$L_{eq,i} = \Delta x_0 \frac{ln\left(\frac{\Delta x_{1/2}}{r_0}\right)}{\theta_i}. \tag{1-15}$$

for $i = 2$ and 4.

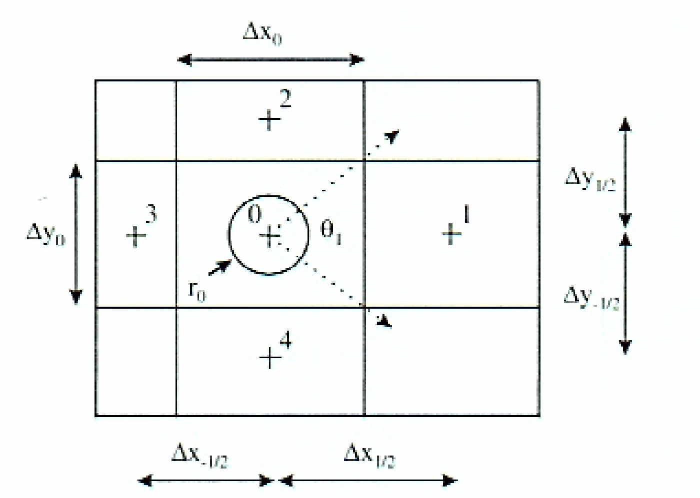

Figure 1- 1. Well-block pressure calculation (Corrected Transmissibility Method).

Goktas and Ertekin[24] described the implementation of a local grid refinement method into three-dimensional simulators to model flow performances of horizontal wells. The constructed model does not utilize an equivalent wellblock radius as used in a conventional wellbore model, but utilizes the residual equation to determine the flow into the well. They showed the local grid refinement (LGR) methodology that can couple circular and non-circular well architectures into numerical models. The coarse blocks that include wells are locally refined in all three dimensions. Fine and coarse grids are coupled at the interface of two grid systems.

G. Blanc et al.[2] presented the correction to the Peaceman Ei function. Derivation of a transient numerical productivity index (TNPI) for the Cartesian grids was done to correct the early-time problem due to the use of the steady state numerical productivity index

(NPI). This is accomplished by using an unsteady state radial flow equation between r_o and r_w to compute the numerical productivity index (TWI) as follows:

$$TWI = \frac{4\pi \times \Delta z_i k}{E_i\left(-\frac{r_0^2}{4kt}\right) - E_i\left(-\frac{r_w^2}{4kt}\right)}. \tag{1-16}$$

This correction is based on pseudo-steady state approximation of the transient flow equation corresponding to a pseudo steady state flow regime around the well. For more accuracy, they showed the full TNPI solution with r_o which is obtained by using the Newton's method of solution. The corrected transmissibility and accumulation term (CTAT) in the flow equation was also derived by G. Blank et al.[2] to improve the steady-state transmissibility multiplier. This should account for the short time period when the well flow rate is essentially from the well block by volume storage. This is given by

$$c_t \phi \int_{v_o} \frac{\partial p}{\partial t} dV, \tag{1-17}$$

so that

$$\frac{\partial p_o}{\partial t} = -\frac{q\mu}{4\pi kh} \frac{e^{-\frac{r_0^2}{4kt}}}{t}. \tag{1-18}$$

Archer and Horne[25] explored the advantages of a hybrid boundary element method known as the Green element method for modeling pressure-transient tests. These methods are based on Green's functions, which are an established part of well test analysis. They presented formulations, which give computationally efficient means to handle heterogeneity.

Vicente et al.[26] developed a fully implicit, three dimensional simulator with local refinement around the wellbore to solve reservoir and horizontal well flow equations simultaneously for single-phase liquid and gas cases. They used a numerical model coupling reservoir and horizontal well flow dynamics for the transient behavior which are pressure continuity and mass balance at the sandface. They introduced the problem encountered with infinite-conductivity idealization of horizontal wellbore.

Archer and Yildiz[27] proposed a transient well index for the numerical simulation of well tests. They compared their results and Peaceman's well index to analytical well test solutions. They assumed that the well block pressure is representative of the average well block pressure for the proposed well index formulation. This is computed directly from the solution for infinite acting radial flow. The model is derived in terms of dimensionless pressure, distance and time given below.

$$p_D(r_D, t_D) = \tfrac{1}{2} Ei\left(-\frac{r_D^2}{4t_D^2}\right), \tag{1-19}$$

where

$$p_D = \frac{kh}{141.2 qB\mu}(p_i - p_{wf}), \tag{1-20}$$

$$t_D = \frac{0.000264 kt}{\phi\mu c_t r_w^2}, \tag{1-21}$$

and

$$r_D = \frac{r}{r_w}. \tag{1-22}$$

They addressed the model in which the grid block pressure is taken to be the analytically determined average pressure. Therefore,

$$q = WI(\overline{p}^B - p_{wf}), \tag{1-23}$$

where

$$\overline{p}^B = \frac{4\int_1^{\frac{x_D^B}{2}}\int_1^{\frac{y_D^B}{2}}\int_{t_D^1}^{t_D^2} \tfrac{1}{2} Ei\left(-\frac{r_D^2}{4t_D}\right) dt_D\, dx_D\, dy_D}{(x_D^B y_D^B - \pi r_{wD}^2)(t_D^2 - t_D^1)}. \tag{1-24}$$

The well index can then be calculated from

$$WI = \frac{kh}{141.2\mu B}(\overline{p}_D^B - p_{D,wf})\ . \tag{1-25}$$

These equations are for an isotropic reservoir. The following equations are for anisotropic:

$$p_D\left(r_D^{'}, t_D\right) = \tfrac{1}{2} Ei(-\frac{r_D^{'2}}{4t_D})\ , \tag{1-26}$$

where

$$t_D = \frac{\sqrt{k_x k_y}\, t}{\phi\mu c_t r_w^2}\ , \tag{1-27}$$

$$r_D^{'} = \sqrt{\left(x_D \times C\right)^2 + \left(y_D / C\right)^2}\ , \tag{1-28}$$

and

$$C = \left(\frac{k_y}{k_x}\right)^{\frac{1}{4}}\ . \tag{1-29}$$

The average grid block pressure is given by

$$\overline{p}^B = \frac{4 \int_1^{\frac{x_D^B \times C}{2}} \int_1^{\frac{y_D^B}{2\times C}} \int_{t_D^1}^{t_D^2} \tfrac{1}{2} Ei(-\frac{r_D^2}{4t_D}) dt_D dx_D dy_D}{(x_D^B y_D^B - \pi r_{wD}^2)(t_D^2 - t_D^1)}\ . \tag{1-30}$$

The well index is then calculated in the same manner as before.

1.2.4 Horizontal Well Pressure-Transient Models

Several studies have been done to develop the standard models of horizontal well pressure-transient analysis during the 1980's.[3-8,12] The solution to the pressure-transient response of horizontal well using instantaneous source functions will be discussed in detail in Chapter 2. A summary of the literature on horizontal well pressure-transient models is provided below.

Clonts and Ramey[3] derived an analytical solution for the pressure-transient response of horizontal drainhole in an anisotropic and finite thickness reservoir for infinite-conductivity and uniform-flux. They showed the solution for the multiple drainholes and developed the pseudo skin factor.

Ozkan et al.[4] showed the analysis of the pressure-transient behavior of a horizontal well by considering the mathematical model that is identical to that examined in Ref.3 for infinite-conductivity and uniform-flux. Pseudoskin factors were considered and based on the vertically fractured well solution. They showed the comparison of the performances between horizontal wells and fully penetrating vertical fractures.

Goode and Thambynayagam[5] presented an analytical solution for drawdown and buildup pressure-transient response analysis of horizontal wells located in homogenous and anisotropic semi-infinite medium. The solution was derived by solving the three-dimensional diffusion equation with successive integral transforms. The analysis methods for the pressure drawdown and buildup data were shown.

Carvalho and Rosa[6] developed mathematical model to evaluate the pressure-transient behavior in a well with an infinite conductivity horizontal drainhole. It was obtained by applying the instantaneous sources and Green's functions. Uniform-flux was discussed and the pressure at the wellbore face was calculated. They showed that it is not true to evaluate the pressure for the infinite-conductivity case with uniform-flux model at a fixed point along the wellbore.

Kuchuk et al.[7] presented the analytical solution for the pressure-transient responses with and without gas cap or aquifer. They showed an interpretation method of horizontal well test data and the analyses of pseudosynthetic and real well test data.

Kuchuk et al.[8] showed new analytical solution in real time and as Laplace transforms for horizontal wells bounded by top and bottom horizontal boundary planes. No flow and constant pressure boundary conditions were considered. They included the skin and wellbore storage effects to the laplace transform pressure solution. The solution was based on uniform-flux and can be approximated to the infinite-conductivity. The pressure response at the well was estimated by average pressure along the well length rather than by using an equivalent pressure point.

Daviau et al.[12] described the simplest and most significant analytical approach for pressure-transient response of a horizontal well with uniform-flux. They presented applicable approach to most real cases by taking into account the wellbore storage, skin and the boundary effect of the reservoir. The interpretation method and the horizontal well test design were shown.

1.2.5 Wellbore Hydraulics

In the literature, several researches have been done to study the effect of pressure drop in the horizontal well on horizontal well responses and production performance. Below a summary of previous studies on the effect of wellbore hydraulics on horizontal well performance are shown.

Dikken[28] investigated the effect of pressure drop in the horizontal well on the production performance. He included the well pressure gradient in the horizontal well flow design. A simple analytical method that links single-phase well flow to turbulent stabilized reservoir flow was used in this study. They solved the second-order differential equation numerically for the appropriate boundary conditions.

Suzuki[29] discussed the influence of wellbore hydraulics within the horizontal section on horizontal well responses. He applied the semi-analytical method to obtain the finite-conductivity solution. The approximation of infinite- to finite- conductivity solutions was presented at downstream end of wellbore.

Sarica et al.[30] studied the effect of wellbore hydraulics on pressure behavior and productivity of horizontal gas wells. They used semi-analytical model that couples gas flow in the reservoir and in the wellbore to investigate the pressure and flux distributions along the well. The pressure losses in the horizontal section of the well was shown to be a composed of friction and acceleration losses and need to be considered in modeling horizontal gas wells.

Ozkan et al.[31] studied the effect of pressure drop in the horizontal section of wellbore on horizontal well pressure-transient. The semi-analytical model that couples wellbore and reservoir hydraulics was used to investigate the flux and pressure distributions along the length of the well. They presented the short- and long- term characteristics of pressure responses along the asymptotic. The detailed solution will be presented in Chapter 2.

Ozkan et al.[32] studied the effect of wellbore pressure drop on horizontal well productivity. Semi-analytical model was used to determine the optimum well length, wellbore diameter, and production rate. They discussed the model of real gases and showed that pressure losses due to acceleration in the wellbore hydraulics of horizontal gas wells should not be ignored.

Chapter 2
HORIZONTAL WELL PRESSURE ANALYSIS

Horizontal wells display more complex flow characteristics from that of vertical wells. This is due to the three dimensional fluid flow and the wellbore hydraulics in the horizontal wells which are reflected by the characteristics of the pressure responses. Therefore, more information is required for horizontal wells to evaluate the performance and productivity forecast.

One of the approaches to interpret the well-test results is to use analytical solutions. Analytical solutions, however, can only be used for simple reservoir architectures. Numerical models may be constructed, but these models are also calibrated by using the analytical models to model more complex architectures and heterogeneous reservoirs. Different analytical solutions have been derived in the literature. In this chapter, the line-source solution for the pressure-transient distribution is given. This solution will be used to compare with the numerical simulation results which will be shown in Chapters 4 and 5 (Well indices and grid structures for horizontal wells, and Results and Discussions, respectively).

2.1 Horizontal Well Transient Pressure Solution

The purpose of the well test is to determine the reservoir properties from the analysis of the record of the pressure change in the wellbore as a function of time. The characteristics of the pressure responses are compared with those of theoretical responses during the analysis. The solution of the diffusion equation given below is used to obtain the theoretical responses.

$$\vec{\nabla} \cdot \left(\frac{\vec{\vec{k}}}{\mu} \vec{\nabla} p \right) = \phi c_t \frac{\partial p}{\partial t} \,. \tag{2-1}$$

Appropriate Initial and boundary conditions are required for the solution of the above equation. The initial condition is equal to the constant p_i, in the entire reservoir. During the infinite acting period, the outer boundary condition is equal to initial pressure. The top and bottom boundaries of the formation affect the horizontal well response during the early-time period. The top and bottom boundaries are assumed to be horizontal planes and there is no flow through these boundaries. Although various production conditions can be applied for the well tests, constant rate production condition is used as the fundamental case. In general, the solutions of the diffusion equation in general are expressed in dimensionless form in order not to be modified every time the properties of the fluid and reservoir change. The following dimensionless variables will be used in this chapter.

$$p_D\left(x_D, y_D, z_D, z_{wD}, L_D, t_D\right) = \left(\frac{kh}{141.2 qB\mu} \right) \left[p_i - p\left(x, y, z, z_w, L_h, t\right) \right], \tag{2-2}$$

and

$$t_D = \frac{0.001055 kt}{\phi c_t \mu L_h^2} \,. \tag{2-3}$$

The dimensionless length and area are shown below respectively.

$$L_D = \left(\frac{L_h}{2h} \right) \sqrt{\frac{k_z}{k}} \,, \tag{2-4}$$

$$A_D = \frac{4A}{L_h^2} \,, \tag{2-5}$$

where

$A = \pi r_e^2$ or $A = x_e y_e$, and

$$t_{AD} = \frac{t_D}{A_D} \,. \tag{2-6}$$

The following relations for l_D, z_{wD} and r_{wD} are presented below:

$$l_D = \left(\frac{2l}{L_h}\right)\sqrt{\frac{k}{k_l}}\,, \tag{2-7}$$

where $l = x$ or y, and

$$z_{wD} = \frac{z_w}{h}\,, \tag{2-8}$$

$$r_{wD} = \frac{r_{w,eq}}{h}\,, \tag{2-9}$$

where

$$r_{w,eq} = \frac{r_w}{2}\left[\left(\frac{k_y}{k_z}\right)^{\frac{1}{4}} + \left(\frac{k_z}{k_y}\right)^{\frac{1}{4}}\right]. \tag{2-10}$$

2.1.1 Analytical Solution for Infinite-Conductivity Horizontal Wells

Consider the horizontal well shown in Fig. 2.1 in a closed reservoir with rectangular boundaries.

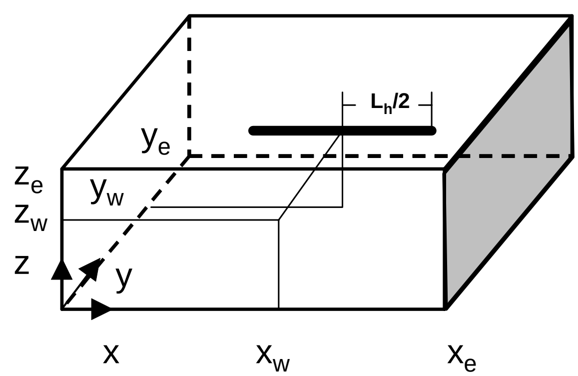

Figure 2- 1. Schematic of horizontal well.

The analytical solution for this horizontal well is given by[11]:

$$\overline{p}_D = \overline{p}_{fD} + \overline{F}_1 \tag{2-11}$$

where

$$\bar{p}_{fD}\left(x_D, y_D\right) = \frac{\pi}{x_{eD} s}\left(\begin{aligned} & \frac{\cosh\sqrt{u}\,\bar{y}_{D1} + \cosh\sqrt{u}\,\bar{y}_{D2}}{\sqrt{u}\sinh\sqrt{u}\,y_{eD}} \\ & + \frac{2x_{eD}}{\pi}\sum_{k=1}^{\infty}\frac{1}{k}\sin k\pi\frac{1}{x_{eD}}\cos k\pi\frac{x_{wD}}{x_{eD}}\cos k\pi\frac{x_D}{x_{eD}} \\ & \times\frac{\cosh\varepsilon_k\tilde{y}_{D1} + \cosh\varepsilon_k\tilde{y}_{D2}}{\varepsilon_k\sinh\varepsilon_k y_{eD}} \end{aligned}\right), \qquad (2\text{-}12)$$

is the fully penetrating vertical fracture solution where

$$\varepsilon_k = \sqrt{u + k^2\pi^2 / x_{eD}^2}\ , \qquad (2\text{-}13)$$

$$\bar{y}_{D1} = y_{eD} - \left|y_D - y_{wD}\right|\ , \qquad (2\text{-}14)$$

and

$$\bar{y}_{D2} = y_{eD} - \left(y_D + y_{wD}\right). \qquad (2\text{-}15)$$

The pseudoskin function $\overline{F}_1$ is shown below.

$$\begin{aligned} \overline{F}_1 = & \frac{2\pi}{x_{eD} s}\sum_{n=1}^{\infty}\cos n\pi z_D\cos n\pi z_{wD}\frac{\cosh\varepsilon_n\tilde{y}_{D1} + \cosh\varepsilon_n\tilde{y}_{D2}}{\varepsilon_n\sinh\varepsilon_n y_{eD}} \\ & + \frac{8}{s}\sum_{n=1}^{\infty}\cos n\pi z_D\cos n\pi z_{wD} \\ & \times\sum_{k=1}^{\infty}\frac{1}{k}\sin k\pi\frac{1}{x_{eD}}\cos k\pi\frac{x_{wD}}{x_{eD}}\cos k\pi\frac{x_D}{x_{eD}} \\ & \times\frac{\cosh\varepsilon_{k,n}\tilde{y}_{D1} + \cosh\varepsilon_{k,n}\tilde{y}_{D2}}{\varepsilon_{k,n}\sinh\varepsilon_{k,n} y_{eD}} \end{aligned}\ , \qquad (2\text{-}16)$$

where

$$\varepsilon_n = \sqrt{u + n^2\pi^2 L_D^2}\ , \qquad (2\text{-}17)$$

and

$$\varepsilon_{k,n} = \sqrt{u + k^2\pi^2 / x_{eD}^2 + n^2\pi^2 L_D^2}\ . \qquad (2\text{-}18)$$

This solution assumes that the flux is distributed uniformly along the well length (uniform-flux assumption). Infinite-conductivity solution, which assumes negligible wellbore pressure drop compared to reservoir pressure drop, can be approximated by substituting $x_D = 0.732$ into Eq. 2.11.[4]

Figure 2-2 shows the Diagnostic plot of the infinite-conductivity case for boundary-dominated flow that is generated by the above analytical solution. This case will be used to check and compare with the results generated by numerical simulation. Four different flow regimes are shown in the Fig. 2-2, early-time radial flow followed by intermediate-time linear flow, pseudo-radial flow and boundary dominated flow when the responses reach the boundary. These flow regimes will be discussed in detail in Section 2.2 (Horizontal Well Flow Characteristics).

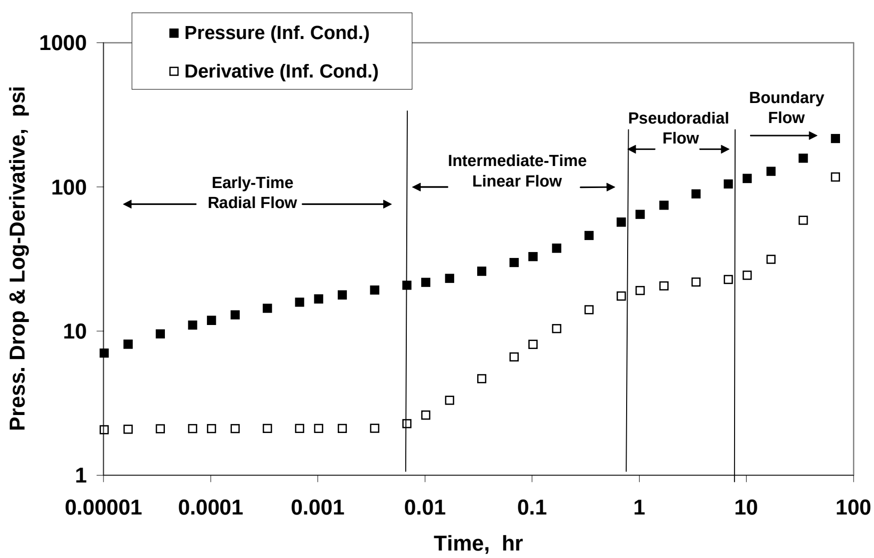

Figure 2- 2. Diagnostic plot – Infinite-conductivity for boundary-dominated flow.

2.1.2 Analytical Solution for Finite-Conductivity Horizontal Wells

In the presence of small reservoir drawdown and relatively high wellbore pressure drop, the well behaves like a finite-conductivity conduit. The well conductivity is a function of the dimensionless C_{hD}, and the Reynolds Number at the heel of the well, N_{Ret}. These parameters are defined as follows[31]:

$$C_{hD} = 7.395 \times 10^{13} \frac{r_w^4}{khL_h}, \tag{2-19}$$

and

$$N_{\mathrm{Re}_t} = 6.157 \times 10^{-2} \frac{\rho q}{\mu r_w}. \tag{2-20}$$

The analytical model used to obtain the finite-conductivity solution is shown below.[31]

$$p_{wD}(t_D) - p_D(x_D, r_{wD}, t_D) = \frac{N_{\mathrm{Re}_t} f_t}{16} \frac{\pi}{C_{hD}} \left(x_D - \int_{0+}^{x_D} \int_{0+}^{x'_D} \frac{D}{N_{\mathrm{Re}_t} f} q_{hD} dx''_D dx'_D \right), \tag{2-21}$$

where, for infinite-acting period,

$$\begin{gathered} p_D(x_D, r_{wD}, t_D) = \frac{1}{4} \int_0^{t_D} \int_{-1}^{+1} q_{hD}(\alpha, t'_D) \exp\left[-\frac{(x_D - \alpha)^2}{4(t_D - t'_D)} \right] d\alpha \\ \left\{ 1 + 2\sum_{n=1}^{\infty} \exp\left[-n^2 \pi^2 L_D^2 (t_D - t'_D) \right] \cos\left[n\pi (z_{wD} + r_{wD}) \right] \cos(n\pi z_{wD}) \right\} \frac{d\tau}{(t_D - \tau)}. \end{gathered} \tag{2-22}$$

Equation 2-21 can be written in the form of

$$p_{wD}(t_D) - p_D(x_D, r_{wD}, t_D) = \frac{\pi}{C_{hD}} \left(x_D - \int_{0+}^{x_D} \int_{0+}^{x'_D} q_{hD} dx''_D dx'_D \right), \tag{2-23}$$

for laminar flow in the wellbore ($N_{\mathrm{Re}} \le 2300$, $f = 16/N_{Re}$ and $D = 16$).

The flow in the entire wellbore is laminar when the pressure responses become independent of the Reynolds number for $N_{\mathrm{Re}_t} \le 2300$. Figure 2-3 shows the Diagnostic plot of the infinite-conductivity case for boundary dominated flow and finite-conductivity for infinite acting period that are generated by analytical solution. This figure will be checked and compared with the results generated by numerical simulation. It can be seen in the figure that as conductivity increases and the Reynolds number decreases, the pressure drop decreases and the responses approach infinite-conductivity. On the other hand, long horizontal well length with small wellbore radius and high production rate will be more under the finite-conductivity effects with higher pressure drop.

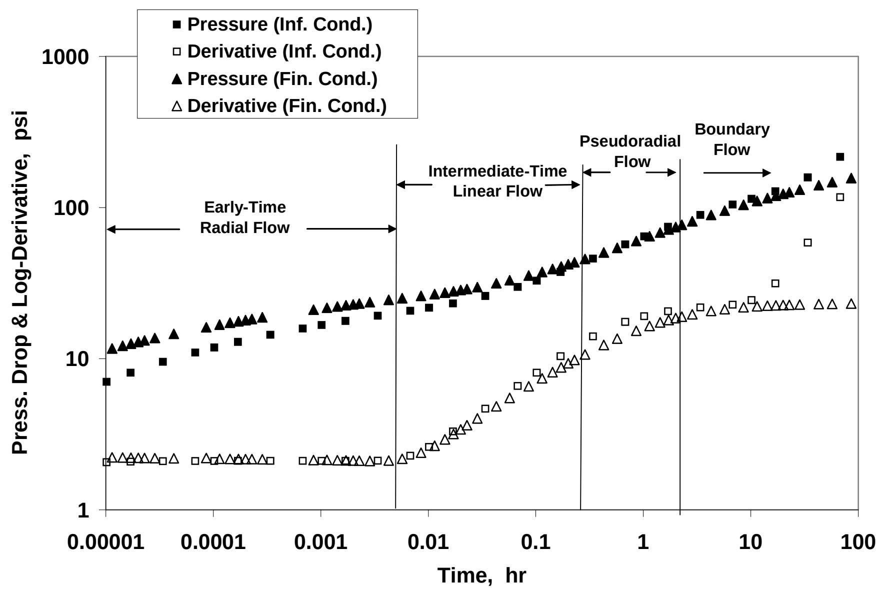

Figure 2- 3. Diagnostic plot – Infinite- and finite- Conductivity for boundary-dominated and infinite-acting flow period respectively.

The effect of a skin zone around the well should be included in the analytical solutions as follows[33]:

$$p_{hD}(x_D, t_D) = p_D(x_D, r_{wD}+, z_{wD}, t_D) + q_{hD}(x_D, t_D)s(x_D), \tag{2-24}$$

where

$$q_{hD} = \frac{q_h(x,t)L_h}{q} = \frac{L_h\sqrt{k_w k_z}}{141.2qB\mu}\left(\tilde{r}\,\frac{\partial p}{\partial \tilde{r}}\right)_{\tilde{r}=r_{w,x}}, \tag{2-25}$$

and

$$s(x_D)=\frac{\Delta p_s(x,t)}{\frac{L_h\sqrt{k_w k_z}}{hk}\left(\tilde{r}\frac{\partial p}{\partial \tilde{r}}\right)_{\tilde{r}=r_{w,x}}}=\frac{\frac{kh}{141.2qB\mu}\Delta p_s(x,t)}{q_{hD}(x_D,t_D)}\,. \tag{2-26}$$

where $\tilde{r}$ is the radial coordinate in the vertical plane (y-z) normal to the axis of the well and

$$k_w=\sqrt{k_y k_z}\ . \tag{2-27}$$

A skin factor of the horizontal s_m and vertical wells s_{mv} are defined below to address the effect of the mechanical damage around the well:

$$s_m=\frac{\sqrt[3]{k_x k_y k_z}\,h}{\sqrt{k_y k_z}\,L_h}s_{mv}\,. \tag{2-28}$$

A higher pressure drop should be observed with the existence of the skin around the well as shown in Fig. 2-4.

Wellbore with finite volume can store and unload compressible fluids which cause a wellbore storage effects. The wellbore loading/ unloading rate is

$$q_{wb}=-\frac{24C}{B}\frac{dp_{wf}}{dt}\,, \tag{2-29}$$

where the wellbore storage coefficient is

$$C=\frac{dV_w}{dp}\,, \tag{2-30}$$

and the production rate at the surface is defined as

$$q=q_{sf}+q_{wb}\,, \tag{2-31}$$

where q_{sf} = sandface rate.

A log-log plot of Δp_{wf} vs. t (Fig.2-4) should yield a unit-slope line during the wellbore storage dominated flow.

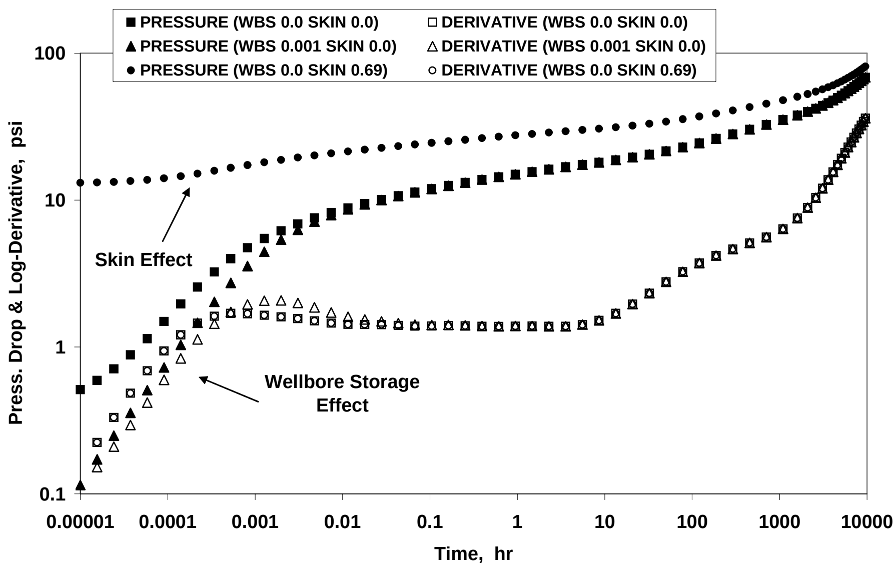

Figure 2- 4. Diagnostic plot for skin and wellbore storage effects.

2.2 Horizontal Well Flow Characteristics

Different flow characteristics are displayed by a horizontal well depending on the shape of the reservoir, orientation of horizontal well, boundary conditions, and the well length. The flow is divided into two regimes: infinite acting flow regimes and boundary flow regimes. The reservoir parameter estimation is obtained during the infinite acting flow regimes whereas productivity estimate and production forecast is calculated during the boundary dominated flow regimes.

A. Infinite-acting Flow regimes:

(i) Early-time radial flow

At early-time, flow converges toward a horizontal well only in the vertical (y-z) plane normal to the axis of the well as shown in Fig.2-5. Fig. 2-3 shows a constant derivative in the diagnostic plot during early-time radial flow.

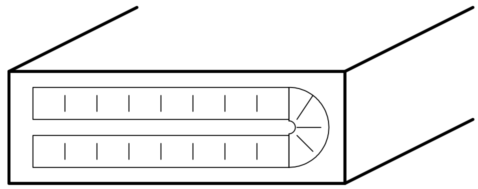

Figure 2- 5. Early-time radial flow, ETRF.

The expression for the early-time radial flow regime is given by:

$$\Delta p_{wf} = \frac{162.6 qB\mu}{\sqrt{k_y k_z} L_h}\left(\log t + \log \frac{\sqrt{k_y k_z}}{\phi c_t \mu r_{w,eq}^2} - 3.23 + \frac{\sqrt{k_y k_z} L_h}{kh} s \right), \tag{2-32}$$

where S is the mechanical skin factor of the horizontal well.

Semi-log plot (Fig. 2-6) of early-time pressure drawdown with respect to time displays a straight line with slope given by

$$m_{er} = \frac{162.6 qB\mu}{\sqrt{k_y k_z} L_h} \tag{2-33}$$

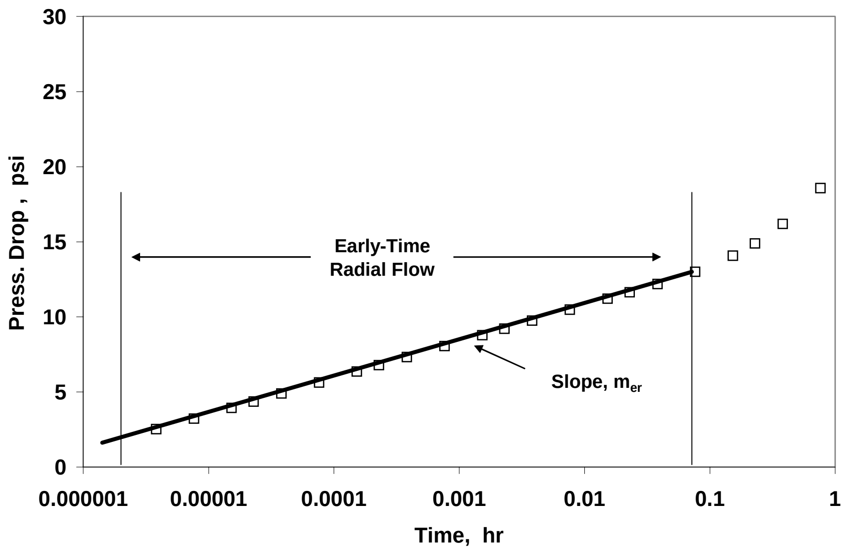

Figure 2- 6. Early-time semi-log analysis.

The skin factor may be determined from the semi-log straight line by using the following relation:

$$s = \frac{1.151kh}{\sqrt{k_y k_z} L_h} \left(\frac{\Delta p_{wf}}{m_{er}} - \log t - \log \frac{\sqrt{k_y k_z}}{\phi c_t \mu r_{w,eq}^2} + 3.23 \right) \tag{2-34}$$

(ii) Intermediate-time linear flow

Linear flow regime in the horizontal (x-y) plane at intermediate-times can be displayed for a long horizontal well in a formation with high vertical permeability. The linear flow starts when the convergence of flow across the tips of the well has not started when the influence of the top and the bottom boundaries becomes evident as seen in Fig.2-7. Figure 2-3 shows the derivatives in diagnostic plot should display a straight line with a slope equal to ½ during the intermediate linear flow.

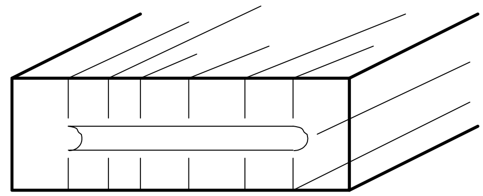

Figure 2- 7. Intermediate -time linear flow, ITLF.

This flow regime is expressed by:

$$\Delta p_{wf} = \frac{8.128 qB\mu}{L_h h\sqrt{\phi c_t \mu k_y}}\sqrt{t} + \frac{141.2 qB\mu}{L_h\sqrt{k_y k_z}}\left(s_{z+} s\right) \tag{2-35}$$

where

$$s_z = \ln\left(\frac{h}{r_{w,eq}}\right) + 0.25\ln\left(\frac{k_y}{k_z}\right) - \ln\left(\sin\frac{\pi z_w}{h}\right) - 1.838 \tag{2-36}$$

is a pseudoskin term caused by partial penetration in the vertical plane.

The cartesian plot of Δp_{wf} vs. $\sqrt{t}$ shown in Fig. 2-8 during this flow period displays a straight line with slope given by

$$m_{il} = \frac{8.13 qB\sqrt{\mu}}{\sqrt{\phi c_t k_y} L_h h} \tag{2-37}$$

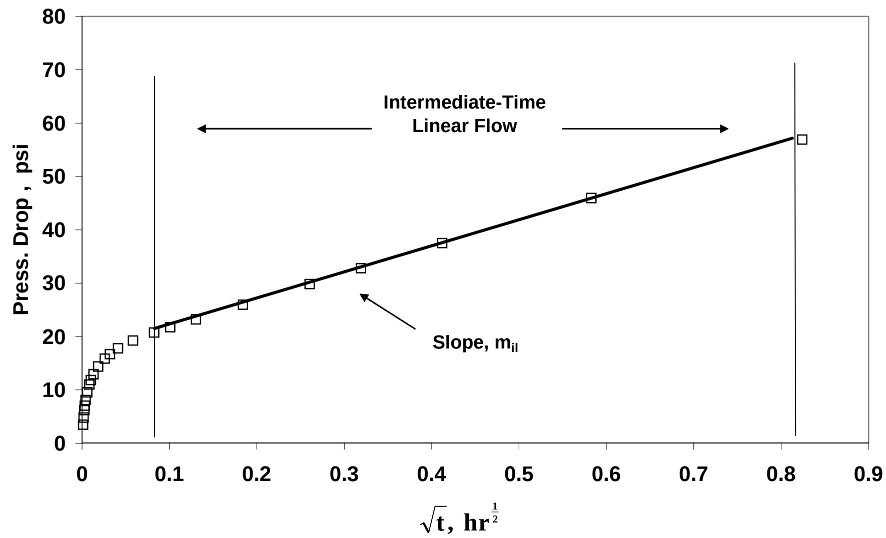

Figure 2- 8. Intermediate time linear Cartesian plot analysis.

The mechanical skin may be computed for intermediate time linear flow from straight line on the cartesian plot of Δp_{wf} vs. $\sqrt{t}$ as shown below.

$$s = \frac{\sqrt{k_y k_z} L_h}{141.2 qB\mu} \Delta p_{wf}(t=0) - s_z \tag{2-38}$$

where s_z is given by Eq. 2-36.

(iii) <u>Pseudo-radial (Late radial) flow.</u>

A two-dimensional flow period in the horizontal plane develops when the flow reaches the tips of the well as can be seen in Fig. 2-9. If pseudo-radial flow exists, the derivatives in diagnostic plot should display a constant slope as shown in Fig. 2-3.

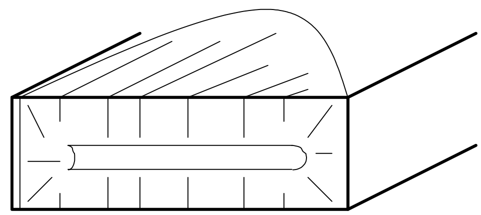

Figure 2- 9. Pseudo- late radial flow, LTRF.

The appropriate expression for this flow regime is given by:

$$\Delta p_{wf} = \frac{162.6 qB\mu}{\sqrt{k_x k_y}\,h}\left(\log t + \log \frac{k}{\phi c_t \mu L_h^2} - 1.757 + \frac{\sqrt{k_x / k}}{1.151}(\sigma + F) + \frac{\sqrt{k_x / k_y}}{1.151 k} s \right), \tag{2-39}$$

where

$$\sigma(x_D, y_D) = \frac{1}{4}\left\{ \begin{array}{l} \left(x_D - \sqrt{k/k_x}\right)\ln\left[\left(x_D - \sqrt{k/k_x}\right)^2 + y_D^2\right] \\ -\left(x_D + \sqrt{k/k_x}\right)\ln\left[\left(x_D + \sqrt{k/k_x}\right)^2 + y_D^2\right] \\ +2y_D\left(arctg\dfrac{x_D - \sqrt{k/k_x}}{y_D} - arctg\dfrac{x_D + \sqrt{k/k_x}}{y_D}\right) \end{array} \right\}, \tag{2-40}$$

where,

$$\sigma = \left\{ \begin{array}{ll} 0 & \textit{for}\ \text{uniform flux} \\ \ln 2 - 1 & \textit{for}\ \text{infinite-conductivity flux} \end{array} \right\}, \tag{2-41}$$

and,

$$F = -\frac{h}{L_h}\sqrt{\frac{k_x}{k_z}}\ln\left\{ 4\sin\left[\frac{\pi}{2h}\left(2z_w + r_{w,eq}\right)\right]\sin\left(\frac{\pi}{2h} r_{w,eq}\right)\right\} - \varphi\,. \tag{2-42}$$

for long horizontal wells.

In Equation 2-42, φ can be neglected within 1 % for most practical conditions. At late times, a semi-log plot of Δp_{wf} vs. t (Fig. 2-10) displays straight line with a slope equal to

$$m_{lr} = \frac{162.6 qB\mu}{\sqrt{k_x k_y} h}. \tag{2-43}$$

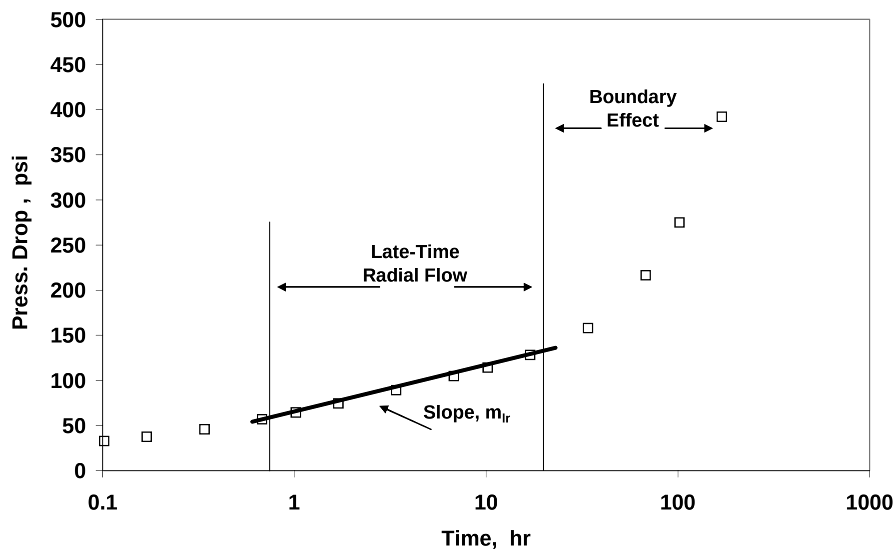

Figure 2- 10. Semi-log plot of Pseudo–Radial (late time) flow, LTRF.

From the slope, the skin may be computed from

$$s = \frac{1.151k}{\sqrt{k_x k_y}}\left(\frac{\Delta p_{wf}}{m_{lr}} - \log t - \log\frac{k}{\phi c_t \mu L_h^2} + 1.757\right) - \sqrt{\frac{k}{k_y}}(\sigma + F). \tag{2-44}$$

B. Boundary Dominated flow Regimes.

(i) Pseudosteady flow regime.

Pseudosteady flow regime exists if the well is located in a completely closed reservoir and is produced at a constant rate.

(ii) Steady flow regime.

Steady flow period prevails in the reservoir if it is under natural or artificial mechanism such as water influx or fluid injection.

Figure 2-11 shows the development of the boundary dominated flow regime. Another linear flow following the second radial flow will be seen in the diagnostic plot as shown in Fig. 2-3.

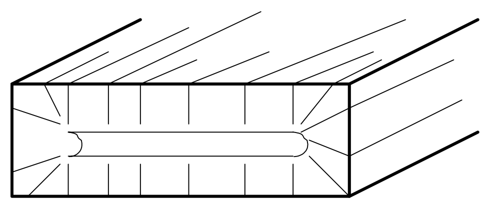

Figure 2- 11. Boundary dominated flow regime.

The expression of the pressure for wells in closed cylindrical reservoirs during pseudosteady flow is given below:

$$p_i - p_{wf} = \frac{0.234qB}{\phi c_t Ah} + \frac{141.2qB\mu}{kh}\left(\ln\frac{2r_e}{L_h} - \frac{3}{4} + 1 + \sigma + F + s\right). \qquad (2\text{-}45)$$

A Cartesian plot of Δp_{wf} vs. t as shown in Fig. 2-12 should yield straight line with slope

$$m_{ps} = \frac{0.234qB}{\phi cAh}. \qquad (2\text{-}46)$$

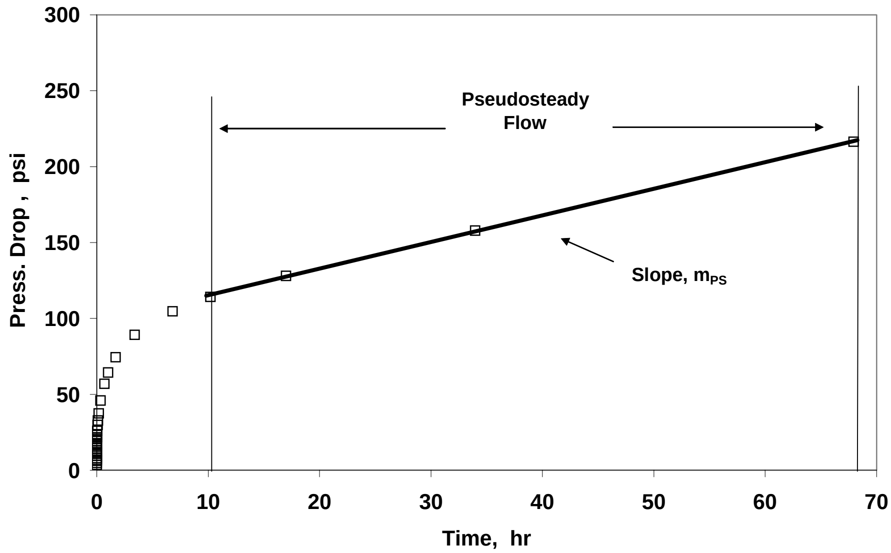

Figure 2- 12. Cartesian plot of pseudo-steady flow.

The expression of the pressure for wells in closed cylindrical reservoirs during steady state flow is given below:

$$p_i - p_{wf} = \frac{141.2 qB\mu}{kh}\left(\ln\frac{2r_e}{L_h} + 1 + \sigma + F + s\right). \tag{2-47}$$

This flow regime is not of practical interest for pressure-transient analysis purposes.

Chapter 3
NUMERICAL SIMULATION OF FLOW TOWARD HORIZONTAL WELLS

Numerical simulation refers to construction and operation of a numerical model whose performance simulates the actual behavior of a given reservoir situation. A numerical model was used in this dissertation to study horizontal wells and it consists of a set of equations that, subject to certain assumptions, describes the physical processes active in the reservoir. The nearly exponential growth in annual rate of simulation-related publications from the mid-1960's to the present indicates the industry's widespread interest in mathematical modeling as an engineering tool.

A numerical simulator consists of a set of difference equations requiring numerical solution as opposed to a set of partial differential equations amenable to analytical solution. The large amount of arithmetic performed by a numerical simulator stems from the large number of gridblocks representing the reservoir model and the number of complex flow equations.

A simulation model generally requires extensive input data. For instance, the reservoir description includes reservoir structure, grid and time step representation, and other attributes such as porosity and permeability. This is not any different in simulation of horizontal wells.

In this dissertation, Visual Fortran (Fortran 90) is used to write simulation code and run the desired models.

3.1 3-D Finite-Difference Formulation of Oil and Gas Flow

In this section we will present two finite-difference formulations for transient flow for horizontal well. The first formulation will cover single-phase flow and the second one will cover two-phase flow of oil and gas. We have neglected the solution gas in the two-phase formulation for simplicity; however, it can be included, but should not affect the outcome for the purpose intended in this study because the transient flow test compared to the production life of reservoir is very small. Therefore, average reservoir pressure during given test will change very little. Thus, during the test, the likelihood of free-gas saturation change as a result of gas coming out of or going back into the solution is minimum. Furthermore, gas-phase redisolution is a very slow process, which causes undersaturation of the oil phase, and will not significantly affect the pressure transient behavior during a well test. Conventional black oil simulators assume instantaneous gas-oil equilibrium, thus, they don not account for real life undersaturation or supersaturation. The following equations were derived based on the assumptions of single- and two-phase flow of slightly compressible fluids. The derivations are for Cartesian coordinates.

3.1.1 Numerical Solution for Single-Phase Flow

Equation 3-1 is the finite-difference equations in 3-D space:

$$\Delta_x T_x\left(\Delta_x p-\gamma\Delta_x D\right)+\Delta_y T_y\left(\Delta_y p-\gamma\Delta_y D\right)+\Delta_z T_z\left(\Delta_z p-\gamma\Delta_z D\right)+q=\frac{V_R}{\Delta t}\Delta_t\left(\phi b\right), \tag{3-1}$$

where

$$\begin{aligned}\Delta_x T_x\left(\Delta_x p-\gamma\Delta_x D\right)&=T_{x_{i+\frac{1}{2},j,k}}\left(\left(p^{n+1}_{i+1,j,k}-p^{n+1}_{i,j,k}\right)-\gamma\left(D_{i+1,j,k}-D_{i,j,k}\right)\right)\\&-T_{x_{i-\frac{1}{2},j,k}}\left(\left(p^{n+1}_{i,j,k}-p^{n+1}_{i-1,j,k}\right)-\gamma\left(D_{i,j,k}-D_{i-1,j,k}\right)\right)\end{aligned}, \tag{3-2}$$

$$\Delta_y T_y \left(\Delta_y p - \gamma \Delta_y D\right) = T_{y_{i,j+\frac{1}{2},k}} \left(\left(p^{n+1}_{i,j+1,k} - p^{n+1}_{i,j,k}\right) - \gamma\left(D_{i,j+1,k} - D_{i,j,k}\right)\right) - T_{y_{i,j-\frac{1}{2},k}} \left(\left(p^{n+1}_{i,j,k} - p^{n+1}_{i,j-1,k}\right) - \gamma\left(D_{i,j,k} - D_{i,j-1,k}\right)\right), \tag{3-3}$$

$$\Delta_z T_z \left(\Delta_z p - \gamma \Delta_z D\right) = T_{z_{i,j,k+\frac{1}{2}}} \left(\left(p^{n+1}_{i,j,k+1} - p^{n+1}_{i,j,k}\right) - \gamma\left(D_{i,j,k+1} - D_{i,j,k}\right)\right) - T_{y_{i,j,k-\frac{1}{2}}} \left(\left(p^{n+1}_{i,j,k} - p^{n+1}_{i,j,k-1}\right) - \gamma\left(D_{i,j,k} - D_{i,j,k-1}\right)\right), \tag{3-4}$$

$$\Delta_t(\phi b) = \phi^n \Delta_t b + b^{n+1}\Delta_t \phi = \left[\phi^n\left(\frac{\overline{\Delta_t b}}{\Delta_t p}\right) + b^{n+1}\left(\frac{\overline{\Delta_t \phi}}{\Delta_t p}\right)\right]_{i,j,k} \Delta_t p_{i,j,k}, \cong \phi b c_t \Delta_t p_{i,j,k} \cong \phi b c_t \left(p^{n+1}_{i,j,k} - p^{n}_{i,j,k}\right). \tag{3-5}$$

$$V_{R_{i,j,k}} = \Delta x_{i,j,k} \Delta y_{i,j,k} \Delta z_{i,j,k}, \tag{3-6}$$

and

$$q^{n+1}_{i,j,k} = -WI^n_{i,j,k}\left(p^{n+1}_{i,j,k} - p_{well}{}^{n+1}_{i,j,k}\right), \tag{3-7}$$

where

$$WI^n_{i,j,k} = 2\pi(0.006328)\left(\frac{k}{\mu B}\right)^n_{i,j,k} \frac{\Delta x_{i,j,k}}{\left[\left\{(1-(\frac{r_w}{r_0})^2)\, ln(\frac{r_0}{r_w})\right\} + s\right]}. \tag{3-8}$$

Equation 3-8 is known as the steady-state well index. For transient flow applications, we use the following “transient well index”:

$$WI^n_{i,j,k} = 4\pi(0.006328)\left(\frac{k}{\mu\ B}\right)^n_{i,j,k} \times \frac{\Delta x_{i,j,k}}{E_i\left(-\frac{\phi c_t \mu\ r_0^2}{4\times 2.637\times 10^{-4} k_z t}\right) - E_i\left(-\frac{\phi c_t \mu\ r_w^2}{4\times 2.637\times 10^{-4} k_z t}\right)}, \tag{3-9}$$

where

$$k = \sqrt{(k_y k_z)}\ , \tag{3-10}$$

and

$$r_0 = \sqrt{\left(\frac{\Delta z \Delta y}{\pi}\right)} e^{-0.5}\ . \tag{3-11}$$

3.1.2 Numerical Solution for Two-Phase Flow

Equations 3-12 and 3-26 are the finite-difference equations in 3-D space for oil and gas respectively.

Oil flow:

$$\begin{aligned}&\Delta_x T_{ox}\left(\Delta_x p_o - \gamma_o \Delta_x D\right) + \Delta_y T_{oy}\left(\Delta_y p_o - \gamma_o \Delta_y D\right) + \Delta_z T_{oz}\left(\Delta_z p_o - \gamma_o \Delta_z D\right) + q_o \\ &= \frac{V_R}{\Delta t}\Delta_t\left(\phi b_o S_o\right)\end{aligned}\ , \tag{3-12}$$

where

$$\begin{aligned}\Delta_x T_{o_x}\left(\Delta_x p_o - \gamma_o \Delta_x D\right) &= T^n_{ox_{i+\frac{1}{2},j,k}}\left(\left(p^{n+1}_{o_{i+1,j,k}} - p^{n+1}_{o_{i,j,k}}\right) - \gamma^n_{o_{i+\frac{1}{2},j,k}}\left(D_{i+1,j,k} - D_{i,j,k}\right)\right) \\ &- T^n_{ox_{i-\frac{1}{2},j,k}}\left(\left(p^{n+1}_{o_{i,j,k}} - p^{n+1}_{o_{i-1,j,k}}\right) - \gamma^n_{o_{i-\frac{1}{2},j,k}}\left(D_{i,j,k} - D_{i-1,j,k}\right)\right)\end{aligned}\ , \tag{3-13}$$

$$\begin{aligned}\Delta_y T_{o_y}\left(\Delta_y p_o - \gamma_o \Delta_y D\right) &= T^n_{oy_{i,j+\frac{1}{2},k}}\left(\left(p^{n+1}_{o_{i,j+1,k}} - p^{n+1}_{o_{i,j,k}}\right) - \gamma^n_{o_{i,j+\frac{1}{2},k}}\left(D_{i,j+1,k} - D_{i,j,k}\right)\right) \\ &- T^n_{oy_{i,j-\frac{1}{2},k}}\left(\left(p^{n+1}_{o_{i,j,k}} - p^{n+1}_{o_{i,j-1,k}}\right) - \gamma^n_{o_{i,j-\frac{1}{2},k}}\left(D_{i,j,k} - D_{i,j-1,k}\right)\right)\end{aligned}\ , \tag{3-14}$$

$$\Delta_z T_{o_z}\left(\Delta_z p_o - \gamma_o \Delta_z D\right) = T^n_{oz_{i,j,k+\frac{1}{2}}}\left(\left(p^{n+1}_{o_{i,j,k+1}} - p^{n+1}_{o_{i,j,k}}\right) - \gamma^n_{o_{i,j,k+\frac{1}{2}}}\left(D_{i,j,k+1} - D_{i,j,k}\right)\right)$$
$$- T^n_{oz_{i,j,k-\frac{1}{2}}}\left(\left(p^{n+1}_{o_{i,j,k}} - p^{n+1}_{o_{i,j,k-1}}\right) - \gamma^n_{o_{i,j,k-\frac{1}{2}}}\left(D_{i,j,k} - D_{i,j,k-1}\right)\right),$$

(3-15)

and

$$\frac{V_R}{\Delta t}\Delta_t\left(\phi b_o S_o\right) = C_{11}\Delta_t S_o + C_{12}\Delta_t p\,, \tag{3-16}$$

where

$$C_{11} = 24\frac{V_{R_{i,j,k}}}{\Delta t}\left\{b^{n+1}_{o_{i,j,k}}\phi^{n+1}_{i,j,k}\right\}, \tag{3-17}$$

$$C_{12} = 24\frac{V_{R_{i,j,k}}}{\Delta t}\left\{\left(\phi S_o\right)^n_{i,j,k}\left(c_o b_o\right)^{n+\frac{1}{2}}_{i,j,k} + b_o^{n+1} S_o^n\left(\phi c_\phi\right)^{n+\frac{1}{2}}_{i,j,k}\right\}, \tag{3-18}$$

and

$$V_{R_{i,j,k}} = \Delta x_{i,j,k} + \Delta y_{i,j,k} + \Delta z_{i,j,k}\,. \tag{3-19}$$

The oil rate is expressed in the following relation.

$$q^n_{o_{i,j,k}} = -WI^n_{o_{i,j,k}}\left(p^{n+1}_{o_{i,j,k}} - p^{n+1}_{well_{i,j,k}}\right), \tag{3-20}$$

where

$$WI^n_{o_{i,j,k}} = 2\pi(0.006328)\left(\frac{kk_{ro}}{\mu_o B_o}\right)^n_{i,j,k}\frac{\Delta x_{i,j,k}}{\left[(1-(\frac{r_w}{r_0})^2)\,ln(\frac{r_0}{r_w}) + s\right]}. \tag{3-21}$$

Equation 3-21 is known as the steady-state well index. The following equation “transient well index” is for transient flow applications.

$$WI_{o_{i,j,k}}^{n} = 4\pi(0.006328)(\frac{kk_{ro}}{\mu_o B_o})_{i,j,k}^{n} \times \frac{\Delta x_{i,j,k}}{E_i\left(-\frac{\phi c_t r_0^2}{4\times 2.637\times 10^{-4}\lambda k_z t}\right) - E_i\left(-\frac{\phi c_t r_w^2}{4\times 2.637\times 10^{-4}\lambda k_z t}\right)}, \tag{3-22}$$

where

$$k = \sqrt{(k_y k_z)}, \tag{3-23}$$

$$\lambda = \frac{k_{ro}}{\mu_o} + \frac{k_{rg}}{\mu_g}, \tag{3-24}$$

and

$$r_0 = \sqrt{\left(\frac{\Delta z \Delta y}{\pi}\right)} e^{-0.5}. \tag{3-25}$$

<u>Gas Flow:</u>

$$\Delta_x T_{g_x}\left(\Delta_x p_g - \gamma_g \Delta_x D\right) + \Delta_y T_{g_y}\left(\Delta_y p_g - \gamma_g \Delta_y D\right) + \Delta_z T_{g_z}\left(\Delta_z p_g - \gamma_g \Delta_z D\right) + q_g = \frac{V_R}{\Delta t}\Delta_t\left(\phi b_g S_g\right), \tag{3-26}$$

where

$$\Delta_x T_{g_x}\left(\Delta_x p_g - \gamma_g \Delta_x D\right) = T_{gx_{i+\frac{1}{2},j,k}}^{n}\left(\left(p_{g_{i+1,j,k}}^{n+1} - p_{g_{i,j,k}}^{n+1}\right) - \gamma_{g_{i+\frac{1}{2},j,k}}^{n}\left(D_{i+1,j,k} - D_{i,j,k}\right)\right) - T_{gx_{i-\frac{1}{2},j,k}}^{n}\left(\left(p_{g_{i,j,k}}^{n+1} - p_{g_{i-1,j,k}}^{n+1}\right) - \gamma_{g_{i-\frac{1}{2},j,k}}^{n}\left(D_{i,j,k} - D_{i-1,j,k}\right)\right), \tag{3-27}$$

$$\Delta_y T_{g_y}\left(\Delta_y p_g - \gamma_g \Delta_y D\right) = T_{gy_{i,j+\frac{1}{2},k}}^{n}\left(\left(p_{g_{i,j+1,k}}^{n+1} - p_{g_{i,j,k}}^{n+1}\right) - \gamma_{g_{i,j+\frac{1}{2},k}}^{n}\left(D_{i,j+1,k} - D_{i,j,k}\right)\right) - T_{gy_{i,j-\frac{1}{2},k}}^{n}\left(\left(p_{g_{i,j,k}}^{n+1} - p_{g_{i,j-1,k}}^{n+1}\right) - \gamma_{g_{i,j-\frac{1}{2},k}}^{n}\left(D_{i,j,k} - D_{i,j-1,k}\right)\right), \tag{3-28}$$

$$\Delta_z T_{g_z}\left(\Delta_z p_g - \gamma_g \Delta_z D\right) = T^n_{gz_{i,j,k+\frac{1}{2}}}\left(\left(p^{n+1}_{g_{i,j,k+1}} - p^{n+1}_{g_{i,j,k}}\right) - \gamma^n_{g_{i,j,k+\frac{1}{2}}}\left(D_{i,j,k+1} - D_{i,j,k}\right)\right) - T^n_{gz_{i,j,k-\frac{1}{2}}}\left(\left(p^{n+1}_{g_{i,j,k}} - p^{n+1}_{g_{i,j,k-1}}\right) - \gamma^n_{g_{i,j,k-\frac{1}{2}}}\left(D_{i,j,k} - D_{i,j,k-1}\right)\right), \tag{3-29}$$

$$\frac{V_R}{\Delta t}\Delta_t\left(\phi b_g S_g\right) = C_{21}\Delta_t S_o + C_{22}\Delta_t p \ , \tag{3-30}$$

$$C_{21} = -24\frac{V_{R_{i,j,k}}}{\Delta t}\left\{b^{n+1}_{g_{i,j,k}}\phi^{n+1}_{i,j,k}\right\}, \tag{3-31}$$

$$C_{22} = 24\frac{V_{R_{i,j,k}}}{\Delta t}\left\{\left(\phi S_g\right)^n_{i,j,k}\left(c_g b_g\right)^{n+\frac{1}{2}}_{i,j,k} + b^{n+1}_g S^n_g\left(\phi c_\phi\right)^{n+\frac{1}{2}}_{i,j,k}\right\}, \tag{3-32}$$

and

$$V_{R_{i,j,k}} = \Delta x_{i,j,k} + \Delta y_{i,j,k} + \Delta z_{i,j,k} \ . \tag{3-33}$$

The gas rate equation is given by:

$$q^n_{g_{i,j,k}} = -WI^n_{g_{i,j,k}}\left(p^n_{g_{i,j,k}} - p^n_{well_{i,j,k}}\right), \tag{3-34}$$

where

$$WI^n_{g_{i,j,k}} = 2\pi(0.006328)\left(\frac{kk_{rg}}{\mu_g B_g}\right)^n_{i,j,k}\frac{\Delta x_{i,j,k}}{\left[(1-(\frac{r_w}{r_o})^2)\ln(\frac{r_0}{r_w})+s\right]} \ . \tag{3-35}$$

Equation 3-30 is known as the steady-state well index. The transient well index equation for transient flow applications is given by:

$$WI^n_{g_{i,j,k}} = 4\pi(0.006328)\left(\frac{kk_{rg}}{\mu_g B_g}\right)^n_{i,j,k} \times \frac{\Delta x_{i,j,k}}{E_i\left(-\frac{\phi c_t r_0^2}{4\times 2.637\times 10^{-4}\lambda k_z t}\right) - E_i\left(-\frac{\phi c_t r_w^2}{4\times 2.637\times 10^{-4}\lambda k_z t}\right)}, \tag{3-36}$$

where

$$k = \sqrt{(k_y k_z)}\,, \tag{3-37}$$

$$\lambda = \frac{k_{ro}}{\mu_o} + \frac{k_{rg}}{\mu_g}\,, \tag{3-38}$$

and

$$r_0 = \sqrt{\left(\frac{\Delta z \Delta y}{\pi}\right)} e^{-0.5}. \tag{3-39}$$

3.2 Grid Coefficients (Transmissivities)

The transmissivities for each grid were generated from the finite-difference equation, Eq.3-1. Each grid in 3-D has seven transmissivities. Equation 3-1 can be written in the following form for single-phase flow:

$$\begin{aligned} &A_{i,j,k} p^{n+1}_{i,j,k-1} + B_{i,j,k} p^{n+1}_{i,j-1,k} + D_{i,j,k} p^{n+1}_{i-1,j,k} + E_{i,j,k} p^{n+1}_{i,j,k} \\ &+ F_{i,j,k} p^{n+1}_{i+1,j,k} + H_{i,j,k} p^{n+1}_{i,j+1,k} + L_{i,j,k} p^{n+1}_{i,j,k+1} + WI_{i,j,k} p_{well_{i,j,k}} = R_{i,j,k} \end{aligned}\,, \tag{3-40}$$

and for two-phase flow:

$$\begin{aligned} &A_{i,j,k} p^{n+1}_{i,j,k-1} + B_{i,j,k} p^{n+1}_{i,j-1,k} + D_{i,j,k} p^{n+1}_{i-1,j,k} + E_{i,j,k} p^{n+1}_{i,j,k} \\ &+ F_{i,j,k} p^{n+1}_{i+1,j,k} + H_{i,j,k} p^{n+1}_{i,j+1,k} + L_{i,j,k} p^{n+1}_{i,j,k+1} + \alpha^{n+1}_{i,j,k} WI_{o_{i,j,k}} p_{well_{i,j,k}} = R_{i,j,k} \end{aligned}\,. \tag{3-41}$$

3.2.1 Pressure Coefficients Equation in 3-D for Single-Phase Flow

The Coefficients for Eq. 3-40 are shown below.

$$F_{i,j,k} = T^n_{x_{i+\frac{1}{2},j,k}} = 0.006328\left(\frac{k_x}{\mu B}\right)^n_{i+\frac{1}{2},j,k} \frac{\Delta y_{i,j,k} \Delta z_{i,j,k}}{\Delta x_{i+\frac{1}{2},j,k}}\,, \tag{3-42}$$

$$D_{i,j,k} = T^n_{x_{i-\frac{1}{2},j,k}} = 0.006328\left(\frac{k_x}{\mu B}\right)^n_{i-\frac{1}{2},j,k} \frac{\Delta y_{i,j,k} \Delta z_{i,j,k}}{\Delta x_{i-\frac{1}{2},j,k}}\,, \tag{3-43}$$

$$H_{i,j,k} = T^n_{y_{i,j+\frac{1}{2},k}} = 0.006328(\frac{k_y}{\mu B})^n_{i,j+\frac{1}{2},k} \frac{\Delta x_{i,j,k} \Delta z_{i,j,k}}{\Delta y_{i,j+\frac{1}{2},k}} , \tag{3-44}$$

$$B_{i,j,k} = T^n_{y_{i,j-\frac{1}{2},k}} = 0.006328(\frac{k_y}{\mu B})^n_{i,j-\frac{1}{2},k} \frac{\Delta x_{i,j,k} \Delta z_{i,j,k}}{\Delta y_{i,j-\frac{1}{2},k}} , \tag{3-45}$$

$$L_{i,j,k} = T^n_{z_{i,j,k+\frac{1}{2}}} = 0.006328(\frac{k_z}{\mu B})^n_{i,j,k+\frac{1}{2}} \frac{\Delta x_{i,j,k} \Delta y_{i,j,k}}{\Delta z_{i,j,k+\frac{1}{2}}} , \tag{3-46}$$

$$A_{i,j,k} = T^n_{z_{i,j,k-\frac{1}{2}}} = 0.006328(\frac{k_z}{\mu B})^n_{i,j,k-\frac{1}{2}} \frac{\Delta x_{i,j,k} \Delta y_{i,j,k}}{\Delta z_{i,j,k-\frac{1}{2}}} , \tag{3-47}$$

$$E_{i,j,k} = -\left\{ \begin{array}{l} A_{i,j,k} + B_{i,j,k} + D_{i,j,k} + F_{i,j,k} + H_{i,j,k} + L_{i,j,k} + WI^n_{i,j,k} \\ + 24 \frac{V_{R\,i,j,k}}{\Delta t} \left[\phi^n \left(\frac{\overline{\Delta_t b}}{\Delta_t p} \right) + b^{n+1} \left(\frac{\overline{\Delta_t \phi}}{\Delta_t p} \right) \right]_{i,j,k} \end{array} \right\} , \tag{3-48}$$

and

$$\begin{aligned} R_{i,j,k} = & -\left\{ 24 \frac{V_{R_{i,j,k}}}{\Delta t} \left[\phi^n \left(\frac{\overline{\Delta_t b}}{\Delta_t p} \right) + b^{n+1} \left(\frac{\overline{\Delta_t \phi}}{\Delta_t p} \right) \right]_{i,j,k} \right\} p^n_{i,j,k} \\ & + T^n_{x_{i+\frac{1}{2},j,k}} \gamma^n_{i+\frac{1}{2},j,k} \left(D_{i+1,j,k} - D_{i,j,k} \right) - T^n_{x_{i-\frac{1}{2},j,k}} \gamma^n_{i-\frac{1}{2},j,k} \left(D_{i,j,k} - D_{i-1,j,k} \right) \\ & + T^n_{y_{i,j+\frac{1}{2},k}} \gamma^n_{i,j+\frac{1}{2},k} \left(D_{i,j+1,k} - D_{i,j,k} \right) - T^n_{y_{i,j-\frac{1}{2},k}} \gamma^n_{i,j-\frac{1}{2},k} \left(D_{i,j,k} - D_{i,j-1,k} \right) \\ & + T^n_{z_{i,j,k+\frac{1}{2}}} \gamma^n_{i,j,k+\frac{1}{2}} \left(D_{i,j,k} - D_{i,j,k+1} \right) - T^n_{z_{i,j,k-\frac{1}{2}}} \gamma^n_{i,j,k-\frac{1}{2}} \left(D_{i,j,k} - D_{i,j,k-1} \right) \\ & + WI^n_{i,j,k} \ \gamma^n_{i+\frac{1}{2},j,k} \left[\left(D_{i,j,k} - D_{i+1,j,k} \right) - HF_{i+\frac{1}{2},j,k} \right]. \end{aligned} \tag{3-49}$$

3.2.2 Pressure Coefficients Equation in 3-D for Two-Phase Flow

Equations 3-12 and 3-26 were combined to eliminate the saturations in the classic IMPES (implicit pressure explicit saturation) formulation. The outcome is presented below in the form of Eq. 3-41.

$$F_{i,j,k} = \alpha_{i,j,k}^{n+1} T_{ox_{i+\frac{1}{2},j,k}}^{n} + T_{gx_{i+\frac{1}{2},j,k}}^{n} , \tag{3-50}$$

$$D_{i,j,k} = \alpha_{i,j,k}^{n+1} T_{ox_{i-\frac{1}{2},j,k}}^{n} + T_{gx_{i-\frac{1}{2},j,k}}^{n} , \tag{3-51}$$

$$H_{i,j,k} = \alpha_{i,j,k}^{n+1} T_{oy_{i,j+\frac{1}{2},k}}^{n} + T_{g_{i,j+\frac{1}{2},k}}^{n} , \tag{3-52}$$

$$B_{i,j,k} = \alpha_{i,j,k}^{n+1} T_{oy_{i,j-\frac{1}{2},k}}^{n} + T_{gy_{i,j-\frac{1}{2},k}}^{n} , \tag{3-53}$$

$$L_{i,j,k} = \alpha_{i,j,k}^{n+1} T_{oz_{i,j,k+\frac{1}{2}}}^{n} + T_{gz_{i,j,k+\frac{1}{2}}}^{n} , \tag{3-54}$$

$$A_{i,j,k} = \alpha_{i,j,k}^{n+1} T_{oz_{i,j,k-\frac{1}{2}}}^{n} + T_{gz_{i,j,k-\frac{1}{2}}}^{n} , \tag{3-55}$$

$$E_{i,j,k} = -\left\{ \begin{array}{l} A_{i,j,k} + B_{i,j,k} + D_{i,j,k} + F_{i,j,k} + H_{i,j,k} + L_{i,j,k} \\ + \alpha_{i,j,k}^{n+1} C_{12} + C_{22} + \alpha_{i,j,k}^{n+1} WI_{o_{i,j,k}}^{n} \end{array} \right\} , \tag{3-56}$$

$$
\begin{aligned}
R^{n-}_{i,j,k} = {} & \alpha^{n+1}_{i,j,k}\left\{T^n_{ox_{i+\frac{1}{2},j,k}}\gamma^n_{o_{i+\frac{1}{2},j,k}}\left(D_{i+1,j,k}-D_{i,j,k}\right)-T^n_{ox_{i-\frac{1}{2},j,k}}\gamma^n_{o_{i-\frac{1}{2},j,k}}\left(D_{i,j,k}-D_{i-1,j,k}\right)\right\} \\
& +\alpha^{n+1}_{i,j,k}\left\{T^n_{oy_{i,j+\frac{1}{2},k}}\gamma^n_{o_{i,j+\frac{1}{2},k}}\left(D_{i,j+1,k}-D_{i,j,k}\right)-T^n_{oy_{i,j-\frac{1}{2},k}}\gamma^n_{o_{i,j-\frac{1}{2},k}}\left(D_{i,j,k}-D_{i,j-1,k}\right)\right\} \\
& +\alpha^{n+1}_{i,j,k}\left\{T^n_{oz_{i,j,k+\frac{1}{2}}}\gamma^n_{o_{i,j,k+\frac{1}{2}}}\left(D_{i,j,k+1}-D_{i,j,k}\right)-T^n_{oz_{i,j,k-\frac{1}{2}}}\gamma^n_{o_{i,j,k-\frac{1}{2}}}\left(D_{i,j,k}-D_{i,j,k-1}\right)\right\} \\
& +\alpha^{n+1}_{i,j,k}\left\{T^n_{ox_{i+\frac{1}{2},j,k}}\gamma^n_{o_{i+\frac{1}{2},j,k}}\left(P^n_{cog_{i+1,j,k}}-P^n_{cog_{i,j,k}}\right)-T^n_{ox_{i-\frac{1}{2},j,k}}\gamma^n_{o_{i-\frac{1}{2},j,k}}\left(P^n_{cog_{i,j,k}}-P^n_{cog_{i-1,j,k}}\right)\right\} \\
& +\alpha^{n+1}_{i,j,k}\left\{T^n_{oy_{i,j+\frac{1}{2},k}}\gamma^n_{o_{i,j+\frac{1}{2},k}}\left(P^n_{cog_{i,j+1,k}}-P^n_{cog_{i,j,k}}\right)-T^n_{oy_{i,j-\frac{1}{2},k}}\gamma^n_{o_{i,j-\frac{1}{2},k}}\left(P^n_{cog_{i,j,k}}-P^n_{cog_{i,j-1,k}}\right)\right\} \\
& +\alpha^{n+1}_{i,j,k}\left\{T^n_{oz_{i,j,k+\frac{1}{2}}}\gamma^n_{o_{i,j,k+\frac{1}{2}}}\left(P^n_{cog_{i,j,k+1}}-P^n_{cog_{i,j,k}}\right)-T^n_{oz_{i,j,k-\frac{1}{2}}}\gamma^n_{o_{i,j,k-\frac{1}{2}}}\left(P^n_{cog_{i,j,k}}-P^n_{cog_{i,j,k-1}}\right)\right\} \\
& + \left\{T^n_{gx_{i+\frac{1}{2},j,k}}\gamma^n_{g_{i+\frac{1}{2},j,k}}\left(D_{i+1,j,k}-D_{i,j,k}\right)-T^n_{gx_{i-\frac{1}{2},j,k}}\gamma^n_{g_{i-\frac{1}{2},j,k}}\left(D_{i,j,k}-D_{i-1,j,k}\right)\right\} \\
& + \left\{T^n_{gy_{i,j+\frac{1}{2},k}}\gamma^n_{g_{i,j+\frac{1}{2},k}}\left(D_{i,j+1,k}-D_{i,j,k}\right)-T^n_{gy_{i,j-\frac{1}{2},k}}\gamma^n_{g_{i,j-\frac{1}{2},k}}\left(D_{i,j,k}-D_{i,j-1,k}\right)\right\} \\
& + \left\{T^n_{gz_{i,j,k+\frac{1}{2}}}\gamma^n_{g_{i,j,k+\frac{1}{2}}}\left(D_{i,j,k+1}-D_{i,j,k}\right)-T^n_{gz_{i,j,k-\frac{1}{2}}}\gamma^n_{g_{i,j,k-\frac{1}{2}}}\left(D_{i,j,k}-D_{i,j,k-1}\right)\right\} \\
& + \alpha^{n+1}_{i,j,k}\left\{WI^n_{o_{i,j,k}}\gamma^n_{o_{i+\frac{1}{2},j,k}}\left[\left(D_{i,j,k}-D_{i+1,j,k}\right)-HF_{i+\frac{1}{2},j,k}\right]\right\} \\
& - \left(\alpha^{n+1}_{i,j,k}WI^n_{o_{i,j,k}}\right)p^n_{cog_{i,j,k}} \\
& - \left(\alpha^{n+1}_{i,j,k}C_{12}+C_{22}\right)p^n_{g_{i,j,k}} \\
& - q^n_{g_{i,j,k}}\ .
\end{aligned}
\tag{3-57}
$$

Where

$$T^n_{ox_{i\pm\frac{1}{2},j,k}} = 0.006328\left(\frac{k_x k_{ro}}{\mu_o B_o}\right)^n_{i\pm\frac{1}{2},j,k}\ \frac{\Delta y_{i,j,k}\Delta z_{i,j,k}}{\Delta x_{i\pm\frac{1}{2},j,k}}\,, \tag{3-58}$$

$$T^n_{oy_{i,j\pm\frac{1}{2},k}} = 0.006328\left(\frac{k_y k_{ro}}{\mu_o B_o}\right)^n_{i,j\pm\frac{1}{2},k}\ \frac{\Delta x_{i,j,k}\Delta z_{i,j,k}}{\Delta y_{i,j\pm\frac{1}{2},k}}\,, \tag{3-59}$$

$$T^n_{oz_{i,j,k\pm\frac{1}{2}}} = 0.006328\left(\frac{k_z k_{ro}}{\mu_o B_o}\right)^n_{i,j,k\pm\frac{1}{2}} \frac{\Delta x_{i,j,k}\Delta y_{i,j,k}}{\Delta z_{i,j,k\pm\frac{1}{2}}}, \tag{3-60}$$

$$T^n_{gx_{i\pm\frac{1}{2},j,k}} = 0.006328\left(\frac{k_x k_{rg}}{\mu_g B_g}\right)^n_{i\pm\frac{1}{2},j,k} \frac{\Delta y_{i,j,k}\Delta z_{i,j,k}}{\Delta x_{i\pm\frac{1}{2},j,k}}, \tag{3-61}$$

$$T^n_{gy_{i,j\pm\frac{1}{2},k}} = 0.006328\left(\frac{k_y k_{rg}}{\mu_g B_g}\right)^n_{i,j\pm\frac{1}{2},k} \frac{\Delta x_{i,j,k}\Delta z_{i,j,k}}{\Delta y_{i,j\pm\frac{1}{2},k}}, \tag{3-62}$$

$$T^n_{gz_{i,j,k\pm\frac{1}{2}}} = 0.006328\left(\frac{k_z k_{rg}}{\mu_g B_g}\right)^n_{i,j,k\pm\frac{1}{2}} \frac{\Delta x_{i,j,k}\Delta y_{i,j,k}}{\Delta z_{i,j,k\pm\frac{1}{2}}}, \tag{3-63}$$

$$\alpha^{n+1}_{i,j,k} = -\frac{C_{21}}{C_{11}} = \frac{b^{n+1}_{g_{i,j,k}}}{b^{n+1}_{o_{i,j,k}}}, \tag{3-64}$$

and

$$p^{n+1}_{o_{i,j,k}} = p^{n+1}_{g_{i,j,k}} - p^n_{cog_{i,j,k}}. \tag{3-65}$$

3.2.3 Saturation Equations for Two-Phase Flow

The oil and gas saturations are calculated explicitly as follows:

$$
S_{g_{i,j,k}}^{n+1} = \frac{\Delta t / 24}{V_{R_{i,j,k}} b_{g_{i,j,k}}^{n+1} \phi_{i,j,k}^{n+1}}
\left[
\begin{array}{l}
T_{gx_{i+\frac{1}{2},j,k}}^{n} \left(\left(p_{g_{i+1,j,k}}^{n+1} - p_{g_{i,j,k}}^{n+1} \right) - \gamma_{g_{i+\frac{1}{2},j,k}}^{n} \left(D_{i+1,j,k} - D_{i,j,k} \right) \right) \\
- T_{gx_{i-\frac{1}{2},j,k}}^{n} \left(\left(p_{g_{i,j,k}}^{n+1} - p_{g_{i-1,j,k}}^{n+1} \right) - \gamma_{g_{i-\frac{1}{2},j,k}}^{n} \left(D_{i,j,k} - D_{i-1,j,k} \right) \right) \\
+ T_{gy_{i,j+\frac{1}{2},k}}^{n} \left(\left(p_{g_{i,j+1,k}}^{n+1} - p_{g_{i,j,k}}^{n+1} \right) - \gamma_{g_{i,j+\frac{1}{2},k}}^{n} \left(D_{i,j+1,k} - D_{i,j,k} \right) \right) \\
- T_{gy_{i,j-\frac{1}{2},k}}^{n} \left(\left(p_{g_{i,j,k}}^{n+1} - p_{g_{i,j-1,k}}^{n+1} \right) - \gamma_{g_{i,j-\frac{1}{2},k}}^{n} \left(D_{i,j,k} - D_{i,j-1,k} \right) \right) \\
+ T_{gz_{i,j,k+\frac{1}{2}}}^{n} \left(\left(p_{g_{i,j,k+1}}^{n+1} - p_{g_{i,j,k}}^{n+1} \right) - \gamma_{g_{i,j,k+\frac{1}{2}}}^{n} \left(D_{i,j,k+1} - D_{i,j,k} \right) \right) \\
- T_{gz_{i,j,k-\frac{1}{2}}}^{n} \left(\left(p_{g_{i,j,k}}^{n+1} - p_{g_{i,j,k-1}}^{n+1} \right) - \gamma_{g_{i,j,k-\frac{1}{2}}}^{n} \left(D_{i,j,k} - D_{i,j,k-1} \right) \right) \\
+ q_{g_{i,j,k}}^{n} \\
+ 24 \frac{V_{R_{i,j,k}}}{\Delta t} \left\{ b_{g_{i,j,k}}^{n} S_{g_{i,j,k}}^{n} \phi_{i,j,k}^{n} \right\}
\end{array}
\right],
\tag{3-66}
$$

and

$$
S_o^{n+1} = 1 - S_g^{n+1}. \tag{3-67}
$$

3.2.4 Wellbore Pressure Equations

Describing horizontal wells is somewhat different from vertical wells because of the geometry and the distance between perforations.

Single-Phase Flow:

The equations, including friction factor, are given below.

$$
\begin{array}{l}
- WI_{i,j,k} (p_{i,j,k}^{n+1} - p_{well_{i,j,k}}^{n+1}) - WI_{i+1,j,k} (p_{i+1,j,k}^{n+1} - p_{well_{i+1,j,k}}^{n+1}) - \cdots\cdots \\
+ 24 \frac{C_w}{\Delta t} (p_{well_{i,j,k}}^{n+1} - p_{well_{i,j,k}}^{n}) = q_t
\end{array}
, \tag{3-68}
$$

where

$$p_{well_{i,j,k}}^{n+1} - p_{well_{i+1,j,k}}^{n+1} = \gamma_{i+\frac{1}{2},j,k}^{n}\left[\left(D_{i,j,k} - D_{i+1,j,k}\right) - HF_{i+\frac{1}{2},j,k}^{n}\right], \tag{3-69}$$

and the wellbore storage effect is given by following term.

$$24\frac{5.615C_w}{\Delta t}(p_{well_{i,j,k}}^{n+1} - p_{well_{i,j,k}}^{n}) \, . \tag{3-70}$$

The Friction head loss equation is shown below.

$$HF_{i+\frac{1}{2},j,k}^{n} = f_{i+\frac{1}{2},j,k}^{n}\frac{\Delta x_{i+\frac{1}{2},j,k}\; v_{wellt_{i+\frac{1}{2},j,k}}^{2}}{2\, d_{pipe}\, g}, \tag{3-71}$$

where

$$v_{wellt_{i+\frac{1}{2},j,k}}^{2} = \left(\frac{q_{wellt_{i+1,j,k}}^{n} B_{i+1,j,k}^{n}}{\frac{\pi}{4}d^{2}}\right) / 86400 \, , \tag{3-72}$$

$$f_{i+\frac{1}{2},j,k}^{n} = \frac{64}{N_{\mathrm{Re}\,i+\frac{1}{2},j,k}^{\;n}}, \tag{3-73}$$

$$N_{Re\,i+\frac{1}{2},j,k}^{\;n} = \frac{0.06157\,\rho_{i+\frac{1}{2},j,k}^{n}}{5.615\, r_w}\left(\left|\frac{q_t^{n} B^{n}}{\mu}\right|_{i+1,j,k}\right), \tag{3-74}$$

and

$$\rho_{i+\frac{1}{2},j,k}^{n} = 144\,\gamma_{\mathrm{i+1},j,k}^{\mathrm{n}} \; . \tag{3-75}$$

<u>Two-Phase Flow:</u>

The wellbore pressure equations for oil flow are shown below.

$$\begin{aligned} &-WI_{o_{i,j,k}}^{n}(p_{o_{i,j,k}}^{n+1} - p_{well_{i,j,k}}^{n+1}) - WI_{o_{i+1,j,k}}^{n}(p_{o_{i+1,j,k}}^{n+1} - p_{well_{i+1,j,k}}^{n+1}) - \cdots\cdots \\ &+ 24\frac{5.615C_w}{\Delta t}(p_{well_{i,j,k}}^{n+1} - p_{well_{i,j,k}}^{n}) = q_{ot}^{n+1} \end{aligned}, \tag{3-76}$$

and for gas flow are given by:

$$-WI^{n}_{g_{i,j,k}}(p^{n+1}_{g_{i,j,k}} - p^{n+1}_{well_{i,j,k}}) - WI^{n}_{g_{i+1,j,k}}(p^{n+1}_{g_{i+1,j,k}} - p^{n+1}_{well_{i+1,j,k}}) - \cdots\cdots \\ + 24\frac{5.615C_w}{\Delta t}(p^{n+1}_{well_{i,j,k}} - p^{n}_{well_{i,j,k}}) = q^{n+1}_{gt} \quad , \tag{3-77}$$

where

$$p^{n+1}_{well_{i,j,k}} - p^{n+1}_{well_{i+1,j,k}} = \gamma^{n}_{i+\frac{1}{2},j,k}\left[\left(D_{i,j,k} - D_{i+1,j,k}\right) - HF_{i+\frac{1}{2},j,k}\right], \tag{3-78}$$

and the wellbore storage effect is expressed by

$$24\frac{5.615C_w}{\Delta t}(p^{n+1}_{well_{i,j,k}} - p^{n}_{well_{i,j,k}}) . \tag{3-79}$$

The Friction head loss equation is given below:

$$HF^{n}_{i+\frac{1}{2},j,k} = f^{n}_{i+\frac{1}{2},j,k}\,\frac{\Delta x_{i+\frac{1}{2},j,k}\; v^{2}_{wellt_{i+\frac{1}{2},j,k}}}{2\,d_{pipe}\;g}, \tag{3-80}$$

where

$$v^{2}_{wellt_{i+\frac{1}{2},j,k}} = v^{2}_{ot_{i+\frac{1}{2},j,k}} + v^{2}_{gt_{i+\frac{1}{2},j,k}} , \tag{3-81}$$

$$v_{ot_{i+\frac{1}{2},j,k}} = \left(\frac{q^{n}_{ot_{i+1,j,k}} B^{n}_{o_{i+1,j,k}}}{\frac{\pi}{4}d^{2}}\right) / 86400 , \tag{3-82}$$

$$v_{gt_{i+\frac{1}{2},j,k}} = \left(\frac{q^{n}_{gt_{i+1,j,k}} B^{n}_{g_{i+1,j,k}}}{\frac{\pi}{4}d^{2}}\right) / 86400 , \tag{3-83}$$

$$q^{n+1}_{t} = q^{n+1}_{gt} + q^{n+1}_{ot} , \tag{3-84}$$

and

$$f^{n}_{i+\frac{1}{2},j,k} = \frac{64}{N^{\;n}_{\mathrm{Re}\,i+\frac{1}{2},j,k}} \quad \text{for } N_{Re} \le 2000, \tag{3-85}$$

$$\frac{1}{\sqrt{f^n_{i+\frac{1}{2},j,k}}} = 1.74 - 2\log\left(\frac{2\varepsilon}{d} + \frac{18.7}{N_{\mathrm{Re}}{}^n_{i+\frac{1}{2},j,k}\sqrt{f^n_{i+\frac{1}{2},j,k}}}\right) \quad \text{for } N_{Re} > 2000,$$

(3-86)

where

$$N_{Re}{}^n_{i+\frac{1}{2},j,k} = \frac{0.06157\,\rho^n_{i+\frac{1}{2},j,k}}{5.615\,r_w}\left(\left|\frac{q^n_{ot}B^n_o}{\mu_o}\right|_{i+1,j,k} + \left|\frac{q^n_{gt}B^n_g}{\mu_g}\right|_{i+1,j,k}\right), \tag{3-87}$$

$$\rho^n_{i+\frac{1}{2},j,k} = 144\,\gamma^{\mathrm{n}}_{\mathrm{i+1},j,k}\,, \tag{3-88}$$

and

$$\gamma^n_{i+1,j,k} = \frac{\left(q^n_{ot}B^n_o\right)_{i+1,j,k}\gamma^n_{o_{i+1,j,k}} + \left(q^n_{gt}B^n_g\right)_{i+1,j,k}\gamma^n_{g_{i+1,j,k}}}{\left(q^n_{ot}B^n_o\right)_{i+1,j,k} + \left(q^n_{gt}B^n_g\right)_{i+1,j,k}}\,. \tag{3-89}$$

3.3 Non-Darcy flow Coefficients

Large flow rates cause non-Darcy flow, which means pressure gradients are no longer proportional to velocity. The model used in this study includes the non-Darcy flow effect. To account for the non-Darcy flow effects, the permeabilities in the grid system are divided by the non-Darcy term ($1+\alpha$).

3.3.1 Non-Darcy Coefficients for Single-Phase Flow

The darcy velocities are calculated as follows:

$$v^n_{x_{i\pm\frac{1}{2},j,k}} = 0.006328\left(\frac{k_x}{\mu}\right)^n_{i\pm\frac{1}{2},j,k}\frac{\left(\Delta p^n_{i\pm\frac{1}{2},j,k} - \gamma^n_{i\pm\frac{1}{2},j,k}\Delta D_{i\pm\frac{1}{2},j,k}\right)}{\Delta x_{i\pm\frac{1}{2},j,k}}, \tag{3-90}$$

$$v^n_{y_{i,j\pm\frac{1}{2},k}} = 0.006328(\frac{k_y}{\mu})^n_{i,j\pm\frac{1}{2},k} \frac{\left(\Delta p^n_{i,j\pm\frac{1}{2},k} - \gamma^n_{i,j\pm\frac{1}{2},k} \Delta D_{i,j\pm\frac{1}{2},k}\right)}{\Delta y_{i,j\pm\frac{1}{2},k}}, \tag{3-91}$$

$$v^n_{z_{i,j,k\pm\frac{1}{2}}} = 0.006328(\frac{k_z}{\mu})^n_{i,j,k\pm\frac{1}{2}} \frac{\left(\Delta p^n_{i,j,k\pm\frac{1}{2}} - \gamma^n_{i,j,k\pm\frac{1}{2}} \Delta D_{i,j,k\pm\frac{1}{2}}\right)}{\Delta z_{i,j,k\pm\frac{1}{2}}}, \tag{3-92}$$

$$v^n_{well_{i\pm\frac{1}{2},j,k}} = (0.006328)(\frac{k}{\mu B})^n_{i,j,k} \frac{(p^n_{i,j,k} - p^n_{well_{i,j,k}})}{r_w\left[(1-(\frac{r_w}{r_0})^2)ln(\frac{r_0}{r_w}) + s\right]}, \tag{3-93}$$

and

$$v^n_{well_{i,j,k}} = 2(0.006328)(\frac{k}{\mu B})^n_{i,j,k} \times \frac{\left(p^n_{i,j,k} - p^n_{well_{i,j,k}}\right)}{r_w\left[E_i\left(-\frac{\phi c_t \mu r_0^2}{4\times 2.637\times 10^{-4} k_z t}\right) - E_i\left(-\frac{\phi c_t \mu r_w^2}{4\times 2.637\times 10^{-4} k_z t}\right)\right]}. \tag{3-94}$$

The non-Darcy coefficients, α , are calculated via β and $\hat{\alpha}$ as follows:

$$\beta^n_{x_{i\pm\frac{1}{2},j,k}} = 6.15\times 10^{10}(k_x)^{-1.55}, \tag{3-95}$$

$$\beta^n_{y_{i,j\pm\frac{1}{2},k}} = 6.15\times 10^{10}(k_y)^{-1.55}, \tag{3-96}$$

$$\beta^n_{z_{i,j,k\pm\frac{1}{2}}} = 6.15\times 10^{10}(k_z)^{-1.55}, \tag{3-97}$$

$$\hat{\alpha}^n_{x_{i\pm\frac{1}{2},j,k}} = 1.8295\times 10^{-16} \beta^n_{x_{i\pm\frac{1}{2},j,k}} \rho^n_{i\pm\frac{1}{2},j,k} (\frac{k_x}{\mu})^n_{i\pm\frac{1}{2},j,k} abs(v^n_{x_{i\pm\frac{1}{2},j,k}}), \tag{3-98}$$

$$\hat{\alpha}^n_{y_{i,j\pm\frac{1}{2},k}} = 1.8295\times 10^{-16} \beta^n_{y_{i,j\pm\frac{1}{2},k}} \rho^n_{i,j\pm\frac{1}{2},k} (\frac{k_y}{\mu})^n_{i,j\pm\frac{1}{2},k} abs(v^n_{y_{i,j\pm\frac{1}{2},k}}), \tag{3-99}$$

$$\hat{\alpha}^n_{z_{i,j,k\pm\frac{1}{2}}} = 1.8295\times10^{-16}\beta^n_{z_{i,j,k\pm\frac{1}{2}}}\rho^n_{i,j,k\pm\frac{1}{2}}(\frac{k_z}{\mu})^n_{i,j,k\pm\frac{1}{2}}abs(v^n_{x_{i,j,k\pm\frac{1}{2}}}), \tag{3-100}$$

$$\alpha^n_{x_{i\pm\frac{1}{2},j,k}} = \frac{\sqrt{(1+4\hat{\alpha}^n_{x_{i\pm\frac{1}{2},j,k}})}-1}{2}, \tag{3-101}$$

$$\alpha^n_{y_{i,j\pm\frac{1}{2},k}} = \frac{\sqrt{(1+4\hat{\alpha}^n_{y_{i,j\pm\frac{1}{2},k}})}-1}{2}, \tag{3-102}$$

and

$$\alpha^n_{z_{i,j,k\pm\frac{1}{2}}} = \frac{\sqrt{(1+4\hat{\alpha}^n_{z_{i,j,k\pm\frac{1}{2}}})}-1}{2}. \tag{3-103}$$

3.3.2 Non-Darcy Coefficients for Two-Phase Flow

The darcy velocities for oil are calculated as follows:

$$v^n_{ox_{i\pm\frac{1}{2},j,k}} = 0.006328(\frac{k_x k_{ro}}{\mu_o})^n_{i\pm\frac{1}{2},j,k}\frac{\Delta y_{i,j,k}\Delta z_{i,j,k}}{\Delta x_{i\pm\frac{1}{2},j,k}}\left(\Delta p^n_{o_{i\pm\frac{1}{2},j,k}} - \gamma^n_{o_{i\pm\frac{1}{2},j,k}}\Delta D_{i\pm\frac{1}{2},j,k}\right), \tag{3-104}$$

$$v^n_{oy_{i,j\pm\frac{1}{2},k}} = 0.006328(\frac{k_y k_{ro}}{\mu_o})^n_{i,j\pm\frac{1}{2},k}\frac{\Delta x_{i,j,k}\Delta z_{i,j,k}}{\Delta y_{i,j\pm\frac{1}{2},k}}\left(\Delta p^n_{o_{i,j\pm\frac{1}{2},k}} - \gamma^n_{o_{i,j\pm\frac{1}{2},k}}\Delta D_{i,j\pm\frac{1}{2},k}\right), \tag{3-105}$$

$$v^n_{oz_{i,j,k\pm\frac{1}{2}}} = 0.006328(\frac{k_z k_{ro}}{\mu_o})^n_{i,j,k\pm\frac{1}{2}}\frac{\Delta x_{i,j,k}\Delta y_{i,j,k}}{\Delta z_{i,j,k\pm\frac{1}{2}}}\left(\Delta p^n_{o_{i,j,k\pm\frac{1}{2}}} - \gamma^n_{o_{i,j,k\pm\frac{1}{2}}}\Delta D_{i,j,k\pm\frac{1}{2}}\right), \tag{3-106}$$

$$v^n_{wello_{i,j,k}} = (0.006328)(\frac{kk_{ro}}{\mu_o B_o})^n_{i,j,k}\frac{(p^n_{o_{i,j,k}} - p^n_{well_{i,j,k}})}{r_w\left[(1-(\frac{r_w}{r_0})^2)ln(\frac{r_0}{r_w})+s\right]}, \tag{3-107}$$

and

$$v^n_{wello_{i,j,k}} = 2(0.006328)\left(\frac{kk_{ro}}{\mu_o B_o}\right)^n_{i,j,k}$$
$$\times \frac{\left(p^n_{o_{i,j,k}} - p^n_{well_{i,j,k}}\right)}{r_w\left[E_i\left(-\frac{\phi c_t r_0^2}{4\times 2.637\times 10^{-4}\lambda k_z t}\right) - E_i\left(-\frac{\phi c_t r_w^2}{4\times 2.637\times 10^{-4}\lambda k_z t}\right)\right]} . \quad (3\text{-}108)$$

The non-Darcy coefficients, α , for oil are calculated via β and $\hat{\alpha}$ as follows:

$$\beta^n_{ox_{i\pm\frac{1}{2},j,k}} = 6.15\times 10^{10}(k_x k^n_{ro_{i\pm\frac{1}{2},j,k}})^{-1.55} , \quad (3\text{-}109)$$

$$\beta^n_{oy_{i,j\pm\frac{1}{2},k}} = 6.15\times 10^{10}(k_y k^n_{ro_{i,j\pm\frac{1}{2},k}})^{-1.55} , \quad (3\text{-}110)$$

$$\beta^n_{oz_{i,j,k\pm\frac{1}{2}}} = 6.15\times 10^{10}(k_z k^n_{ro_{i,j,k\pm\frac{1}{2}}})^{-1.55} , \quad (3\text{-}111)$$

$$\hat{\alpha}^n_{ox_{i\pm\frac{1}{2},j,k}} = 1.8295\times 10^{-16}\beta^n_{ox_{i\pm\frac{1}{2},j,k}}\rho^n_{o_{i\pm\frac{1}{2},j,k}}\left(\frac{k_x k_{ro}}{\mu_o}\right)^n_{i\pm\frac{1}{2},j,k} abs(v^n_{ox_{i\pm\frac{1}{2},j,k}}) , \quad (3\text{-}112)$$

$$\hat{\alpha}^n_{oy_{i,j\pm\frac{1}{2},k}} = 1.8295\times 10^{-16}\beta^n_{oy_{i,j\pm\frac{1}{2},k}}\rho^n_{o_{i,j\pm\frac{1}{2},k}}\left(\frac{k_y k_{ro}}{\mu_o}\right)^n_{i,j\pm\frac{1}{2},k} abs(v^n_{oy_{i,j\pm\frac{1}{2},k}}) , \quad (3\text{-}113)$$

$$\hat{\alpha}^n_{oz_{i,j,k\pm\frac{1}{2}}} = 1.8295\times 10^{-16}\beta^n_{oz_{i,j,k\pm\frac{1}{2}}}\rho^n_{o_{i,j,k\pm\frac{1}{2}}}\left(\frac{k_z k_{ro}}{\mu_o}\right)^n_{i,j,k\pm\frac{1}{2}} abs(v^n_{ox_{i,j,k\pm\frac{1}{2}}}) , \quad (3\text{-}114)$$

$$\alpha^n_{ox_{i\pm\frac{1}{2},j,k}} = \frac{\sqrt{(1+4\hat{\alpha}^n_{ox_{i\pm\frac{1}{2},j,k}})} - 1}{2} , \quad (3\text{-}115)$$

$$\alpha^n_{oy_{i,j\pm\frac{1}{2},k}} = \frac{\sqrt{(1+4\hat{\alpha}^n_{oy_{i,j\pm\frac{1}{2},k}})} - 1}{2} , \quad (3\text{-}116)$$

and

$$\alpha^n_{oz_{i,j,k\pm\frac{1}{2}}} = \frac{\sqrt{(1+4\hat{\alpha}^n_{oz_{i,j,k\pm\frac{1}{2}}})} - 1}{2} . \quad (3\text{-}117)$$

The darcy velocities for gas are calculated as follows:

$$v^n_{gx_{i\pm\frac{1}{2},j,k}} = 0.006328(\frac{k_x k_{rg}}{\mu_g})^n_{i\pm\frac{1}{2},j,k} \frac{\Delta y_{i,j,k}\Delta z_{i,j,k}}{\Delta x_{i\pm\frac{1}{2},j,k}}\left(\Delta p^n_{g_{i\pm\frac{1}{2},j,k}} - \gamma^n_{g_{i\pm\frac{1}{2},j,k}}\Delta D_{i\pm\frac{1}{2},j,k}\right), \quad (3\text{-}118)$$

$$v^n_{gy_{i,j\pm\frac{1}{2},k}} = 0.006328(\frac{k_y k_{rg}}{\mu_g})^n_{i,j\pm\frac{1}{2},k} \frac{\Delta x_{i,j,k}\Delta z_{i,j,k}}{\Delta y_{i,j\pm\frac{1}{2},k}}\left(\Delta p^n_{g_{i,j\pm\frac{1}{2},k}} - \gamma^n_{g_{i,j\pm\frac{1}{2},k}}\Delta D_{i,j\pm\frac{1}{2},k}\right), \quad (3\text{-}119)$$

$$v^n_{gz_{i,j,k\pm\frac{1}{2}}} = 0.006328(\frac{k_z k_{rg}}{\mu_g})^n_{i,j,k\pm\frac{1}{2}} \frac{\Delta x_{i,j,k}\Delta y_{i,j,k}}{\Delta z_{i,j,k\pm\frac{1}{2}}}\left(\Delta p^n_{g_{i,j,k\pm\frac{1}{2}}} - \gamma^n_{g_{i,j,k\pm\frac{1}{2}}}\Delta D_{i,j,k\pm\frac{1}{2}}\right), \quad (3\text{-}120)$$

$$v^n_{wel\,lg_{i,j,k}} = (0.006328)(\frac{kk_{rg}}{\mu_g B_g})^n_{i,j,k} \frac{(p^n_{g_{i,j,k}} - p^n_{well_{i,j,k}})}{r_w\left[(1-(\frac{r_w}{r_0})^2)ln(\frac{r_0}{r_w}) + s\right]}, \quad (3\text{-}121)$$

and

$$v^n_{wel\,lg_{i,j,k}} = 2(0.006328)(\frac{kk_{rg}}{\mu_g B_g})^n_{i,j,k} \times \frac{\left(p^n_{g_{i,j,k}} - p^n_{well_{i,j,k}}\right)}{r_w\left[E_i\left(-\frac{\phi c_t r_0^2}{4\times 2.637\times 10^{-4}\lambda k_z t}\right) - E_i\left(-\frac{\phi c_t r_w^2}{4\times 2.637\times 10^{-4}\lambda k_z t}\right)\right]}. \quad (3\text{-}122)$$

The non-Darcy coefficients, α , for gas are calculated via β and $\hat{\alpha}$ as follows:

$$\beta^n_{gx_{i\pm\frac{1}{2},j,k}} = 6.15\times 10^{10}(k_x k^n_{rg_{i\pm\frac{1}{2},j,k}})^{-1.55}, \quad (3\text{-}123)$$

$$\beta^n_{gy_{i,j\pm\frac{1}{2},k}} = 6.15\times 10^{10}(k_y k^n_{rg_{i,j\pm\frac{1}{2},k}})^{-1.55}, \quad (3\text{-}124)$$

$$\beta^n_{gz_{i,j,k\pm\frac{1}{2}}} = 6.15\times 10^{10}(k_z k^n_{rg_{i,j,k\pm\frac{1}{2}}})^{-1.55}, \quad (3\text{-}125)$$

$$\hat{\alpha}^n_{gx_{i\pm\frac{1}{2},j,k}} = 1.8295\times 10^{-16}\beta^n_{gx_{i\pm\frac{1}{2},j,k}}\rho^n_{g_{i\pm\frac{1}{2},j,k}}(\frac{k_x k_{rg}}{\mu_g})^n_{i\pm\frac{1}{2},j,k} abs(v^n_{gx_{i\pm\frac{1}{2},j,k}}), \quad (3\text{-}126)$$

$$\hat{\alpha}^n_{gy_{i,j\pm\frac{1}{2},k}} = 1.8295\times10^{-16}\beta^n_{gy_{i,j\pm\frac{1}{2},k}}\rho^n_{g_{i,j\pm\frac{1}{2},k}}\left(\frac{k_y k_{rg}}{\mu_g}\right)^n_{i,j\pm\frac{1}{2},k} abs(v^n_{gy_{i,j\pm\frac{1}{2},k}}), \tag{3-127}$$

$$\hat{\alpha}^n_{gz_{i,j,k\pm\frac{1}{2}}} = 1.8295\times10^{-16}\beta^n_{gz_{i,j,k\pm\frac{1}{2}}}\rho^n_{g_{i,j,k\pm\frac{1}{2}}}\left(\frac{k_z k_{rg}}{\mu_g}\right)^n_{i,j,k\pm\frac{1}{2}} abs(v^n_{gx_{i,j,k\pm\frac{1}{2}}}), \tag{3-128}$$

$$\alpha^n_{gx_{i\pm\frac{1}{2},j,k}} = \frac{\sqrt{(1+4\hat{\alpha}^n_{gx_{i\pm\frac{1}{2},j,k}})}-1}{2}, \tag{3-129}$$

$$\alpha^n_{gy_{i,j\pm\frac{1}{2},k}} = \frac{\sqrt{(1+4\hat{\alpha}^n_{gy_{i,j\pm\frac{1}{2},k}})}-1}{2}, \tag{3-130}$$

and

$$\alpha^n_{gz_{i,j,k\pm\frac{1}{2}}} = \frac{\sqrt{(1+4\hat{\alpha}^n_{gz_{i,j,k\pm\frac{1}{2}}})}-1}{2}. \tag{3-131}$$

3.4 Rock and Fluid Properties

A simulation model requires several input data like rock and fluid properties. These properties are calculated using the following equations below added to the simulator. The capillary pressures are calculated using the Bensten and Anli suggested expression defined below[34]:

$$P_{cog}(s_o) = p_{th} - p_{sp}\ln\left(\frac{S_o - S_{or}}{1 - S_{or}}\right). \tag{3-132}$$

Relative permeabilities for oil and gas are calculated using the Brooks and Corey equation as shown below[35]:

$$k_{ro}(s_o) = k^*_{ro}\left(\frac{S_o - S_{or}}{1 - S_{or}}\right)^{no}, \tag{3-133}$$

and

$$k_{rg}\left(s_g\right) = k_{rg}^*\left(\frac{S_g - S_{gr}}{1 - S_{or}}\right)^{ng} . \tag{3-134}$$

The oil and gas formation factors and densities are calculated using the following equations.

$$B_o\left(p\right) = B_{ob}\left(1 - c_o\left(p - p_b\right)\right), \tag{3-135}$$

$$B_g\left(p\right) = 0.02829\frac{ZT}{p}, \tag{3-136}$$

$$\rho_o\left(p\right) = \rho_{ob}\left(1 + c_o\left(p - p_b\right)\right), \tag{3-137}$$

and

$$\rho_g\left(p\right) = \frac{pM_{wt}}{ZRT} . \tag{3-138}$$

The oil and gas gradients are calculated from the oil and gas densities.

$$\gamma_o = \frac{\rho_o}{144}, \tag{3-139}$$

and

$$\gamma_g = \frac{\rho_g}{144} . \tag{3-140}$$

The equation below is used to find the coefficient of isothermal compressibility of gases.

$$c_g\left(p\right) = \frac{1}{p} - \frac{1}{Z}\frac{\partial Z}{\partial p} . \tag{3-141}$$

3.5 Reservoir, Well and Grid Structures

Different local grid refinements are used in this dissertation to study their effect on the pressure-transient behavior of the wells. Log-distributed grid in addition to user-choice was used to define the grids. The equations below generate log-distributed grid in the y- and z- directions, while uniform grid was used in the x-direction.

Y-direction

$$Y(j) = Y_w e^{(j\Delta U)} \tag{3-142}$$

for $j = 0, 1, 2, \ldots\ldots, j_{size}$,

where

$$\Delta U = \frac{1}{j_{size}} \ln\left(\frac{Y_e}{Y_w}\right), \tag{3-143}$$

$$Y_w = \Delta Y_{jwell}, \tag{3-144}$$

and

Y_e is the drainage distance from the well to the reservoir boundaries in j-direction.

The numerical grid sizes in the y-direction are calculated as follows:

$$\Delta Y_{jwell-\frac{1}{2}} = Y(j) - Y(j-1), \tag{3-145}$$

and

$$\Delta Y_{jwell+\frac{1}{2}} = Y(j) - Y(j-1) \tag{3-146}$$

for $j = 1, 2, \ldots\ldots, j_{size}$,

where

j_{well} is the j-location of the well.

j_{size} is the maximum number of grids for half space between the horizontal well and reservoir boundaries in the j-direction.

Z-direction

$$Z(k) = Z_w e^{(k\Delta U)} \tag{3-147}$$

for $k = 0, 1, 2, \ldots\ldots, k_{size}$,

where

$$\Delta U = \frac{1}{k_{size}} \ln\left(\frac{Z_e}{Z_w}\right), \tag{3-148}$$

$$Z_w = \Delta Z_{kwell}, \tag{3-149}$$

and

Z is the drainage distance from the well to the reservoir boundaries in k-direction. The numerical grid sizes in the z-direction are generated as shown below.

$$\Delta Z_{kwell-\frac{1}{2}} = Z(k) - Z(k-1). \tag{3-150}$$

$$\Delta Z_{kwell+\frac{1}{2}} = Z(k) - Z(k-1) \tag{3-151}$$

for $k = 1, 2, \ldots\ldots, k_{size}$.

where

k_{well} is the k-location of the well.

k_{size} is the maximum number of grids for half space between the horizontal well and reservoir boundaries in the k-direction.

3.6 Time-step Representation

Log-distributed time-stepping was used in addition to the user-choice to generate the time steps. The equations below show the log-distributed technique.

$$\Delta\tau = \frac{1}{N_{\max} - 1} \ln\left(\frac{t_{\max}}{\Delta t_1}\right), \tag{3-152}$$

where

$$t_n = \Delta t_1 e^{(n-1)\Delta\tau}, \tag{3-153}$$

and

$$\Delta t_n = t_n - t_{n-1} \tag{3-154}$$

for $n = 1, 2, \ldots\ldots, N_{\max}$.

Chapter 4
WELL INDICES AND GRID STRUCTURES FOR HORIZONTAL WELLS

The main objective of this research is to study the pressure-transient performance of horizontal wells with complex geometries in complex structures under single- and two-phase fluid flow conditions. In order to obtain accurate pressure-transient behavior of horizontal wells from numerical models, bottom-hole flowing pressure of the well should be accurately related to the grid block pressure. This is accomplished by using well indices. The objective of this chapter is to investigate the choice of different well indices, grid structures and time steps to enhance the numerical simulation of horizontal well tests.

In the first section of this chapter, two different well indices are used: conventional well index (WI) and transient well index (TWI). Transient well index is a relatively new concept used for vertical wells[2] and is applied to horizontal wells in this study. These indices are investigated with the use of different grid refinements, time step selections and equivalent wellbore radius equations. Several cases are run to reach the optimum numerical model that gives closer match to the analytical solution. The results obtained from this work help us to construct the numerical model to be used in the investigation of pressure-transient performance of horizontal wells with complex geometries in complex structures.

The second section describes the grid structures used to model anticlines and curved horizontal wells. Horizontal wells can have simple curvature or undulations. The existence of a gas cap is also considered in the models.

4.1 Representation of Horizontal Wells in Grid Block

In this section, well indices are compared and tested to obtain reliable horizontal well test models. Two types of well indices have been used: conventional well index (WI) and transient well index (TWI). These indices were applied with different grid refinements, time-steps, and equivalent wellbore radius equations. These cases used straight horizontal well in horizontal slab reservoir for single-phase flow (Fig. 4-1). The results were compared with the analytical solution (Eq. 3-11) for model verification.

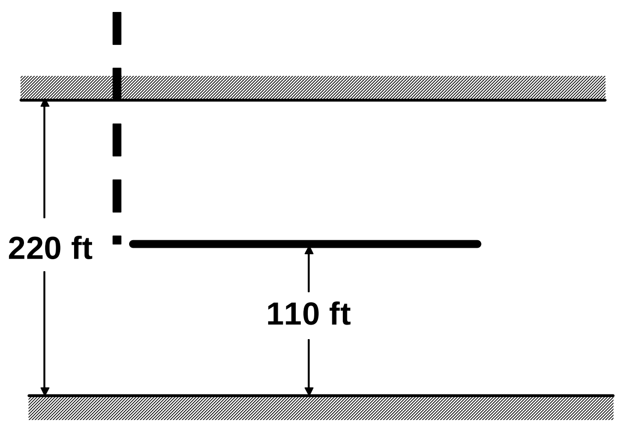

Figure 4- 1. Straight horizontal well in a 220-ft thick slab structure; single-phase.

The data used for the simulations in this study are shown in Tables 4-1 and 4-2. The porosity, formation and fluid compressibilities, wellbore radius and surface roughness are kept the same for various simulated cases as presented in Table 4-1.

Table 4- 1. Constant properties used in the simulations.

Porosity, ϕ, fraction	0.2
Formation compressibility, c_ϕ, psi^{-1}	4 x 10^{-6}
Oil compressibility, c_o, psi^{-1}	1 x 10^{-5}
Oil formation volume factor, B_o, bbl/stb	1.0
Gas formation volume factor, B_g, cf/scf	1.0
Oil viscosity, μ_o, cp	1.0
Gas viscosity, μ_g, cp	0.02
Formation temperature, T, °F	120
Wellbore radius, r_w, ft	0.25
Wellbore surface roughness, ε_D	0.002

Table 4-2 shows the permeabilities, dimensions of the reservoir, and the length and rate of the horizontal well for the investigation of well indices and sensitivity runs.

Table 4- 2. Reservoir and well properties for the infinite-conductivity horizontal wells in a 220-ft thick slab structure.

Permeability in x-direction, k_x, md	20
Permeability in y-direction, k_y, md	20
Permeability in z-direction, k_z, md	5
Formation thickness, h, ft	220
Formation size in the x-direction, x_e, ft	6000
Formation size in the y-direction, y_e, ft	6000
Horizontal well length, L, ft	2000
Total flow rate, q, scf/d	2000

4.1.1 Conventional Well Index (WI)

Several cases were run using WI (Eqs. 3-21 and 3-35) with equivalent wellbore radius (Eq. 3-11) and applying different grid refinements and time steps. For grid refinement and time steps, log-distribution and user-choice options were used. The objective is to find a model that gives closer match to the analytical solution. Six cases were needed to reach the optimum model beyond which the match dose not improve.

Case WI – 1:

The grid structure of the model is shown in Fig. 4-2. It has uniform grids in x-, y-, and z-directions (500, 461.54, and 31.43 ft, respectively). Equal time steps intervals were used for this case.

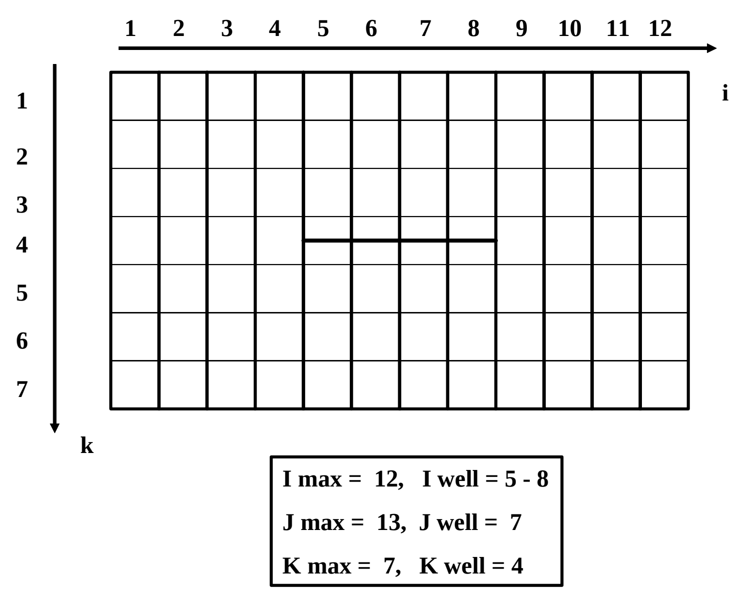

Figure 4- 2. Grid structure for a straight horizontal well in a 220-ft thick slab structure; Case WI – 1.

Fig. 4-3 shows the pressure-transient responses for Case WI – 1 and the analytical solution for the same case. The numerical model does not match the analytical solution during early times. Flat pressure and unit-slope derivative indicate poor numerical representation of the well. During the late-time region, t ≥ 10 hr, however, very good match is observed.

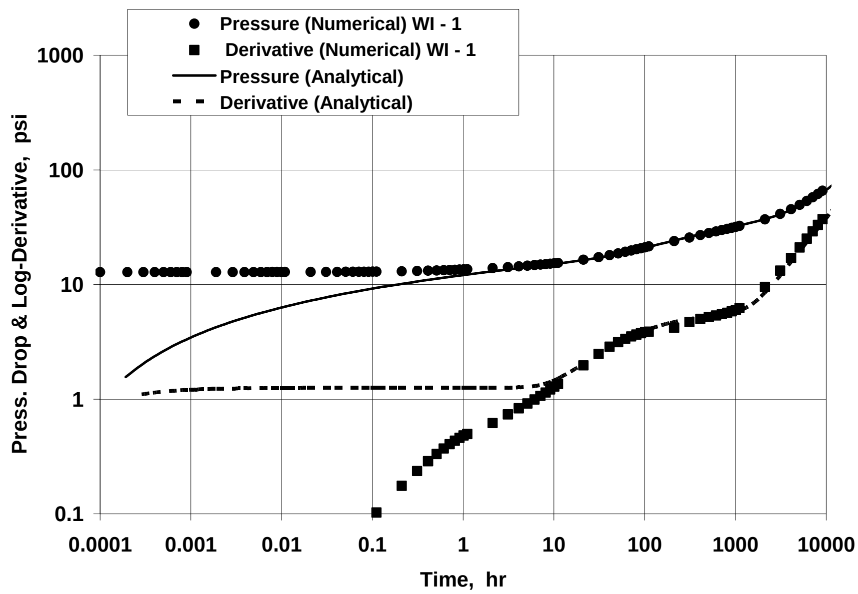

Figure 4- 3. Pressure-transient responses for a straight horizontal well in a 220-ft thick slab structure; Case WI – 1.

In summary, numerical model does not reproduce early-time radial flow behavior but becomes reasonably accurate after the start of intermediate-time linear flow.

Case WI – 2:

The grid structure of Case WI – 1 was used for this case but with different time-steps. The log-distributed time step method was applied by using Eq.3-152. This run shows no improvement on the pressure-transient behavior (Fig. 4-4) as compared with the previous case.

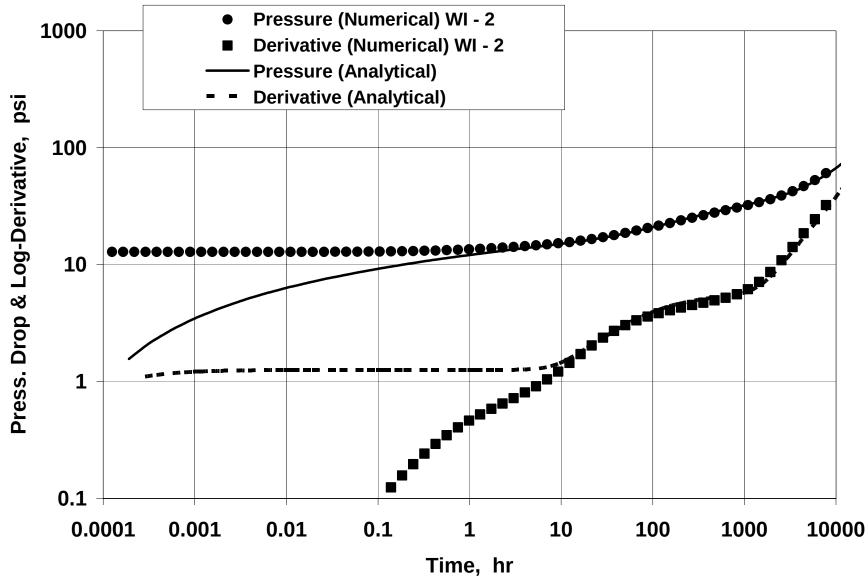

Figure 4- 4. Pressure-transient responses for a straight horizontal well in a 220-ft reservoir thick structure; Case WI – 2.

<u>Case WI – 3:</u>

A combination of log-distributed and user-choice time steps was used for the same grid system in Case WI – 1. As shown in Fig. 4.5, no improvement on the pressure-transient behavior is observed.

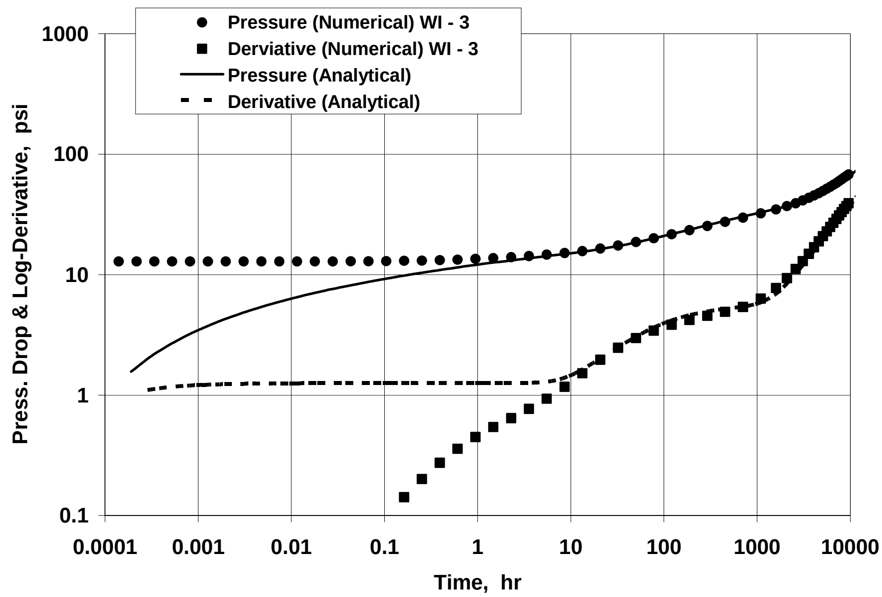

Figure 4- 5. Pressure-transient responses for a straight horizontal well in a 220-ft thick slab structure; Case WI – 3.

Based on these observations, it can be concluded the accuracy of the model is not very sensitive to the selection of time-steps. Therefore, the time steps applied for Case WI – 3 were applied for the rest of the cases with different grid refinements.

Case WI – 4:

The purpose of this case is to test different grid structures to see the effect on the pressure-transient behavior. Fig. 4-6 shows the grid structure for this case. Finer grids were applied manually around the well. The grid size in y-direction increases from 20 ft around the wellblock to 40, 390, 1000 ft and 1500 ft at the boundary. The grid dimensions in the z-direction are the same as those in the y-direction (for z-direction, the maximum grid size is 40 ft). Uniform grid distribution was used in the x-direction. The number of grids was kept the same in the x-, y- and z-directions.

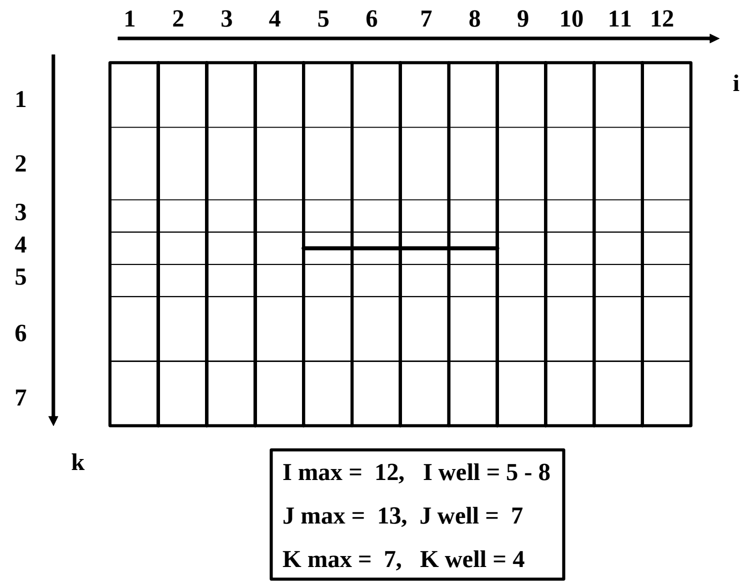

Figure 4- 6. Grid structure for a straight horizontal well in a 220-ft thick slab structure; Case WI – 4.

Case WI – 4 shows an improvement on the match with analytical solution for $t \geq 0.1$ hr (Fig. 4-7) as compared with the previous cases. The straight pressure and unit-slope derivative of the numerical solution still exists but at earlier times. Based on this result, more grid refinements were applied to improve the pressure behavior at early times.

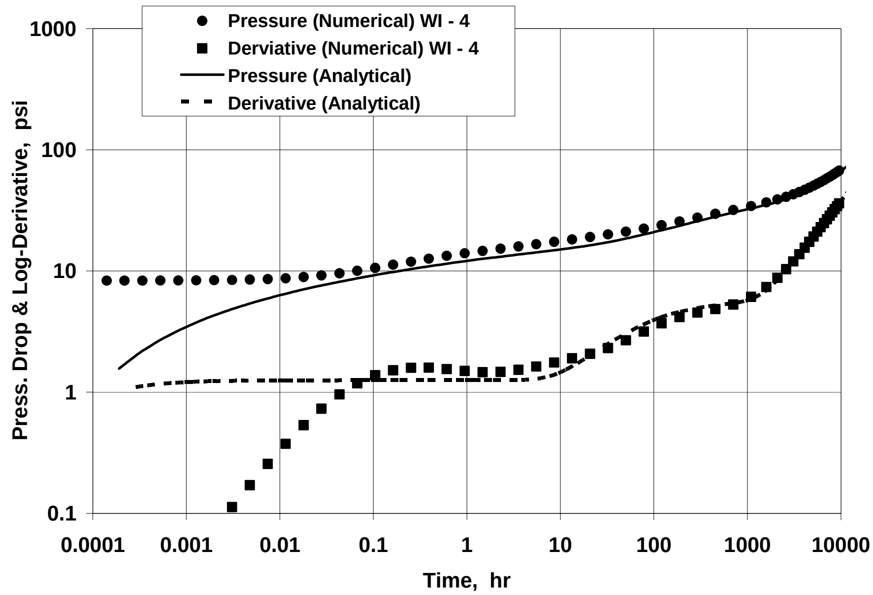

Figure 4- 7. Pressure-transient responses for a straight horizontal well in a 220-ft thick slab structure; Case WI – 4.

<u>Case WI – 5:</u>

The same grid structure as Case WI – 4 was applied but with finer uniform wellblock grid (250 ft) in the x-direction. This brings the total number of grids in x-direction to 16 as shown in Fig.4-8.

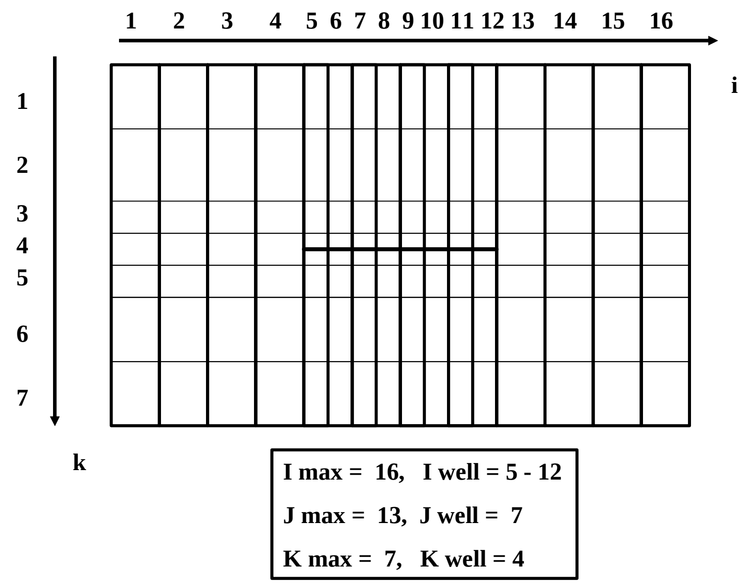

Figure 4- 8. Grid structure for a straight horizontal well in a 220-ft thick slab structure; case WI – 5.

The grid refinement used in Case WI – 5 does not improve the pressure-transient behavior of the numerical solution (Fig. 4-9) as compared with Case WI – 4. This means finer grids in x-direction will not improve the results. Therefore, the uniform grid distribution in the x-direction (500 ft) of the previous cases was used for the rest of the cases. In addition, finer grids were applied in the y- and z- directions which are the directions of flow toward the well to improve the pressure-transient behavior during the early-time radial flow.

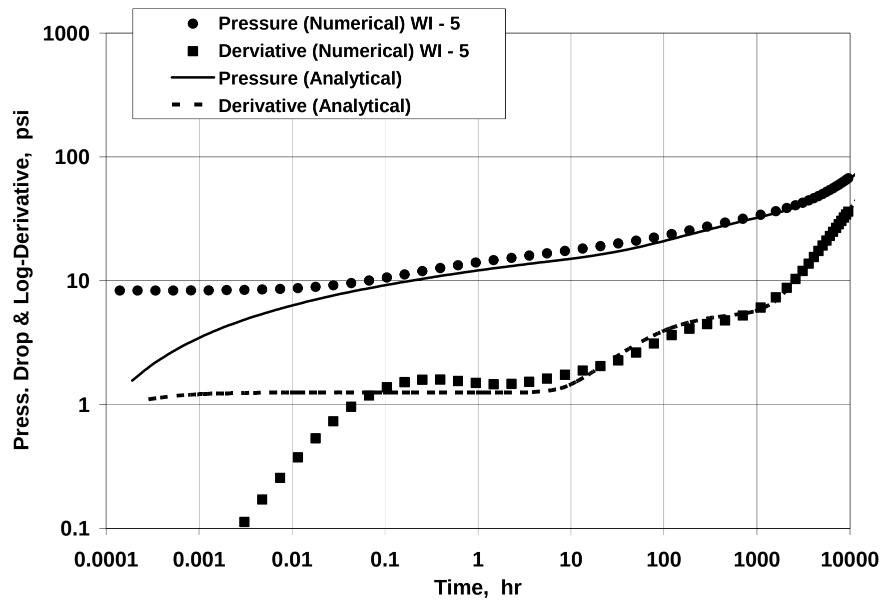

Figure 4- 9. Pressure-transient responses for a straight horizontal well in a 220-ft thick slab structure; Case WI – 5.

<u>Case WI – 6:</u>

To create a finer but gradually increasing grid structure for this case, log-distributed grids were applied to Case WI – 5. This method generates grids in the y- and z-directions (Fig. 4-10) using Eqs. 3-142 and 3-147 with square y-z wellblock of 1 ft^2. This increases the number of grids in the y- direction to 17 and z-direction to 13.

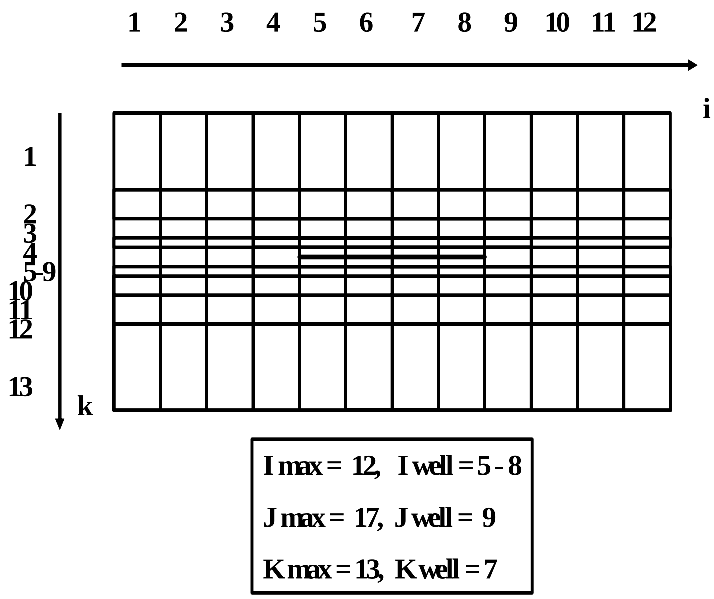

Figure 4- 10. Grid structure for a straight horizontal well in a 220-ft thick slab structure; Case WI – 6.

Case WI – 6 in Fig.4-11 shows an improvement on the pressure-transient behavior for early times, $t \leq 0.1$ hr. The flat pressure and unit-slop derivative of the numerical solution observed in the previous cases in the early-time region disappeared yielding a better match with the analytical solution. The difference observed in the early-time data between simulation and analytical results may be attributed to the fact that the simulation uses finite-wellbore radius and analytical solution assumes a line- source.

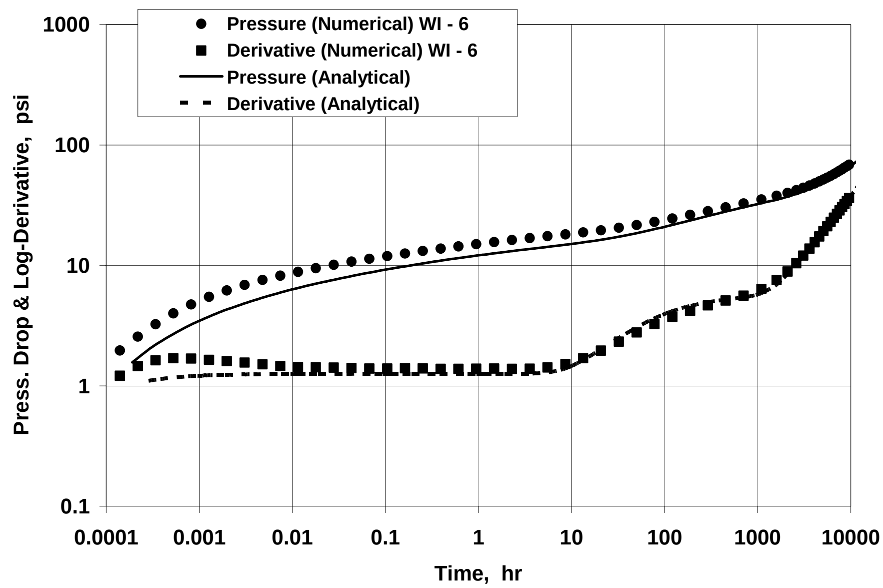

Figure 4- 11. Pressure-transient responses for a straight horizontal well in a 220-ft thick slab structure; Case WI – 6.

Based on the results found with these cases, Case WI – 6 was chosen as the optimum model for WI of its best performance. Transient well index (TWI), however, will be investigated and compared with Case WI – 6 in the following section.

4.1.2 Transient Well Index (TWI)

In this section, the transient well index (Eqs. 3-22 and 3-36) was investigated for straight horizontal wells in horizontal slab reservoir (Fig. 4-1) through several cases. These cases used several equivalent wellbore radius equations and different grid structures. In addition, log-distributed and user-choice time-steps were applied. Five cases were used to find the model that gives closer match with the analytical solution compared with conventional well index, especially during the early-time region.

<u>Case TWI – 1:</u>

The equivalent wellbore radius shown in Eq. 3-11 with the grid structure for Case WI – 4 (Fig.4-6) was applied for this case. In Fig. 4-12, Case TWI – 1 numerical solution shows very good match to the analytical solution. This result shows no flat pressure and unit-slope derivative during the early-time region as compared with pressure-transient responses for Case WI – 4 (Fig. 4-7). Also with smaller number of grids in the y- and z-directions, no difference in pressure responses were observed between Case TWI – 1 numerical solution and analytical solution during early-time region as compared with Case WI – 6 (Fig. 4-11). The derivative responses for Case TWI – 1, however, are not smooth and have a hump during the early-time region (Fig. 4-12). Therefore, different wellbore radius equations with the same grid structure (Fig. 4-6) will be applied to the following cases to eliminate the hump on the derivative responses.

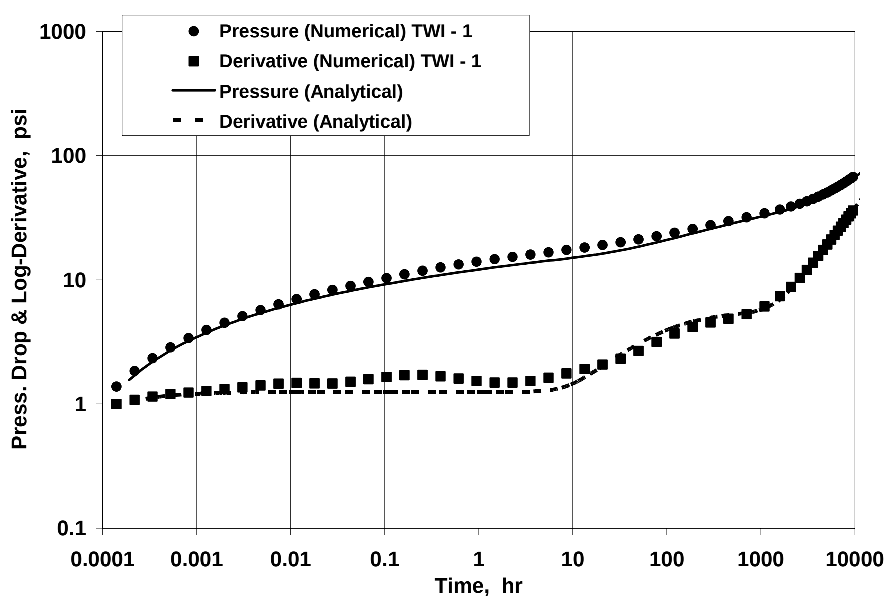

Figure 4- 12. Pressure-transient responses for a straight horizontal well in a 220-ft thick slab structure; Case TWI – 1.

<u>Case TWI – 2:</u>

The equivalent wellbore radius equation shown below[1] was applied to run this model.

$$r_0 = 0.198\Delta y \tag{4-1}$$

As compared with Case TWI – 1 (Fig. 4-12), Case TWI – 2 produces similar pressure responses but with more fluctuations on the derivative responses during the early-time region as shown in Figure 4-13.

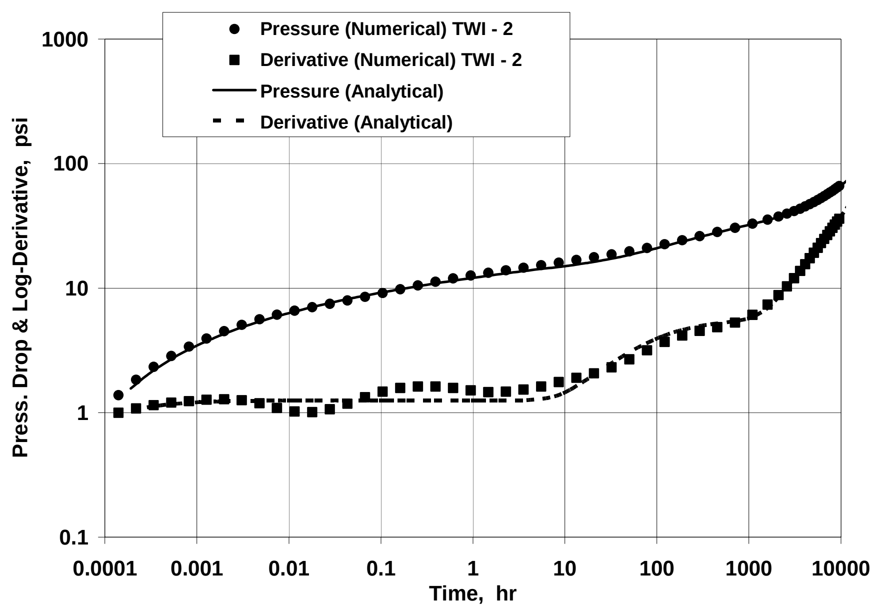

Figure 4- 13. Pressure-transient responses for a straight horizontal well in a 220-ft thick slab structure; Case TWI – 2.

<u>Case TWI – 3:</u>

In order to improve the derivative responses during the early time region, Case TWI – 3 was run with a combination of equivalent wellbore radii defined by Eqs. 1-5 and 3-11. Eq. 1-5 was used at early times and switched with Eq. 3-11 at the start of linear flow. In Fig. 4-14, Case TWI - 3 numerical solution shows unstable derivative responses during the early-time region with bad match to the analytical solution at the very early times. During late-time region, similar to the previous cases, Case TWI - 3 matches the analytical solution for the pressure and derivative responses.

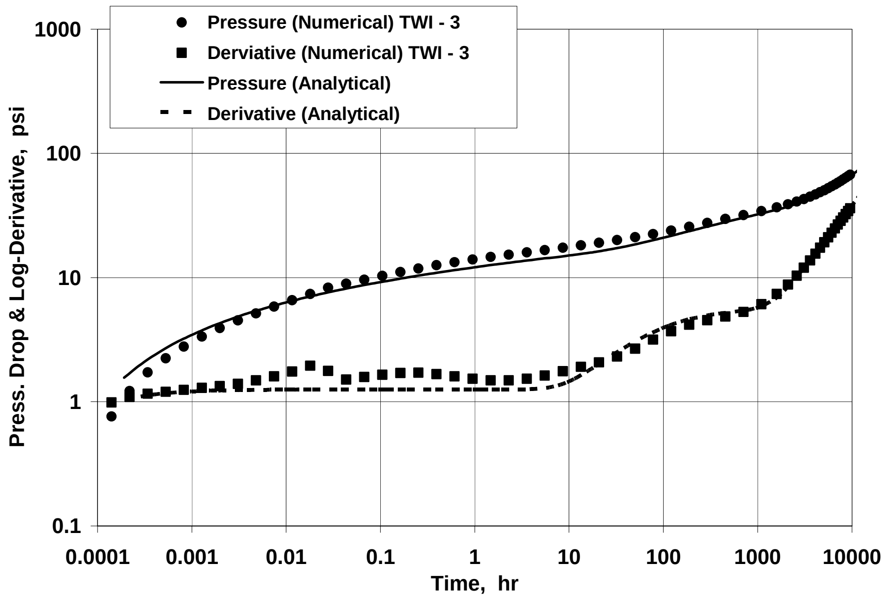

Figure 4- 14. Pressure-transient responses for a straight horizontal well in a 220-ft thick slab structure; Case TWI – 3.

Based on the results found, it is concluded that using different equivalent wellbore radius equations will not improve the derivative behavior. To be more accurate, full transient solution will be applied to solve for the equivalent wellbore radius for the following case.

Case TWI – 4:

Fully transient Ei solution was applied for this case by solving the equivalent wellbore radius with a Newton Raphson method as shown below.

$$x_{i+1} = x_i - \frac{f(x_i)}{f'(x_i)}, \qquad (4\text{-}2)$$

where

$$f(x_i) = -\frac{qB\mu}{4\pi(0.006328)L\Delta p\sqrt{k_y k_z}} Ei\left[-\frac{x_i^2}{4\left(\dfrac{2.637\times10^{-4}k_z}{\phi c_t \mu}t\right)}\right] - 1. \tag{4-3}$$

and x_i and x_{i+1} are the old and new estimate of the equivalent wellbore radius (r_o) for the Newton Raphson method. This method utilizes the Ei solution as the early time pressure response for horizontal wells. The r_o calculated form this method was used at early times and switched to r_o calculated at the start of linear flow.

In Fig. 4-15, The Case TWI – 4 numerical solution matches the analytical solution with more stable derivative responses. This Case generates better pressure-transient behavior as compared with the previous TWI cases in terms of stability of the derivative curves.

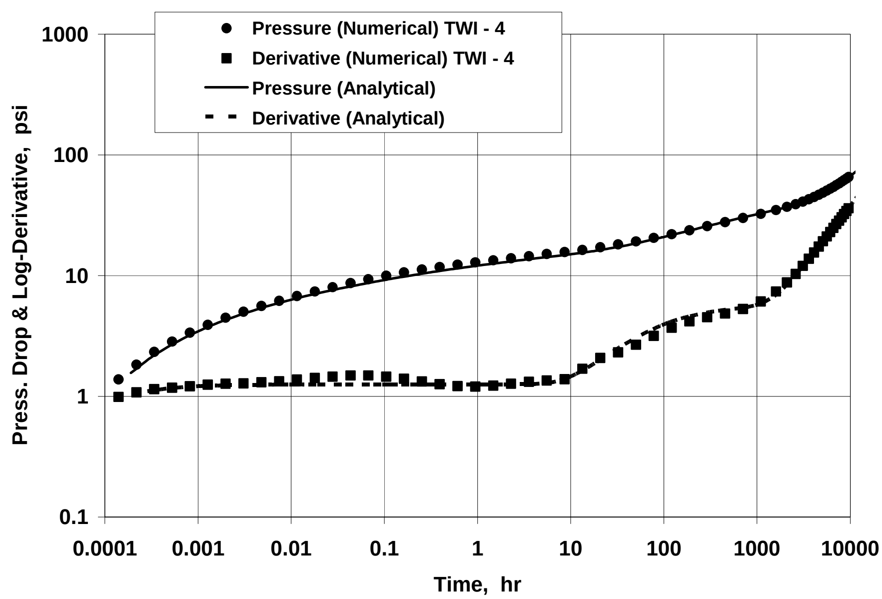

Figure 4- 15. Pressure-transient responses for a straight horizontal well in a 220-ft thick slab structure; Case TWI – 4.

Case TWI – 4 used smaller number of grids (coarser grids shown in Fig. 4.6). As shown in Figs. 4- 11 and 4-15, it generated better match during the early-time region as compared with Case WI – 6 (finer grids shown in Fig. 4-10). Therefore, the finer grid structure (Fig.4-10) is applied to Case TWI – 4 for the following case to study its effect on the transient well index performance.

Case TWI – 5:

Case TWI – 5 used the grid structure of Case WI – 6 (Fig.4-10) and was run to observe the effect on the pressure-transient responses as compared with Case WI – 6. As shown in Fig. 4-16, Case TWI – 5 follows pressure-transient behavior of Case WI – 6. Therefore, the use of the fine grid with transient well index will cause deviation from the analytical results and yield comparable results with conventional well index.

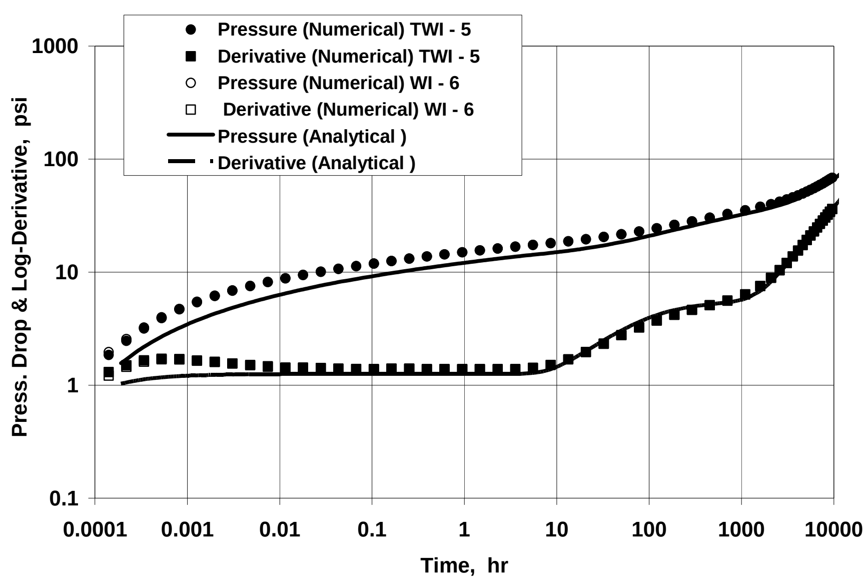

Figure 4- 16. Pressure-transient responses for a straight horizontal well in a 220-ft thick slab structure; Case TWI – 5.

A summary of different well indices investigated in this study and the associated equivalent wellbore radii, time steps, and grid structures is given in Table 4-2.

Table 4- 3. Summary of well indices investigated.

Well model	**Well index Equation**	**Equivalent wellbore radius**	**Time step**	**Grid Structure**
WI-1	Eqs. 3-21 and 3-35	Eq. 3-11	Equal time steps	Figure 4-2
WI-2	Eqs. 3-21 and 3-35	Eq. 3-11	Log-distributed Time step Eq. 3-152	Figure 4-2
WI-3	Eqs. 3-21 and 3-35	Eq. 3-11	Log-distributed plus user choice Time steps	Figure 4-2
WI-4	Eqs. 3-21 and 3-35	Eq. 3-11	Log-distributed plus user choice Time steps	Figure 4-6
WI-5	Eqs. 3-21 and 3-35	Eq. 3-11	Log-distributed plus user choice Time steps	Figure 4-8
WI-6	Eqs. 3-21 and 3-35	Eq. 3-11	Log-distributed plus user choice Time steps	Figure 4-10
TWI-1	Eqs. 3-22 and 3-36	Eq. 3-11	Log-distributed plus user choice Time steps	Figure 4-6
TWI-2	Eqs. 3-22 and 3-36	Eq. 4-1	Log-distributed plus user choice Time steps	Figure 4-6
TWI-3	Eqs. 3-22 and 3-36	Eg.1-5 and switched to Eq. 3-11	Log-distributed plus user choice Time steps	Figure 4-6
TWI-4	Eqs. 3-22 and 3-36	Eqs. 4-2 – 4-3 and fixed r_o after start of linear flow	Log-distributed plus user choice Time steps	Figure 4-6
TWI-5	Eqs. 3-22 and 3-36	Eqs. 4-2 – 4-3 and switched to $r_{o,max.}$	Log-distributed plus user choice Time steps	Figure 4-10

Based on the results found, transient well index generates better match to the analytical solution than conventional well index during early times. On the other hand, both well indices yield similar match during the late time region. As will be discussed in the next chapter, the effect of the well and formation curvature and gas cap manifests itself on the late time (after the start of linear flow) responses of horizontal well. Therefore, the method used in Case WI- 6 will be applied to straight wells in anticlinal structures and curved wells in horizontal slab reservoirs for single and two-phase fluid flow. The following section will describe the grid structure and the models of these runs.

4.2 Grid Structures Used in This Study

Several models were built and simulated to study the effect of the pressure-transient responses of straight horizontal wells in anticlinal structures and curved wells in horizontal slab reservoirs. These models are divided under two categories: well undulation and structure effects. Grid structures for two-phase models (with a gas cap at the top) will also be described.

4.2.1 Well Undulation Effects

The straight, concave downward, and concave upward horizontal well models in horizontal slab reservoirs were used to study the undulation effects.

Straight Well in Horizontal Slab Reservoir:

Figure 4-17 shows the model for the straight horizontal well in slab reservoir.

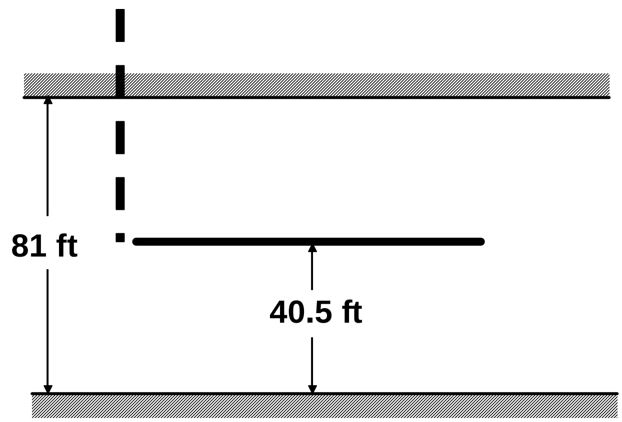

Figure 4- 17. Straight horizontal well in an 81-ft thick slab structure; single-phase.

The grid structure for this model is shown in Fig. 4-18.

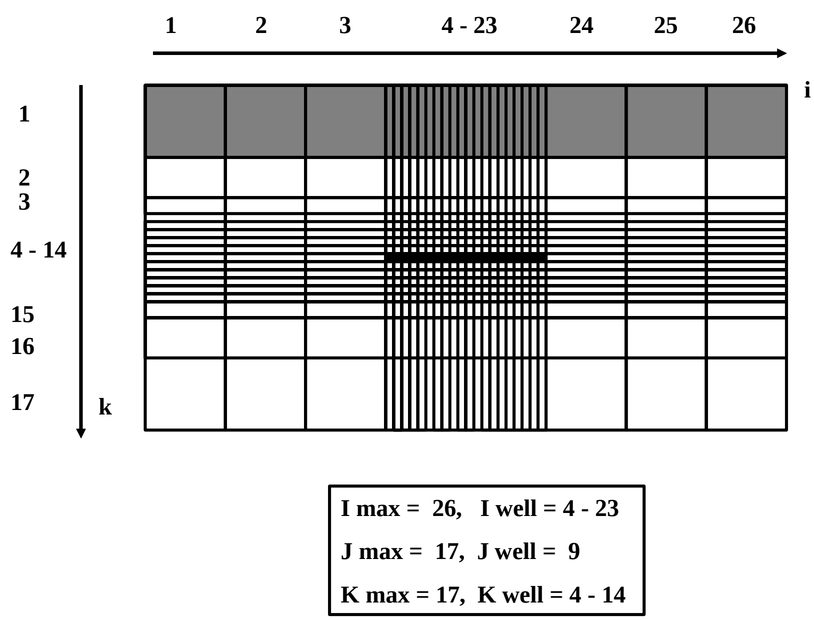

Figure 4- 18. Grid structure for a straight horizontal well in an 81-ft thick slab structure.

For the curved well scenario, the grids in the z-direction were manually refined and adjusted (1, 2, 10 and 23 ft) to accommodate for the curvature of the well. For the same reason, the x-direction grids were set uniform (50 ft for the wellblocks and 500 ft for the formation blocks). The grids in the y-direction, however, were log-distributed with square y-z wellblock of 1 ft^2. The shaded color grid blocks in the grid figures this section represent the gas cap for the two phase models.

Concave Downward Well in Horizontal Slab Reservoir:

The concave downward well in horizontal slab reservoir model was simulated as shown in Fig. 4-19.

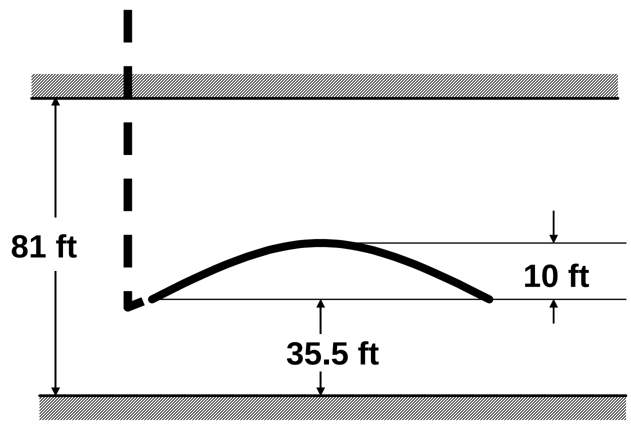

Figure 4- 19. Concave downward well in an 81-ft thick slab structure; single-phase.

The same grid structure for the straight horizontal well model was used for the concave downward well as presented in Fig. 4-20.

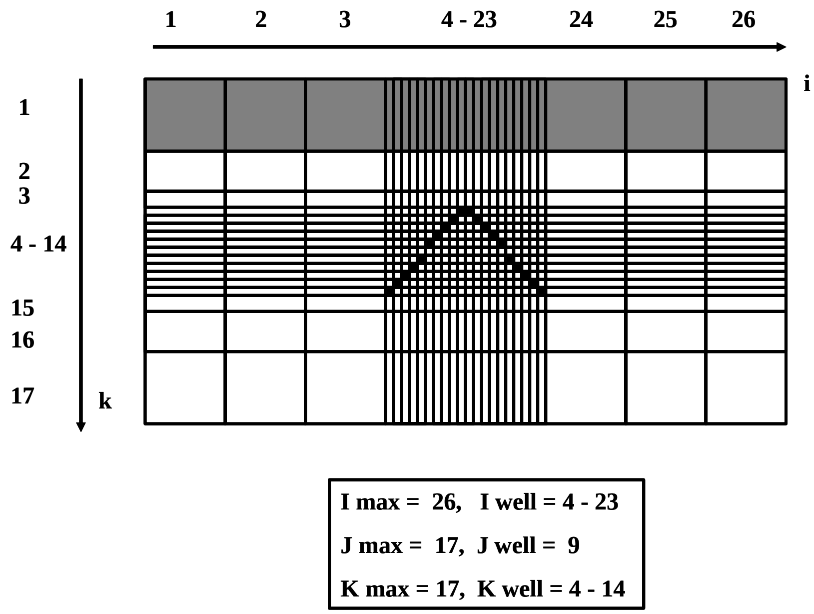

Figure 4- 20. Grid structure for a concave downward well in an 81-ft thick slab structure.

Concave Upward Well in Horizontal Slab Reservoir:

Figure 4-21 shows the model for the concave upward well in horizontal slab reservoir to compare with straight and concave downward wells models.

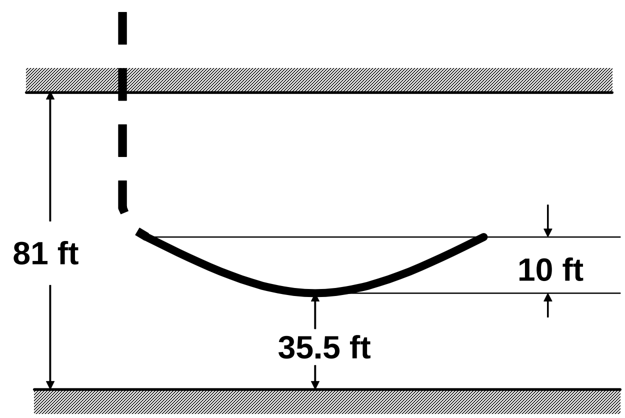

Figure 4- 21. Concave upward well in an 81-ft thick slab structure; single-phase.

Figure 4-22 shows the grid structure for the concave upward well scheme in a horizontal slab reservoir. The grid system as that for a straight well (Fig. 4-16).

.

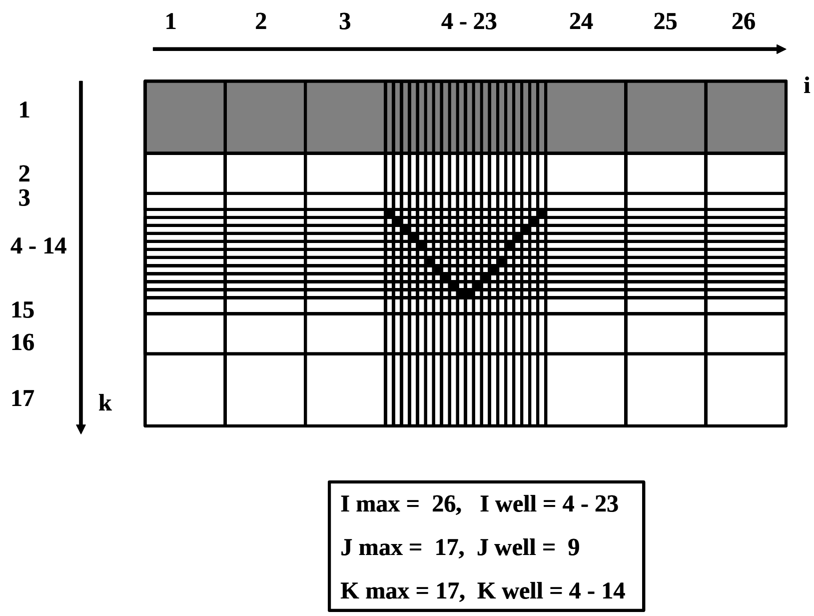

Figure 4- 22. Grid structure for a concave upward well in an 81-ft thick slab structure.

Beside the curved wells, three different sinusoidal well undulations cases were simulated to study their effect on the pressure-transient responses.

<u>2 ½ – Cycle Sinusoidal Undulated Well in Horizontal Slab Reservoir:</u>

The third case shown in Fig. 4-23 is for 2 ½ – cycle sinusoidal in horizontal slab reservoir.

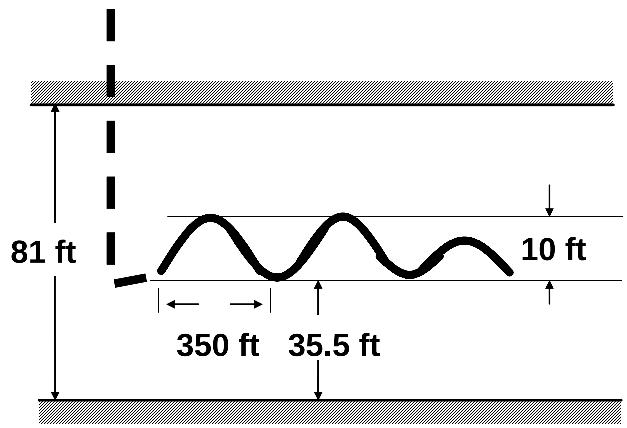

Figure 4- 23. 2 ½ cycle sinusoidal, undulated well in an 81-ft thick slab structure; single-phase.

The grid structure of the curved wells was applied (Figs. 4-20 and 4-22) with different well schemes for sinusoidal well undulation cases. The grid structure of the horizontal slab reservoir with 2 ½ – cycle sinusoidal undulation scheme is shown in Fig. 4-24.

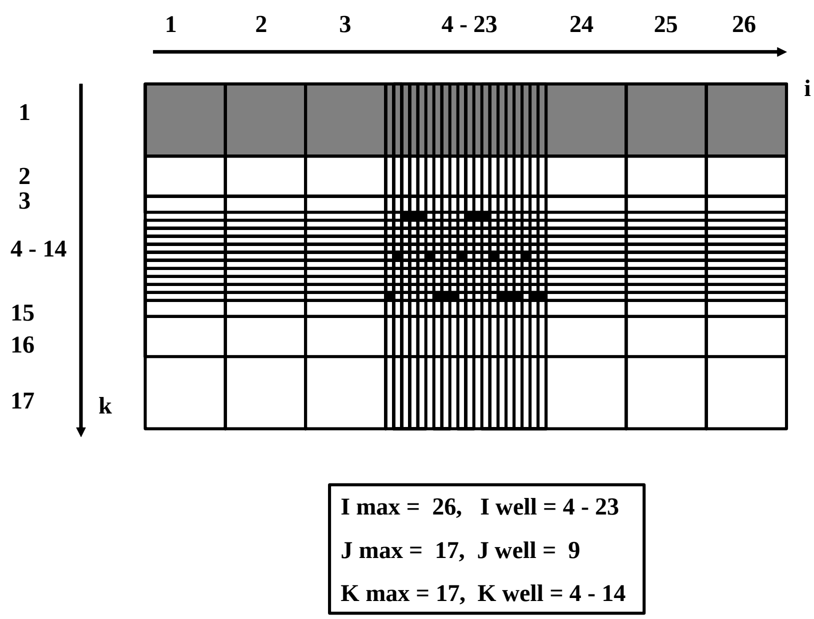

Figure 4- 24. Grid structure for 2 ½ – cycle sinusoidal, undulated well in an 81-ft thick slab structure.

<u>3 – Cycle Sinusoidal Undulated Well in Horizontal Slab Reservoir:</u>

The second case was simulated with 3 sinusoidal cycles in horizontal slab reservoir as presented in Fig. 4-25.

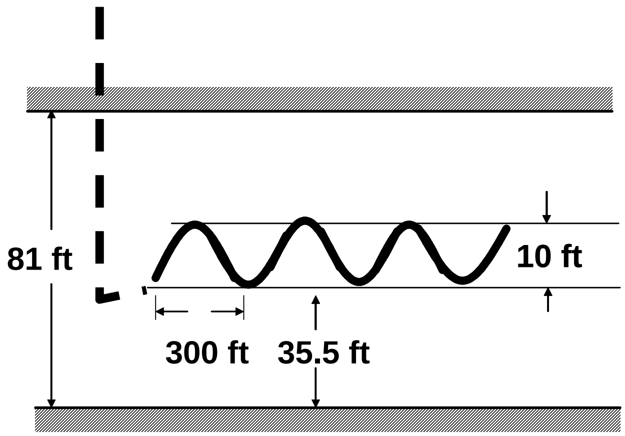

Figure 4- 25. 3 – cycle sinusoidal, undulated well in an 81-ft thick slab structure; single-phase.

Figure 4-26 shows the grid structure for the 3 – cycle undulated well in horizontal slab reservoir.

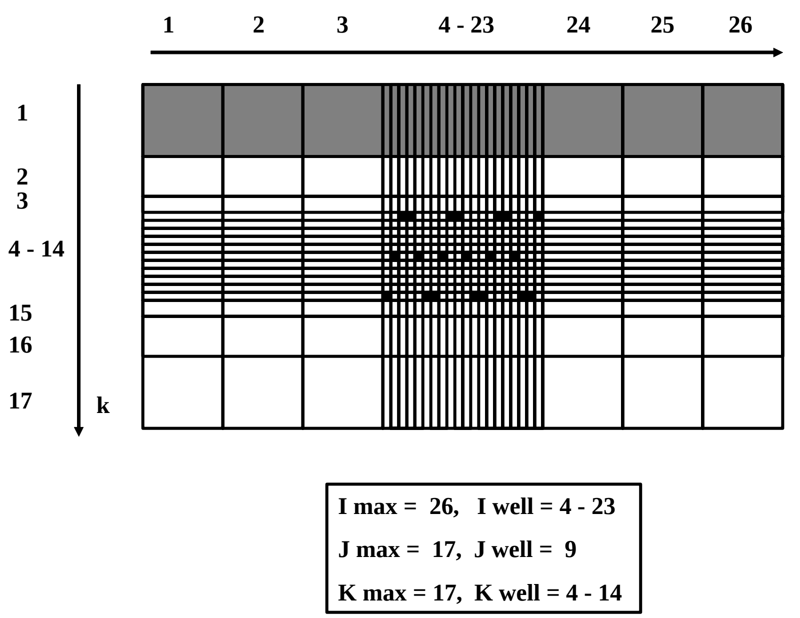

Figure 4- 26. Grid structure for 3 – cycle sinusoidal, undulated well in an 81-ft thick slab structure.

4 ½ – Cycle Sinusoidal Undulated Well in Horizontal Slab Reservoir:

The 4 ½ – cycle undulated well model in horizontal slab reservoir is shown in Fig. 4-27 below.

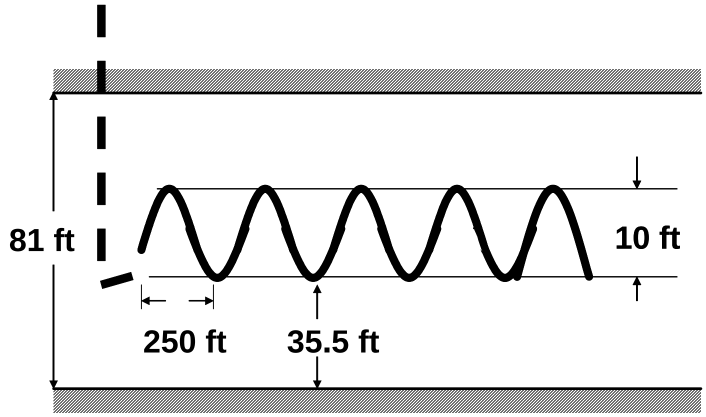

Figure 4- 27. 4 ½ – cycle sinusoidal, undulated well in an 81-ft thick slab structure; single-phase.

The grid structure of the third case for sinusoidal well model is presented in Fig. 4-28.

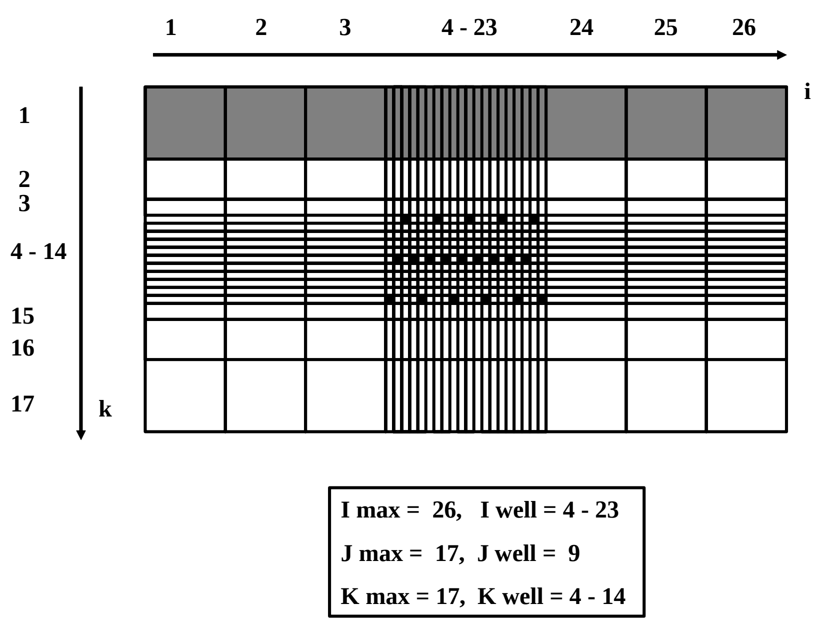

Figure 4- 28. Grid structure for 4 ½ – cycle sinusoidal, undulated well in an 81-ft thick slab structure.

In addition to the study of the well-undulation effects in flat reservoir, the anticline structure effects for the straight wells were investigated in this work. The following section describes the model and the grid structure for the straight wells in horizontal slab reservoirs and anticline structures.

4.2.2 Structure Effects

Straight well in horizontal slab reservoir and anticline structure models were simulated to show the structure effect on the pressure-transient behavior. Figures 4-1 and 4-10 show the model and grid structure for straight well in horizontal slab reservoir respectively. The model for a straight well in an anticline structure is presented below.

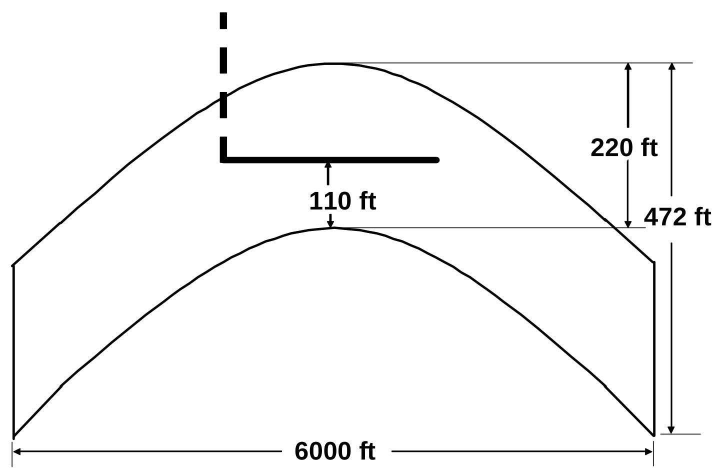

Figure 4- 29. Straight horizontal well in a 220-ft thick anticline structure; single-phase.

Figure 4-30 shows the grid structure for the straight well in an anticline structure. It presents log-distributed grids in z- and y-directions with square y-z wellblock of 1 ft^2. Grid adjustments along the z-direction, however, were needed to draw the anticline structure. Similar to the grid structure for the straight well in a horizontal reservoir (Fig. 4-10), uniform grids of 500 ft were applied in the x-direction.

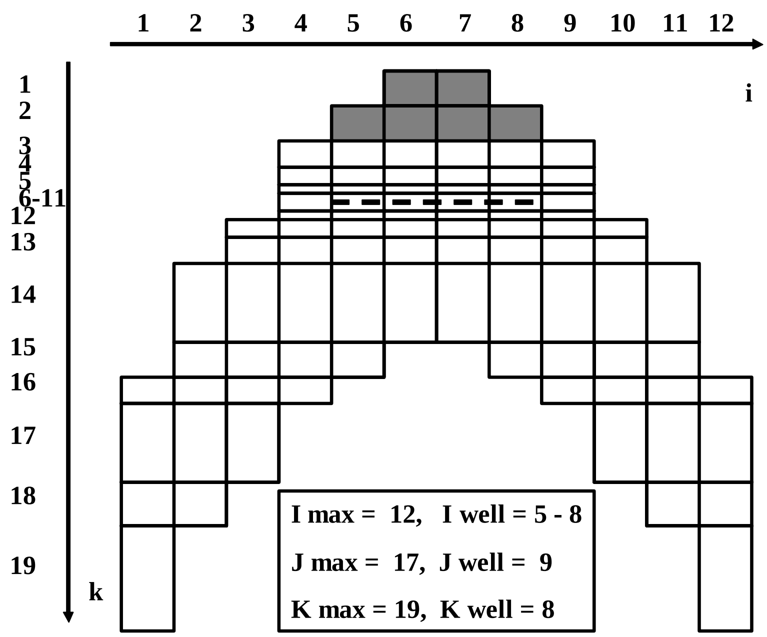

Figure 4- 30. Grid structure for a straight horizontal well in a 220-ft thick anticline structure.

Chapter 5
RESULTS AND DISCUSSIONS

In this chapter, several cases are simulated using the optimum well representation, grid system and time steps found in Chapter 4 for curved horizontal wells in slab reservoirs and straight horizontal wells in anticlines under single- and two-phase flow conditions. Two sections are presented to discuss the results of these cases. The results for straight and undulated wells in horizontal slab structures are discussed in the first section. Single-phase results are used to verify the numerical simulator with the analytical models. In the second section, results for straight wells in anticline structures are shown. The discussion of two-phase pressure buildup responses for straight wells in anticlines and slab reservoirs are also presented in the second section.

The constant properties used to simulate various cases discussed in this chapter have been summarized in Table 4-1 in Chapter 4. In addition, the reservoir properties and flow rate for a straight, infinite-conductivity horizontal well in a 220-ft thick formation (anticline or slab reservoir) have been shown in Table 4-2. In this chapter, we also consider straight and undulated, infinite-conductivity horizontal wells in an 81-ft thick slab reservoir. Table 5-1 presents the relevant reservoir properties and flow rates for these cases.

Table 5- 1. Reservoir and well properties for the infinite-conductivity horizontal wells in an 81-ft thick slab structure.

Permeability in x-direction, k_x, md	20
Permeability in y-direction, k_y, md	20
Permeability in z-direction, k_z, md	5
Formation thickness (single-phase), h, ft	81
Formation thickness (gas cap), h, ft	81
Formation size in the x-direction, x_e, ft	4000
Formation size in the y-direction, y_e, ft	4000
Horizontal well length, L, ft	1000
Total flow rate, q, scf/d	2000

In addition, Table 5-2 presents the reservoir properties and flow rate for straight and curved wells in horizontal slab structures (81 ft thickness) that yield small reservoir drawdown and relatively high wellbore pressure drop to highlight the effect of frictional pressure drop (finite-conductivity effect). The grid systems used to obtain these results have been discussed in Sections 4.2.1 and 4.2.2 in Chapter 4.

Table 5- 2. Reservoir and well properties for the finite-conductivity horizontal wells in an 81-ft thick slab structure.

Permeability in x-direction, k_x, md	1000
Permeability in y-direction, k_y, md	1000
Permeability in z-direction, k_z, md	800
Formation thickness (single-phase), h, ft	81
Formation thickness (gas cap), h, ft	81
Formation size in the x-direction, x_e, ft	4000
Formation size in the y-direction, y_e, ft	4000
Horizontal well length, L, ft	1000
Total flow rate, q, scf/d	150000

In the following sections, the simulation results are shown in terms of log-log plots of pressure and pressure derivative. The results are also compared with analytical solutions.

5.1 Well Undulation Effects in Horizontal Slab Structures

In this section, straight and curved horizontal wells in slab structures are considered to study the undulation effects on pressure-transient behavior. The amplitude of the undulations considered in this work is always less than 12 percent of the formation thickness (In reality, horizontal wells usually undulate as a result of drilling practices). However, the amplitude of the curvature is normally negligible compared to the thickness of the producing formation. Therefore, the results obtained here should be applicable to the cases where the well curvature is a result of the normal drilling practices.

First consider a straight horizontal well in a slab structure to verify the numerical model and identify the conventional characteristics of pressure and derivative responses.

Straight wells under single-phase flow condition:

This case is presented to verify the numerical model for conventional horizontal wells. We consider single-phase flow to a straight horizontal well in an 81-ft slab structure. The well is represented as shown in Fig. 4-17. The comparison of the pressure and derivative responses from numerical and analytical models (Eq. 2-11) for the infinite-conductivity case (Table 5-1) is shown in Fig. 5-1. The early-time difference between the analytical and numerical results in Fig. 5-1 may be attributed to the fact that the numerical solution assumes a finite wellbore radius and the analytical solution is for a line source well.

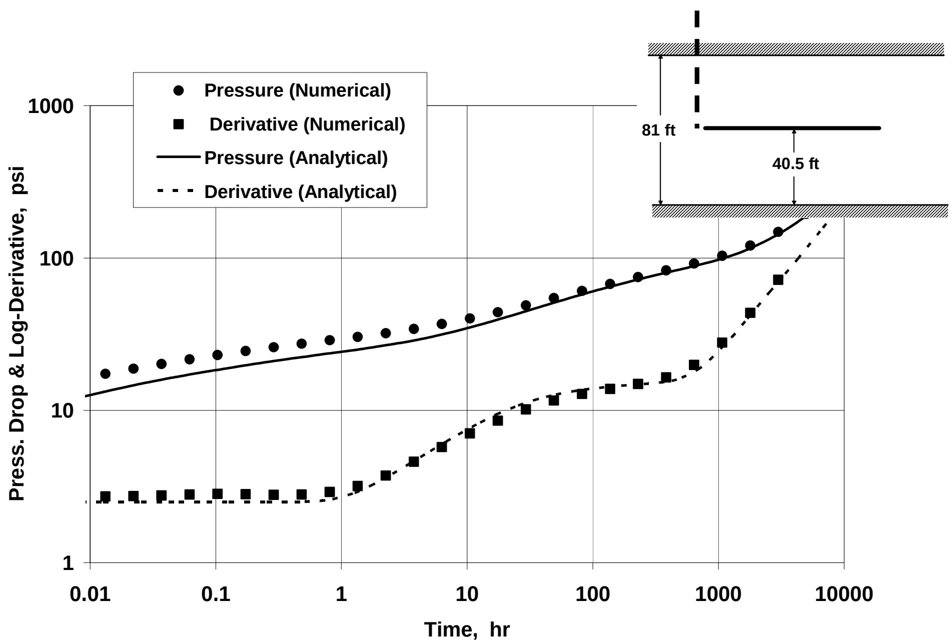

Figure 5- 1. Verification of the numerical results for a straight, infinite-conductivity horizontal well in an 81-ft thick slab structure; single-phase.

Figure 5-2 presents the comparisons of the pressure and derivative responses from numerical and analytical models for the finite-conductivity case (Table 5-2). The late-time difference between the analytical and numerical results in Fig. 5-2 is because of the fact that the analytical model (Eq. 2-21) is for an infinite slab reservoir.

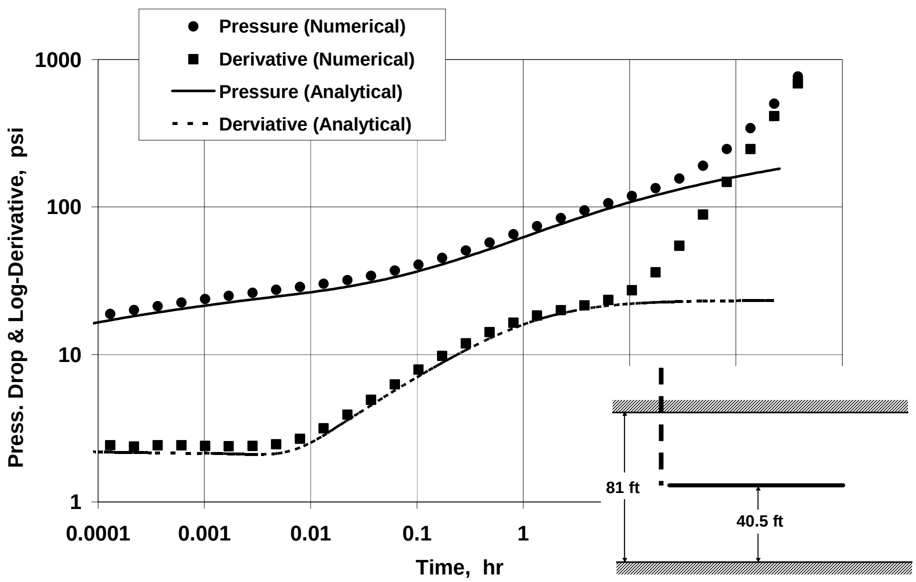

Figure 5- 2. Verification of the numerical results for a straight, finite-conductivity horizontal well in an 81 ft slab thick structure; single-phase.

The results in Figs. 5-2 and 5-3 verify our numerical model, grid system, and time-step selection. Therefore, this model is used for the cases to investigate the undulation effects.

<u>Undulated wells under single-phase flow condition</u>**:**

To study the effects of horizontal well undulations in slab structures, a vertical window of curvature of 10 ft in an 81-ft-thick reservoir is chosen. (The schematics of the cases considered are given by Figs. 4-19, 4-21, 4-23, 4-25 and 4-27, and also by the insets of the figures presented in this section). The pressure and derivative responses are shown in Figs. 5-3 – 5-9 below.

The results for concave downward wells without and with finite-conductivity effects are presented in Figs. 5-3 and 5-4, respectively. The results indicate that the concave downward well displays similar pressure behavior to the straight wells under single-phase flow conditions.

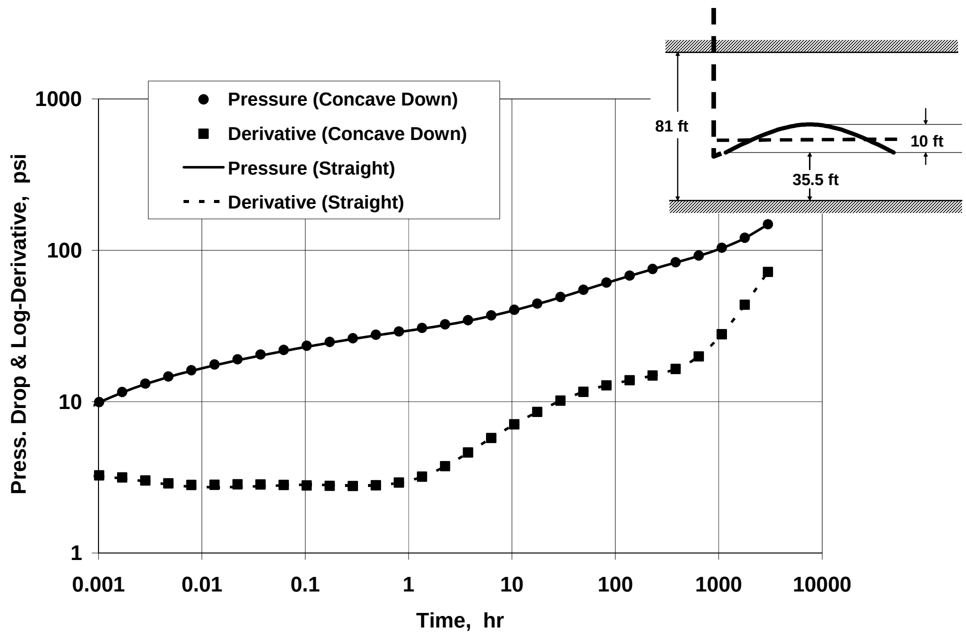

Figure 5- 3. Pressure-transient responses for straight and concave downward infinite-conductivity wells in an 81-ft thick slab structure; single-phase.

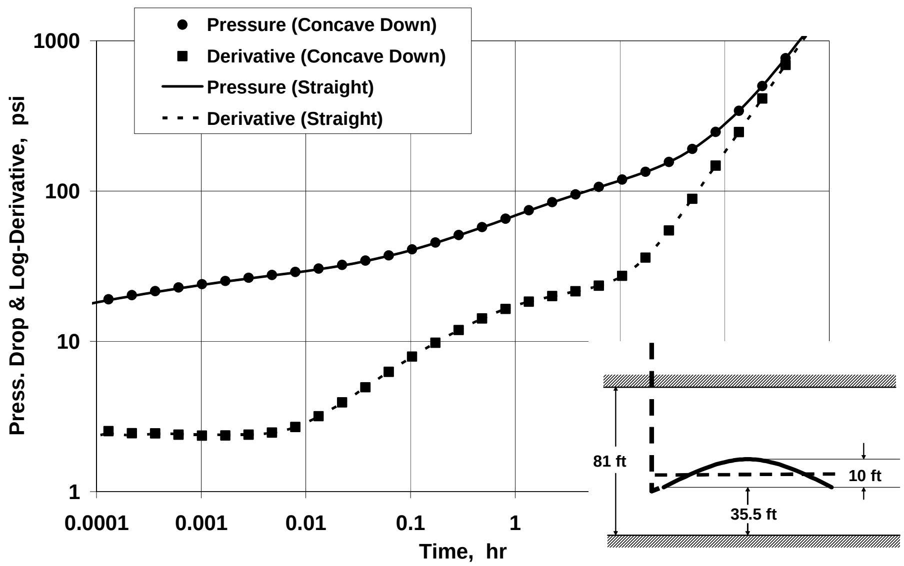

Figure 5- 4. Pressure-transient responses for straight and concave downward finite-conductivity wells in an 81-ft thick slab structure; single phase.

Figs. 5-5 and 5-6 are the counterparts of Figs. 5-3 and 5-4, respectively, for a well that is concave up. The results shown in Figs. 5-5 and 5-6 agree with results of the concave downward well and show no difference on the pressure-transient responses as compared with the straight well case.

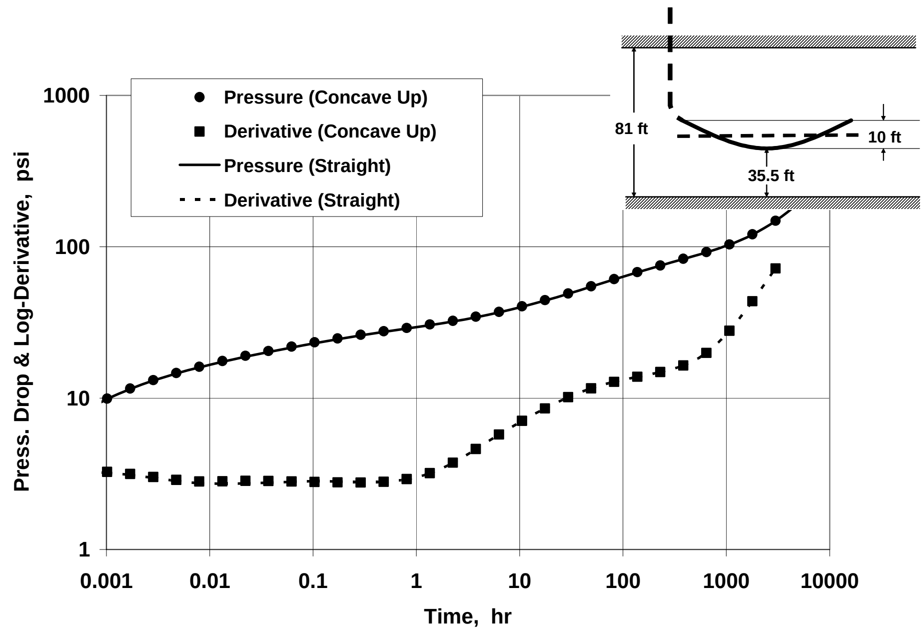

Figure 5- 5. Pressure-transient responses for straight and concave upward infinite-conductivity well in an 81-ft thick slab structure; single phase.

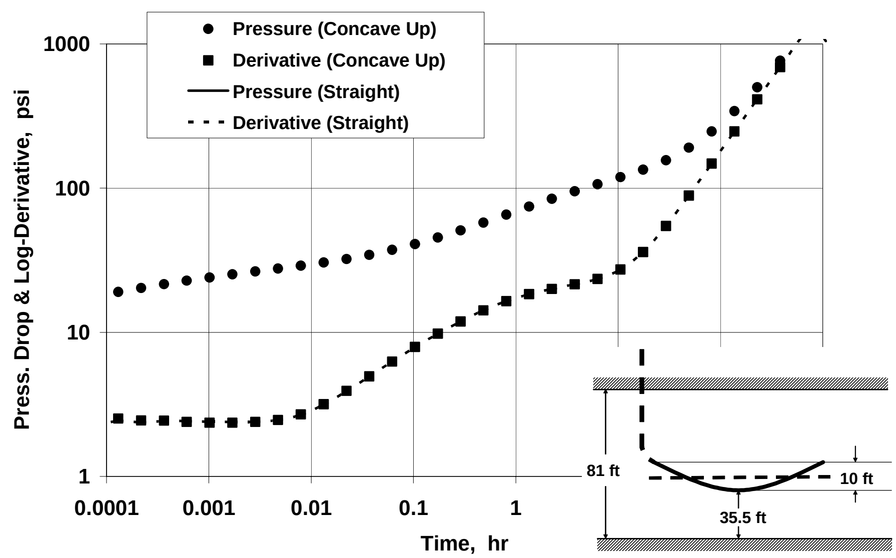

Figure 5- 6. Pressure-transient responses for straight and concave upward finite-conductivity wells in an 81-ft thick slab structure; single-phase.

The flux distributions along the straight and curved horizontal wells for infinite- and finite-conductivity wells are shown in Figs. 5-7 and 5-8, respectively. The curved wells show similar flux distribution to that of the straight well for both infinite- and finite-conductivity cases. This indicates that the gravitational and frictional forces balance each other in the upward and downward inclined sections of the well. Figs. 5-7 and 5-8 show that the flux distribution is symmetric for infinite-conductivity wells because the pressure drop along the wellbore is negligible compare to the reservoir drawdown. The high frictional pressure drop in the wellbore causes asymmetric flux distribution for the finite-conductivity wells. Therefore, the concave downward and upward trajectory of the well does not affect the pressure transient response. The conclusion is valid under single-phase flow conditions for both infinite- and finite-conductivity wells. Based on these results, only infinite-conductivity wells are considered in the rest of this study.

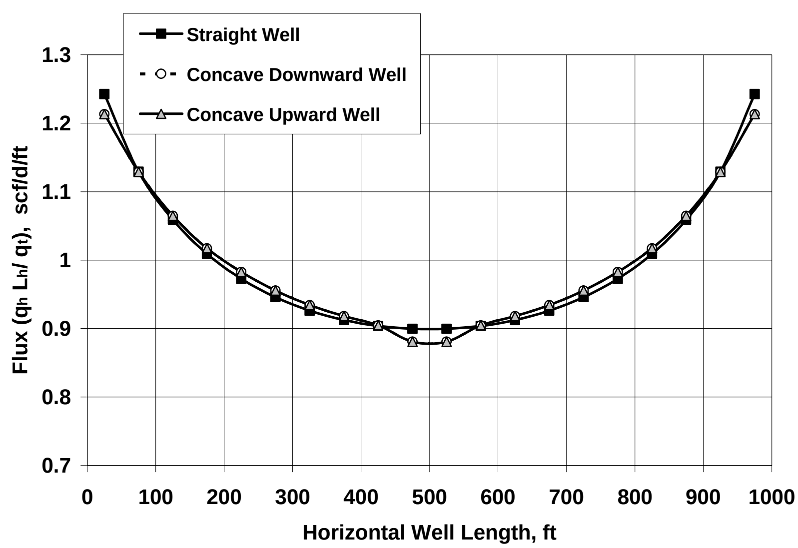

Figure 5- 7. Flux distribution for straight, concave upward, and concave downward infinite-conductivity wells in an 81-ft thick slab structure; single-phase.

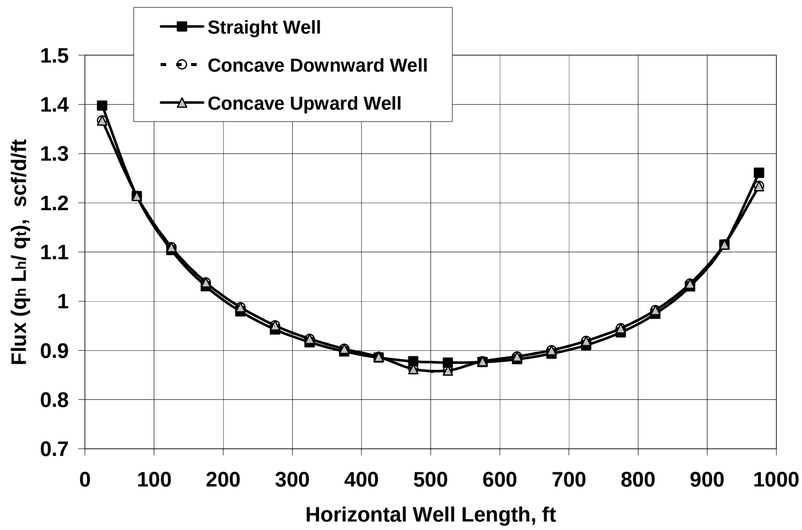

Figure 5- 8. Flux distribution for straight, concave upward, and concave downward finite-conductivity wells in an 81-ft thick slab structure; single-phase.

In addition to the study of the curved wells (concave upward and downward), three sinusoidal undulations of the wells were considered: 2 ½ cycles (Fig. 4-23), 3 cycles (Fig. 4-25), and 4 ½ cycles (Fig. 4-27).

Fig. 5-9 presents the results for an undulated well with 2 ½ sinusoidal cycles. It shows a very good agreement with straight horizontal well case.

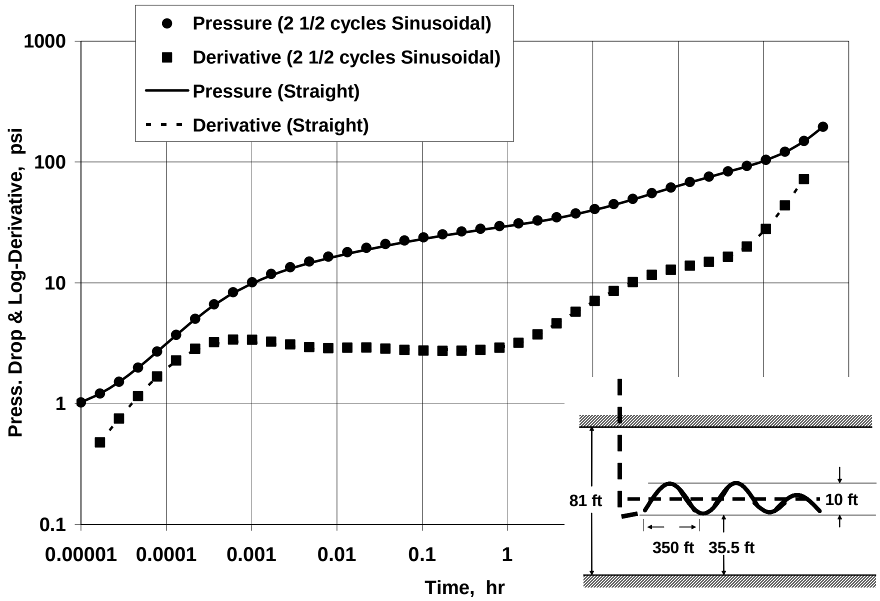

Figure 5- 9. Pressure-transient responses for straight and 2 ½ – cycle sinusoidal undulated wells in an 81 ft slab structure; single-phase, infinite-conductivity.

Figure 5-10 shows similar result as compared with the curved well (Figs. 5-3 and 5-5). Larger number of sinusoidal cycles (3 cycles) were considered as shown in the inset of Fig. 5-10. In Fig. 5-10, no pressure difference is shown as compared with the straight well.

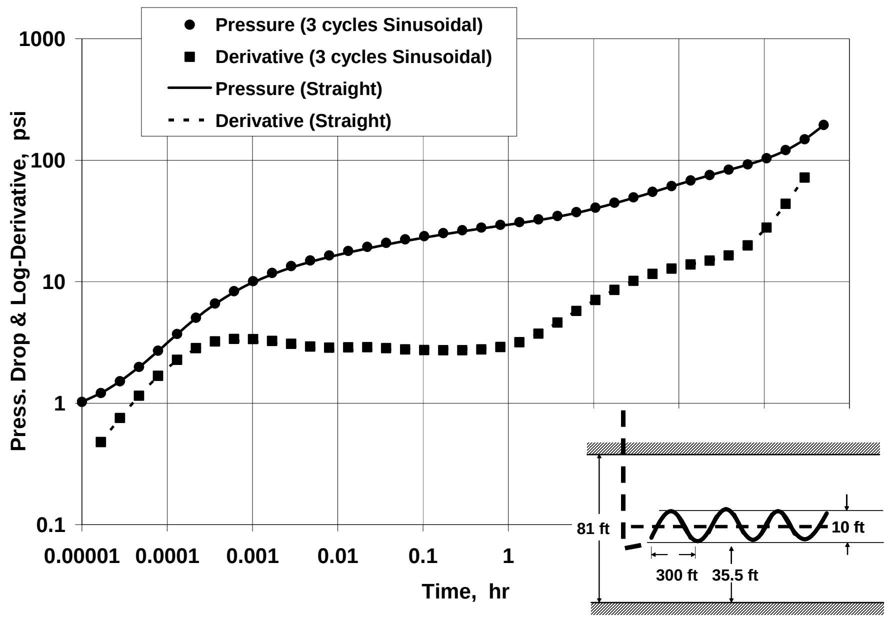

Figure 5- 10. Pressure-transient responses for straight and 3 – cycle sinusoidal undulated wells in an 81 ft slab structure; single-phase, infinite-conductivity.

The comparison of the results for 4 ½ – cycle undulated well and the straight well are shown in Fig. 5-11. Again, the agreement with the straight horizontal well case is very good.

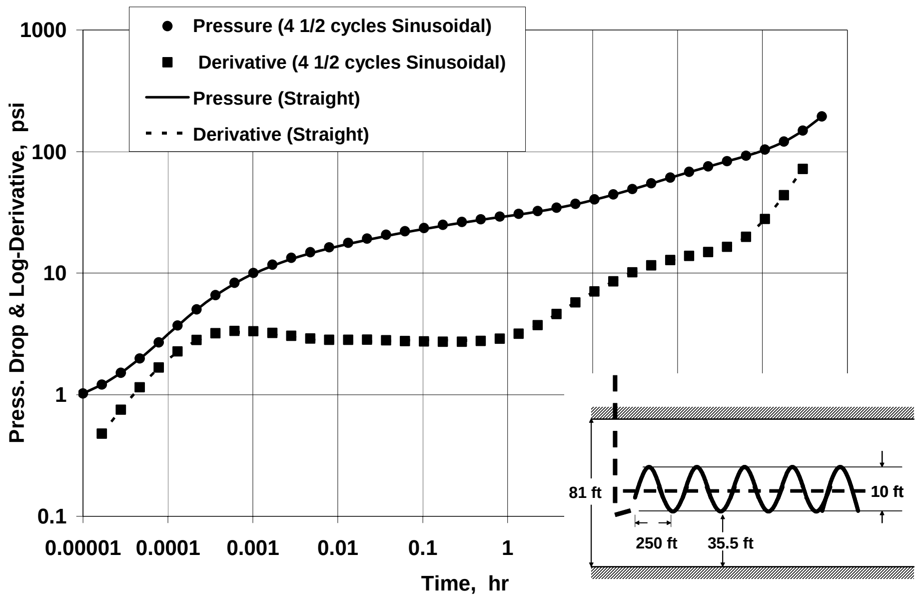

Figure 5- 11. Pressure-transient responses for straight and 4 ½ – cycle sinusoidal undulated wells in an 81-ft thick slab structure; single-phase, infinite-conductivity.

The good match between the results for the straight and curved wells shown in Figs. 5-3 – 5-9 agrees with the observations of Goktas and Ertekin.[16] Goktas and Ertekin approximated the effective length for the curved and undulated wells by the straight distance between the tips of the well (Fig. 5-12). Considering three different undulation schemes (Fig. 5-12), they found that the effect of the undulations would be negligible except when the amplitude of the undulations approach the formation thickness, and only for early and intermediate times (Figs. 5-13, 5-14 and 5-15). In this study, however, all the undulated wells were modeled in the center of an 81 ft thick slab structure with fixed amplitude undulation of 10 ft (The ratio of the amplitude of the undulations to formation thickness is less than 12 %).

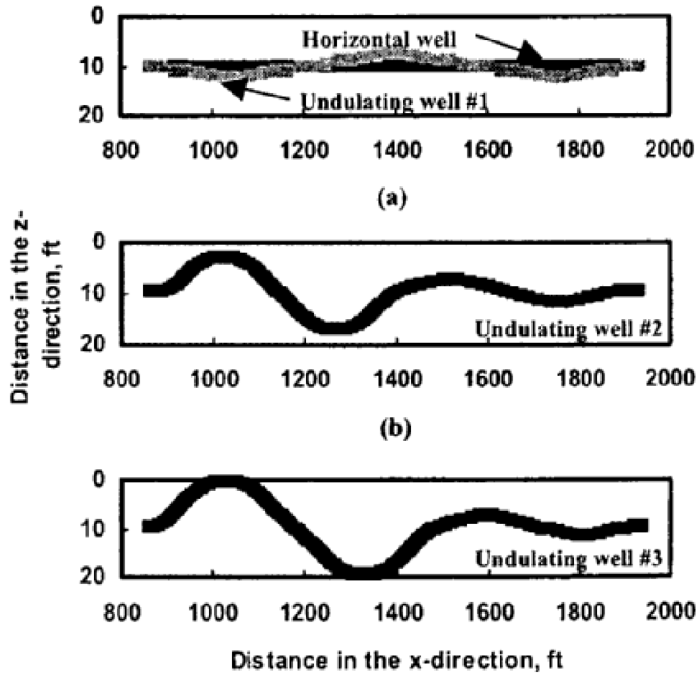

Figure 5- 12. Schematic representation of three undulating wells considered.[16]

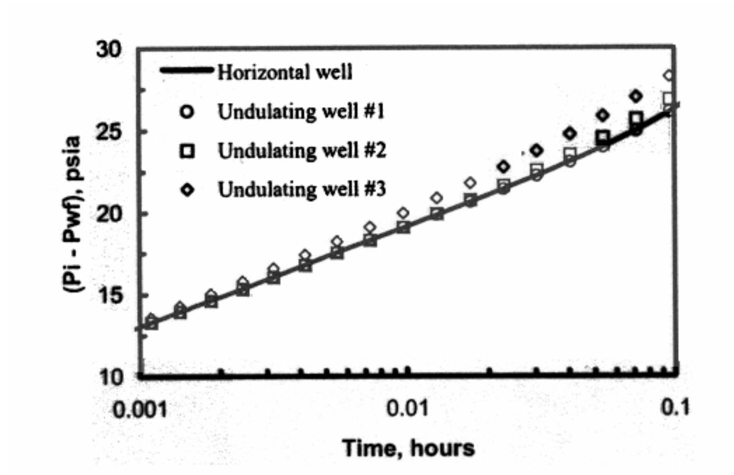

Figure 5- 13. Early-time radial flow.[16]

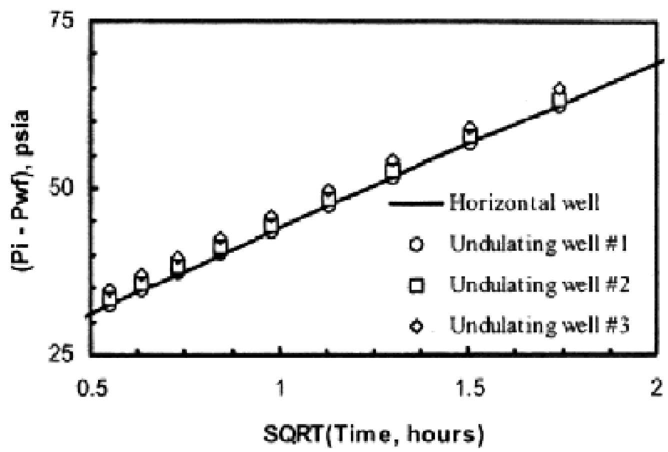

Figure 5- 14. Early-time linear flow.[16]

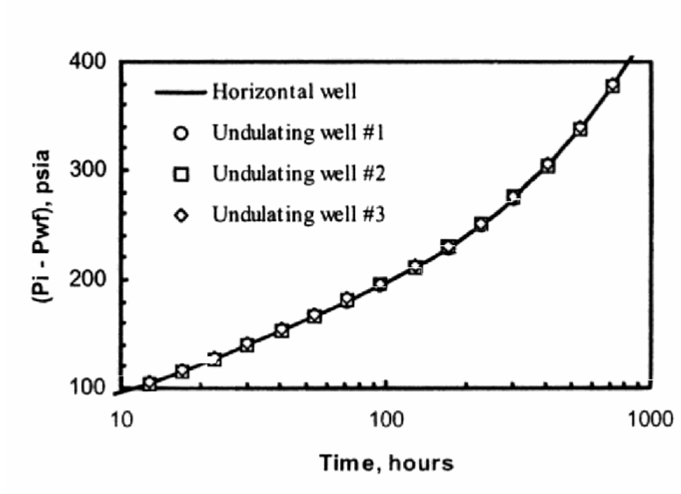

Figure 5- 15. Late pseudo-radial flow.[16]

In another study, Azar-Nejad et al.[15] have found that undulations may affect the pressure-transient characteristics of horizontal wells significantly especially in anisotropic formations. The comparison of the dimensionless pressure of a ¼ – circle (Fig.5-16) and a straight horizontal well with the same producing length in a rectilinear, anisotropic reservoir (higher horizontal permeability than vertical permeability) is shown in Fig. 5-17. It can be seen that the pressure of the curvilinear well is lower than that of the straight horizontal well. This result is different from our conclusions and the results of Goktas and Ertekin.[16] The choice of the effective well length may be the cause of the difference. The total drilled length is used as the effective length in Ref.15 as shown in Fig. 5-16. On the other hand, both curvilinear well and straight horizontal well in isotropic reservoir show almost identical pressure responses as shown in Fig. 5-18.

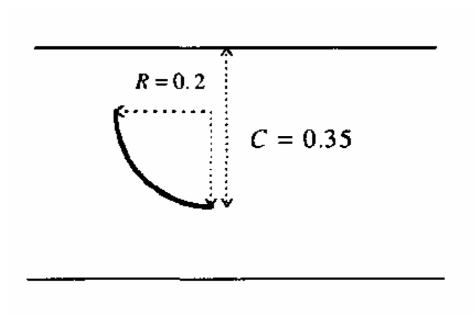

Figure 5- 16. Schematic of a curvilinear well (1/4 of a circle with radius 0.2) in a rectilinear reservoir.[15]

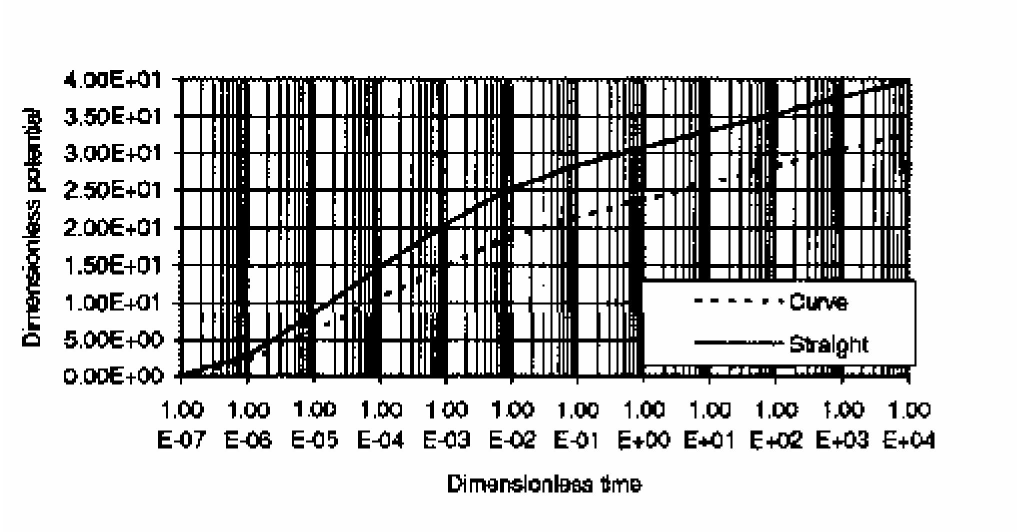

Figure 5- 17. Comparison of dimensionless pressures of a ¼ – circle and a straight horizontal well with the same producing length; anisotropic reservoir[15].

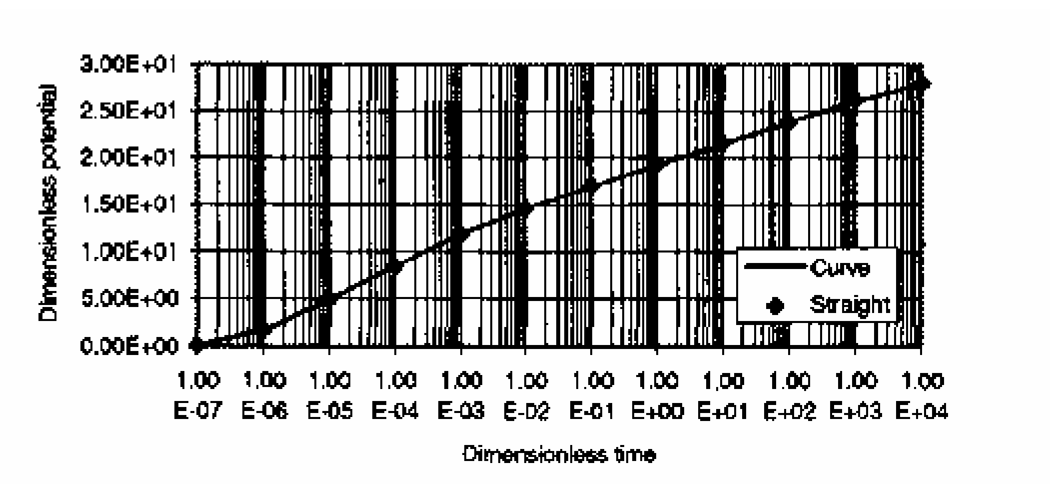

Figure 5- 18. Comparison of dimensionless pressures of a ¼ – circle and a straight horizontal well with the same producing length; isotropic reservoir[15].

Based on the results of this study, it is concluded that the pressure-transient responses of undulated wells may be simulated and analyzed by assuming a straight well in a horizontal slab structure (conventional horizontal well models) provided that the straight distance between the tips of the well is used as the effective well length. This conclusion is also valid for the finite-conductivity cases with considerable wellbore pressure drop. However, wells with high curvature or wide undulations that are too close to the top and bottom boundaries are excluded.

The cases of non-uniform skin distribution with selectively open segments of high and low influx along the well may severely affect the pressure distributions in and around the well. Therefore, the above conclusion may not be applicable for these cases. In addition, the curved wells considered in this study have symmetry with respect to the mid-point of the well. Therefore, the effects of gravity and friction in the two halves of the well may be cancelled. Significant differences for asymmetric wells, however, are not expected as indicated by the results of sinusoidal undulated wells (Figs. 5-9 – 5-11).

Straight wells under gas-cap effect:

The cases discussed above were only limited to single-phase flow. This section will address the effect of a gas cap on pressure-transient responses. Because most pressure-transient analysis tools and techniques ignore the existence of a gas cap, it is important to investigate the consequences of this assumption. However, there are exist different options to replace a system with a gas cap by an approximate single-phase system. In this study, two different cases were considered. The first case is for a structure with a gas cap of total thickness equal to the formation thickness for the single-phase flow model (Fig. 5-19). In second case, the original oil zone thickness is assumed to be the same as the formation thickness for the single-phase flow model (Fig. 5-21). Fig. 5-19 shows a gas cap of 23-ft thickness located at the top of an 81-ft thick slab structure and 17.5 ft away from the well.

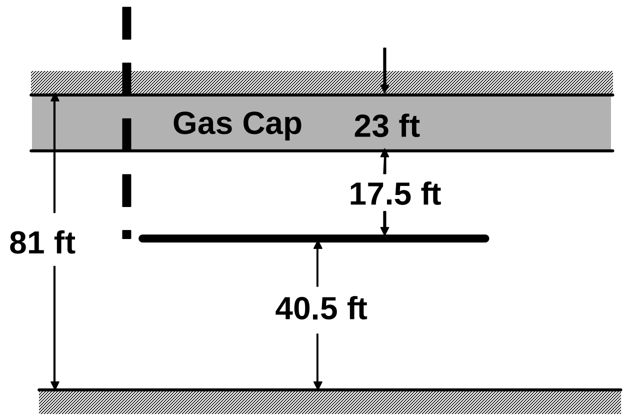

Figure 5- 19. Straight horizontal well in an 81-ft thick slab structure; gas cap.

Models with and without gas cap are shown in Figs. 5-19 and 4-17, respectively. The comparison of the drawdown responses of straight horizontal wells with and without gas cap is seen in Fig. 5-20. Gas encroachment toward the well affects the pressure and derivative responses significantly as observed by Fleming et al.[17, 18] It is shown in Fig. 5-20 that the gas effect starts at the end of early-time radial flow period and changes the flow characteristics of intermediate- and late times compared to single-phase flow. The physical parameters of gas coning toward a horizontal well governs the deviation from the conventional horizontal well behavior (single-phase flow toward a straight horizontal well in a slab structure).[36-39]

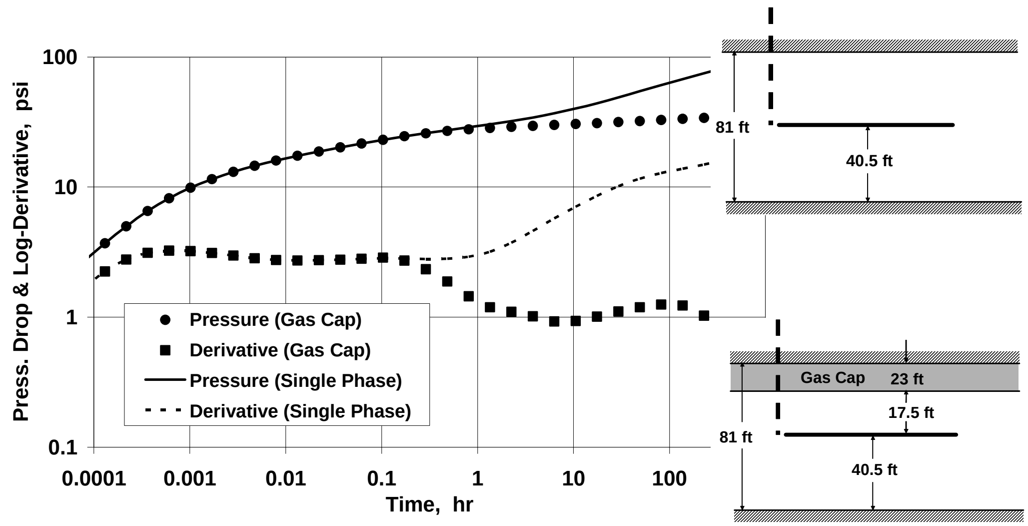

Figure 5- 20. Pressure-transient responses for a straight horizontal well in an 81-ft thick slab structure; single-phase and gas cap.

The model for the second case of equal gas cap volume located 23-ft away from the well in 104-ft thick slab structure was run as shown in Fig. 5-21.

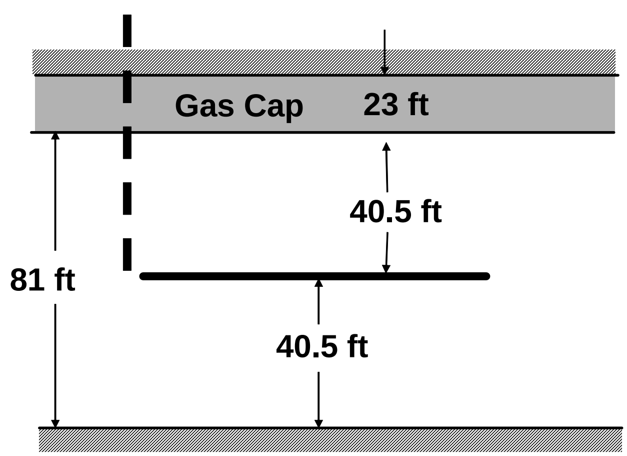

Figure 5- 21. Straight horizontal well in an 81-ft thick slab structure; gas cap.

For this case, the gas effect starts later (t = 1hr) than the model with a gas cap located 23 ft closer to the well as shown in Fig. 5-22. This is because of the farther distance traveled by the pressure response in Fig. 5-21 to reach the gas-oil interface. As expected, this indicates that the start of the distorted flow characteristics from single-phase flow is governed by the location of the gas cap from the well.

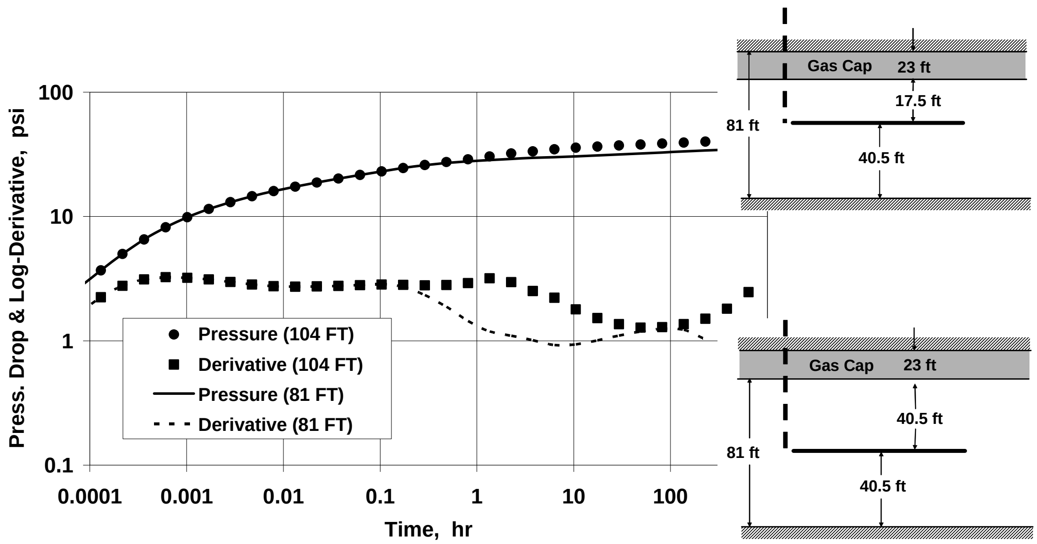

Figure 5- 22. Pressure-transient responses for a straight horizontal well in an 81 and 104 ft slab structure; gas-cap.

The results presented in Figs. 5-20 and 5-22 indicate that the analysts may be perplexed if they fail to recognize the effects of gas coning during the interpretation of horizontal well tests. In addition, obtaining the directional permeabilities by using the conventional models would be impossible with the loss of the characteristics of the intermediate- and late-time flow regimes.[14] Therefore, detailed numerical models, such as the one developed in this study, are crucial to be able to analyze horizontal well tests under the influence of gas cap.

<u>Curved wells under gas-cap flow:</u>

The next issue is to address the effect of well curvature in the presence of a gas cap. Figure 5-23 shows the concave-downward well model in the presence of a gas cap.

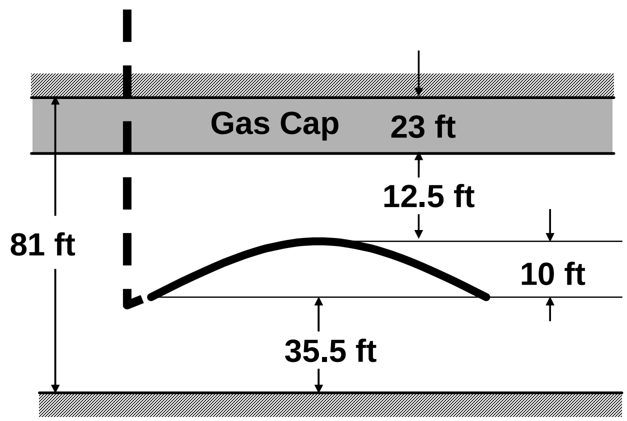

Figure 5- 23. Concave downward well in an 81-ft thick slab structure; gas cap.

The responses of concave-downward and straight horizontal wells in the presence of a gas cap are presented in Fig. 5-24. Figure 5-24 shows the agreement between the two-phase pressure-transient responses of concave downward and straight wells. This is akin to the result observed in Fig. 5-4 under single-phase condition.

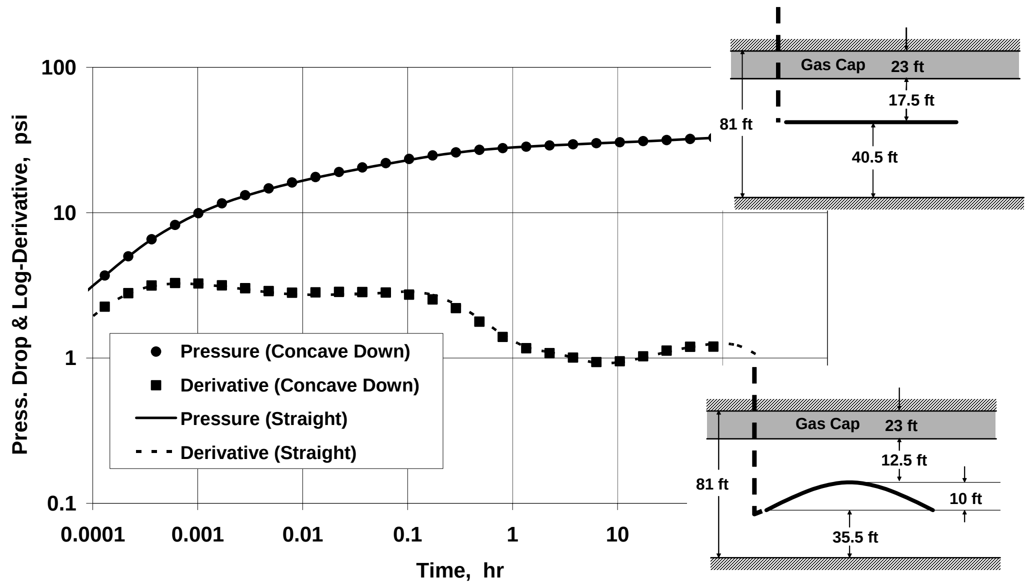

Figure 5- 24. Pressure-transient responses for straight and concave downward wells in an 81-ft thick slab structure; gas cap.

In addition to a concave downward well, a concave-upward well in the presence of a gas cap (Fig. 5-25) was also considered. Figure 5-26 compares the responses of concave-upward well (Fig. 5-25) with that of a straight horizontal well (Fig. 5-19) in the presence of a gas cap.

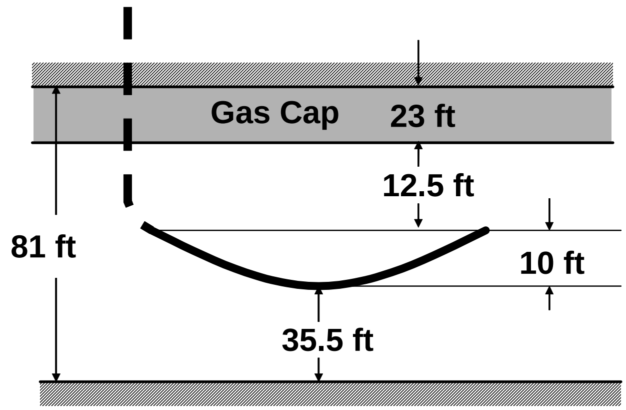

Figure 5- 25. Concave upward well in an 81-ft thick slab structure; gas cap.

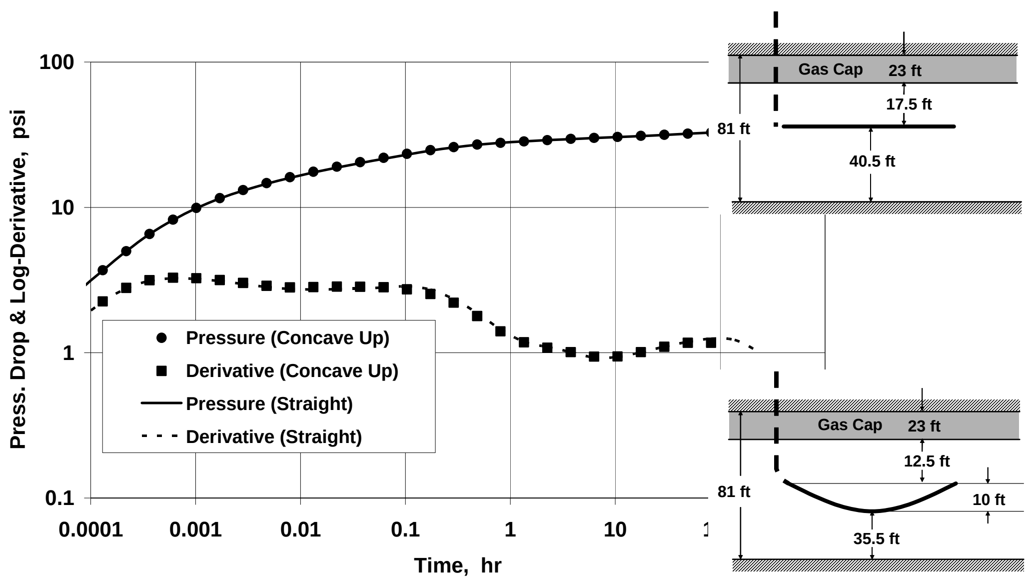

Figure 5- 26. Pressure-transient responses for straight and concave downward wells in an 81-ft thick slab structure; gas cap.

Figure 5-26 indicates, again, that the curvature of the well does not influence the pressure and derivative responses. This is because the straight distance between the tips of the curved wells was used as the effective horizontal well length in the simulation of the straight well case. Based on this result, the sinusoidal undulated wells in the presence of a gas cap were not investigated. On the other hand, the effect of the gas cap should be taken into account in the interpretation of the pressure and derivative responses as discussed in Fig. 5-20.

5.2 Structure Effects

In this section, the effect of the curvature of the pay zone will be discussed by comparing the results for straight horizontal wells in anticlines and horizontal slab reservoirs.

Straight wells in horizontal slab reservoirs and anticlines under single-phase flow condition:

First, the effect of the curvature of the pay zone is examined under single-phase flow conditions. The pressure-transient responses of straight horizontal wells in anticlines (Fig. 4-29) and slab reservoirs (Fig. 4-1) are presented in Fig 5-27.

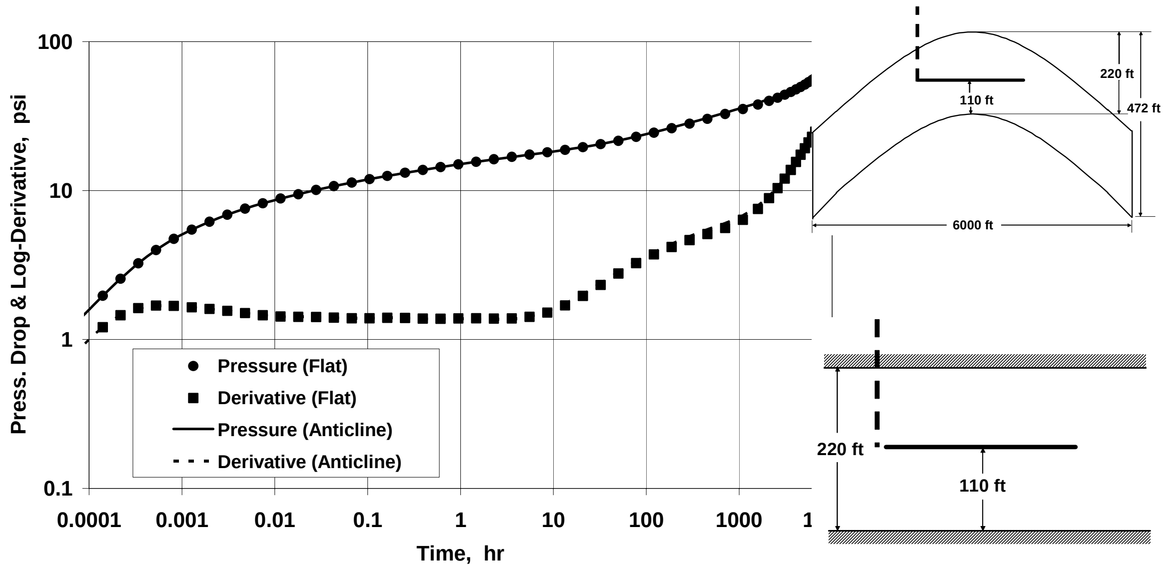

Figure 5- 27. Pressure-transient responses for a straight horizontal well in a 220-ft thick slab reservoir and anticline; single-phase.

Figure 5-27 shows no discernable influence of the curvature of the pay zone on the pressure-transient responses. Therefore, the pressure-transient responses of horizontal wells in anticlines and domes can be analyzed by using the conventional horizontal well models (straight well in horizontal slab structure) under single-phase flow conditions. This conclusion, however, is found to be invalid if a gas cap exists in the system as shown below.

<u>Straight wells in anticline structure under gas-cap effect:</u>

Based on the results found for horizontal slab structures under two-phase flow, some influence of the gas cap on the pressure-transient responses of horizontal wells in anticlines is expected. Figure 5-28 shows the straight horizontal well model in anticlines with gas cap.

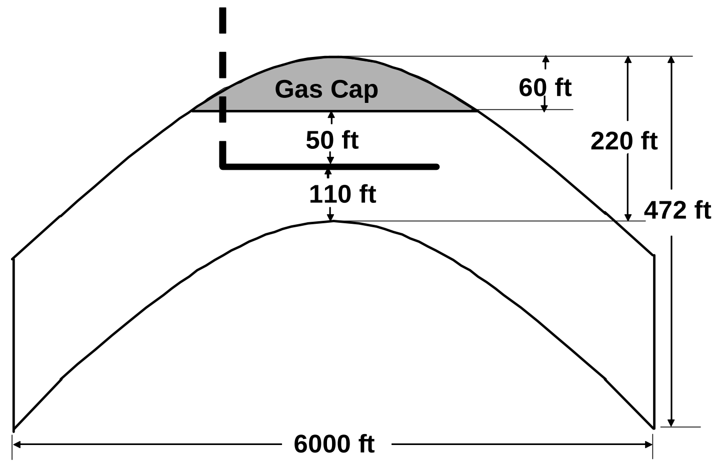

Figure 5- 28. Straight horizontal well in a 220-ft thick anticline structure; gas cap.

Figure 5-29 compares the pressure and derivative responses of straight horizontal wells in anticlines with and without gas cap (Figs. 5-28 and 4-29, respectively). It can be seen in the figure, as expected, there is significant difference in the pressure and derivative characteristics when the gas cone advances toward the well. This conclusion is the same as that for straight wells in slab structure (Fig. 5-20).

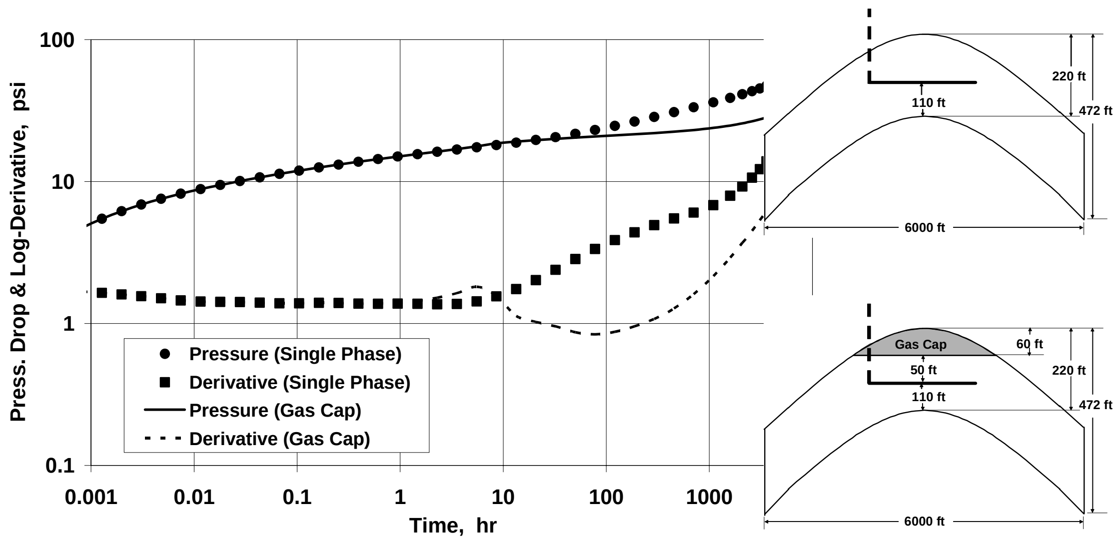

Figure 5- 29. Pressure-transient responses for a straight horizontal well in a 220-ft thick anticline structure; single- and gas cap.

<u>Straight wells in horizontal slab reservoirs and anticlines under gas-cap effect:</u>

In this section, the results for a straight horizontal well in anticlines and slab reservoirs with gas cap are discussed. Equivalent volume of gas cap was applied in both anticline structure and horizontal slab reservoir. Two different methods were used for the slab reservoir model to create the same amount of gas volume as in anticline structure: adjusting the gas cap thickness or the gas cap porosity. Figure 5-30 shows a straight well in a slab structure in the presence of the adjusted gas cap thickness of 15.06 ft (60.25 ft for single-phase).

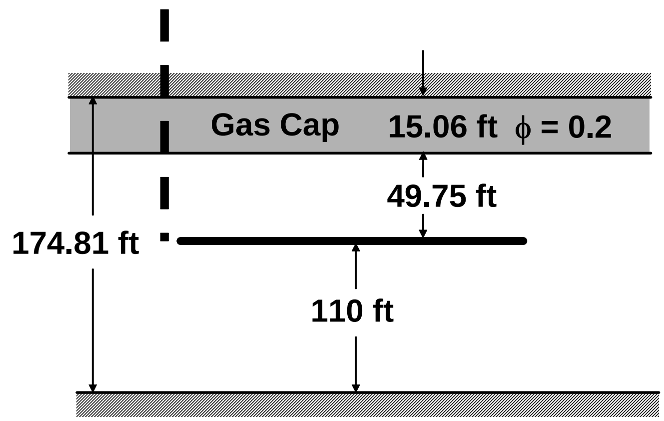

Figure 5- 30. Straight horizontal well in a 174.81-ft thick slab structure; gas cap.

Figure 5-31 shows an interesting observation for the case where the pressure and derivative responses of horizontal wells in anticlines (Fig. 5-28) and slab reservoirs (Fig. 5-30) are compared in the presence of a gas cap. It can be seen that the derivative responses show some difference after the gas breakthrough. Therefore, the approximation of an anticline by an equivalent horizontal slab with an equivalent gas cap of adjusted thickness may not be valid for the analysis of horizontal-well tests.

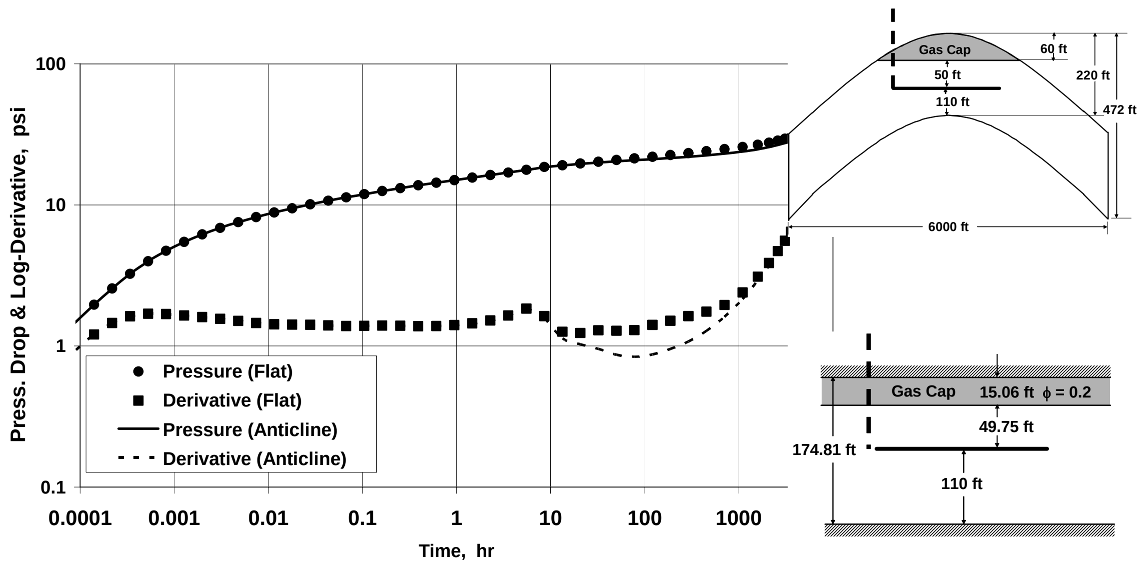

Figure 5- 31. Pressure-transient responses for straight horizontal wells in a 174.81-ft thick slab reservoir and a 220-ft thick anticline; gas cap.

Based on this result, another method was used to calculate the gas volume for the horizontal slab structure by adjusting the porosity of the gas cap to 0.05 (0.2 for single-phase) as shown in Fig. 5-32.

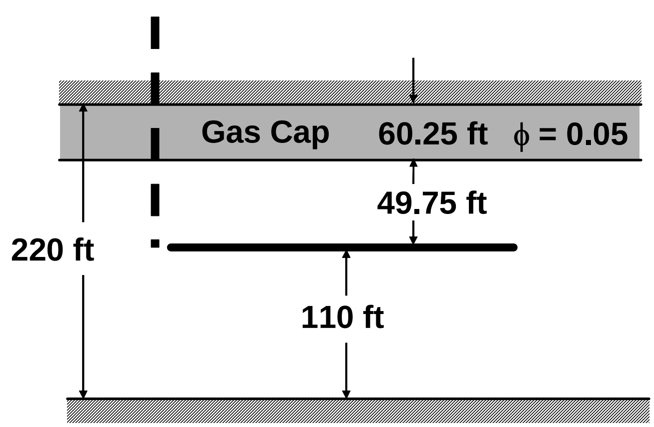

Figure 5- 32. Straight horizontal well in a 220-ft thick slab structure; gas cap.

Figure 5-33 shows comparable pressure pressure-transient and derivative responses for the straight well in anticline and slab reservoirs in the presence of a gas cap. The method used to calculate the equivalent gas volume for horizontal slab reservoir by adjusting the gas cap porosity shown in Fig. 5-33 yields smaller difference on the derivative responses after the gas breakthrough as compared with the method of adjusting the gas cap thickness.

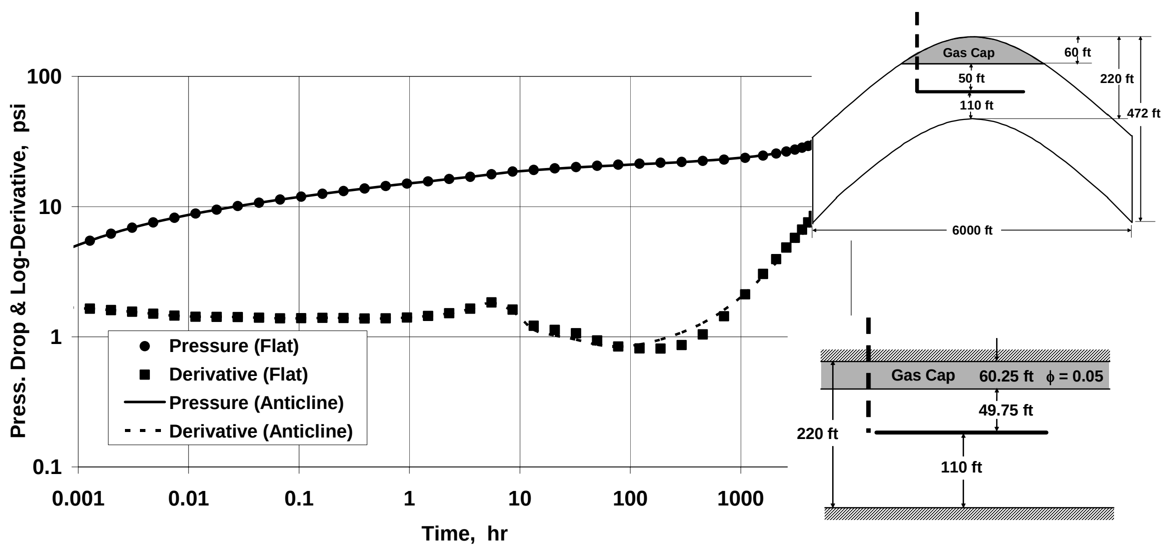

Figure 5- 33. Pressure-transient responses for straight horizontal wells in a 220-ft thick slab reservoir and anticline; gas cap.

<u>Pressure Buildup:</u>

The drawdown responses discussed so far indicate that the pressure responses are influenced significantly by the encroachment of a gas cap. Then, the buildup responses following a drawdown should be influenced by the gas cap. In this section, the buildup responses are examined for both straight wells in anticline and slab structures.

Based on the results obtained so far, the buildup responses should follow the conventional horizontal well models for the cases where the well or pay-zone curvature has no effect on the pressure-transient characteristics of horizontal wells. Therefore, three cases including a gas cap were considered for the buildup responses.

The case for a straight well in an anticline (Fig. 5-28) is considered and compared with a straight well in a horizontal slab reservoir for adjusted gas cap thickness and porosity in Figs. 5-30 and 5-32, respectively. The schematic of these models are shown in the inset of the figures below. The buildup tests follow a long producing period of 16,400 hrs (gas has brokenthrough by the time the well is shut in) at a constant rate of 2000 scf/d (the data for this case is given in Tables 4-1 and 4-2).

Figure 5-34 compares the buildup responses of straight wells in horizontal slab reservoirs (Fig.5-30) and anticlines (Fig. 5-28). It is shown in Fig. 5-34 that derivative responses for both cases display oscillations after the initial radial flow period. It is clear from the results shown in Fig. 5-34 that the derivatives of the pressure buildup responses for the horizontal slab reservoir and anticline do not follow each other when the oscillations begin. This is because of the differences during the drawdown period as displayed in Fig. 5-31.

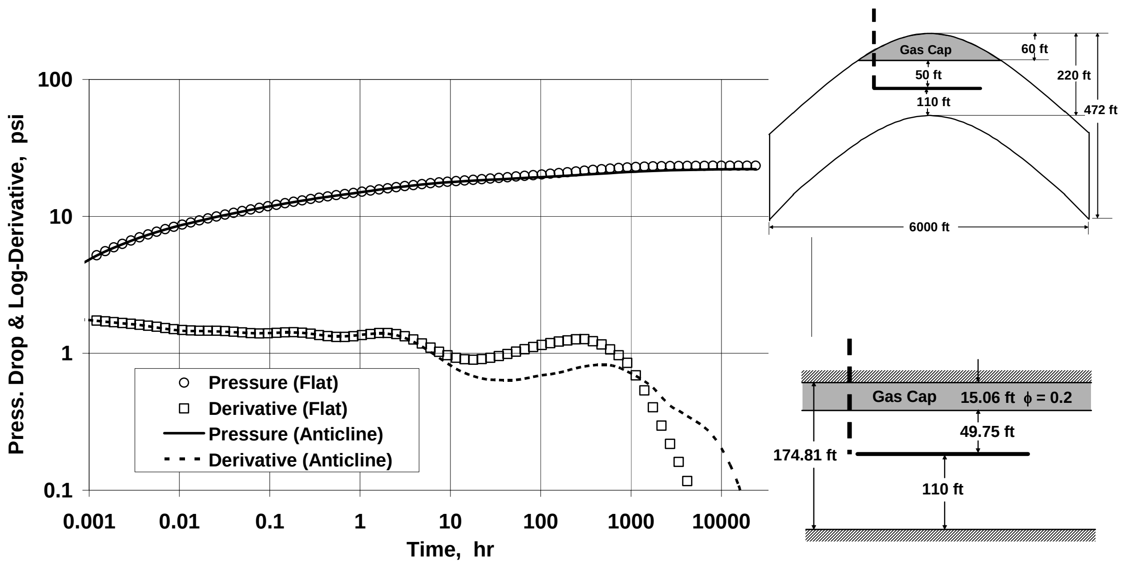

Figure 5- 34. Pressure buildup responses for straight horizontal wells in a 174.81-ft thick slab reservoir and a 220-ft thick anticline; gas cap.

The buildup responses for a straight well in a horizontal slab reservoir (Fig. 5-32) and an anticline (Fig. 5-28) show oscillations on the derivative responses after the early-radial flow regime as presented in Fig. 5-35. The small difference in the derivatives of the pressure buildup responses between horizontal slab reservoir and anticline is because of the difference during the drawdown period (Fig. 5-33).

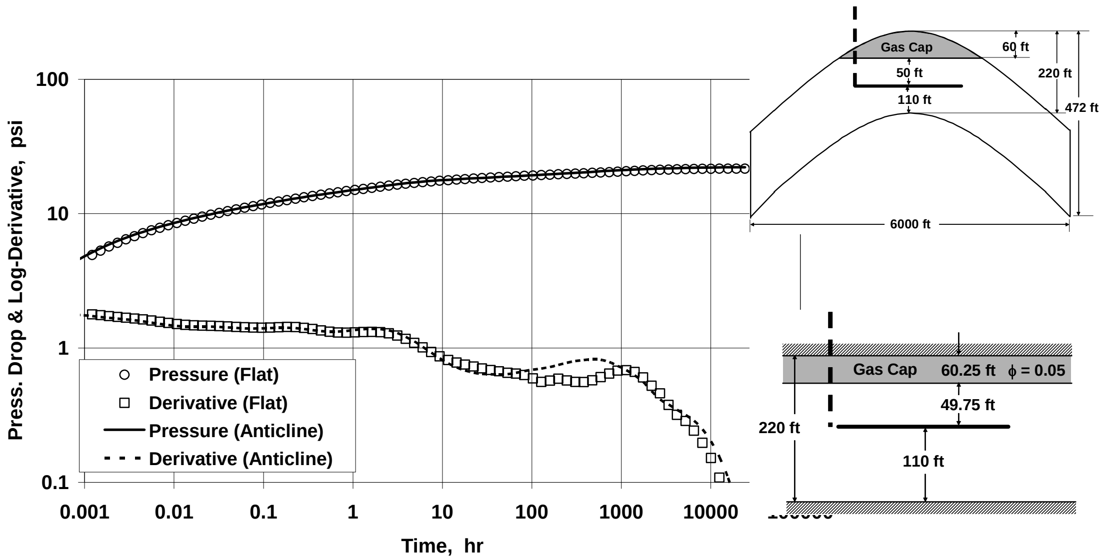

Figure 5- 35. Pressure-transient buildup responses for straight horizontal wells in a 220-ft thick slab reservoir and anticline; gas cap.

.

For completeness, the gas saturation distribution at different times during drowdawn and buildup is shown in Figs. 5-36 – 5-39. The figures indicate that gas cusps into the oil zone during production period and breaks into the well by the time the well is shut in. During the buildup, the cone recedes.

	1	2	3	4	5	6	7	8	9	10	11	12
1	0.800	0.800	0.800	0.800	0.800	0.800	0.800	0.800	0.800	0.800	0.800	0.800
2	0.000	0.000	0.000	0.000	0.000	0.000	0.000	0.000	0.000	0.000	0.000	0.000
3	0.000	0.000	0.000	0.000	0.000	0.000	0.000	0.000	0.000	0.000	0.000	0.000
4	0.000	0.000	0.000	0.000	0.000	0.000	0.000	0.000	0.000	0.000	0.000	0.000
5	0.000	0.000	0.000	0.000	0.000	0.000	0.000	0.000	0.000	0.000	0.000	0.000
6	0.000	0.000	0.000	0.000	0.000	0.000	0.000	0.000	0.000	0.000	0.000	0.000
7	0.000	0.000	0.000	0.000	0.000	0.000	0.000	0.000	0.000	0.000	0.000	0.000
8	0.000	0.000	0.000	0.000	0.000	0.000	0.000	0.000	0.000	0.000	0.000	0.000
9	0.000	0.000	0.000	0.000	0.000	0.000	0.000	0.000	0.000	0.000	0.000	0.000
10	0.000	0.000	0.000	0.000	0.000	0.000	0.000	0.000	0.000	0.000	0.000	0.000
11	0.000	0.000	0.000	0.000	0.000	0.000	0.000	0.000	0.000	0.000	0.000	0.000
12	0.000	0.000	0.000	0.000	0.000	0.000	0.000	0.000	0.000	0.000	0.000	0.000
13	0.000	0.000	0.000	0.000	0.000	0.000	0.000	0.000	0.000	0.000	0.000	0.000

Figure 5- 36. Gas saturation distribution in the vertical well plane at time of 20.8 hr (drawdown).

	1	2	3	4	5	6	7	8	9	10	11	12
1	0.798	0.798	0.797	0.797	0.796	0.796	0.796	0.796	0.797	0.797	0.798	0.798
2	0.000	0.000	0.000	0.000	0.161	0.159	0.159	0.161	0.000	0.000	0.000	0.000
3	0.000	0.000	0.000	0.000	0.000	0.000	0.000	0.000	0.000	0.000	0.000	0.000
4	0.000	0.000	0.000	0.000	0.000	0.000	0.000	0.000	0.000	0.000	0.000	0.000
5	0.000	0.000	0.000	0.000	0.000	0.000	0.000	0.000	0.000	0.000	0.000	0.000
6	0.000	0.000	0.000	0.000	0.000	0.000	0.000	0.000	0.000	0.000	0.000	0.000
7	0.000	0.000	0.000	0.000	0.000	0.000	0.000	0.000	0.000	0.000	0.000	0.000
8	0.000	0.000	0.000	0.000	0.000	0.000	0.000	0.000	0.000	0.000	0.000	0.000
9	0.000	0.000	0.000	0.000	0.000	0.000	0.000	0.000	0.000	0.000	0.000	0.000
10	0.000	0.000	0.000	0.000	0.000	0.000	0.000	0.000	0.000	0.000	0.000	0.000
11	0.000	0.000	0.000	0.000	0.000	0.000	0.000	0.000	0.000	0.000	0.000	0.000
12	0.000	0.000	0.000	0.000	0.000	0.000	0.000	0.000	0.000	0.000	0.000	0.000
13	0.000	0.000	0.000	0.000	0.000	0.000	0.000	0.000	0.000	0.000	0.000	0.000

Figure 5- 37. Gas saturation distribution in the vertical well plane at time of 5100 hr (drawdown).

	1	2	3	4	5	6	7	8	9	10	11	12
1	0.792	0.792	0.792	0.791	0.791	0.790	0.790	0.791	0.791	0.792	0.792	0.792
2	0.000	0.000	0.000	0.000	0.382	0.381	0.381	0.382	0.000	0.000	0.000	0.000
3	0.000	0.000	0.000	0.000	0.199	0.182	0.182	0.199	0.000	0.000	0.000	0.000
4	0.000	0.000	0.000	0.000	0.078	0.053	0.053	0.078	0.000	0.000	0.000	0.000
5	0.000	0.000	0.000	0.000	0.045	0.028	0.028	0.045	0.000	0.000	0.000	0.000
6	0.000	0.000	0.000	0.000	0.027	0.016	0.016	0.027	0.000	0.000	0.000	0.000
7	0.000	0.000	0.000	0.000	0.012	0.007	0.007	0.012	0.000	0.000	0.000	0.000
8	0.000	0.000	0.000	0.000	0.000	0.000	0.000	0.000	0.000	0.000	0.000	0.000
9	0.000	0.000	0.000	0.000	0.000	0.000	0.000	0.000	0.000	0.000	0.000	0.000
10	0.000	0.000	0.000	0.000	0.000	0.000	0.000	0.000	0.000	0.000	0.000	0.000
11	0.000	0.000	0.000	0.000	0.000	0.000	0.000	0.000	0.000	0.000	0.000	0.000
12	0.000	0.000	0.000	0.000	0.000	0.000	0.000	0.000	0.000	0.000	0.000	0.000
13	0.000	0.000	0.000	0.000	0.000	0.000	0.000	0.000	0.000	0.000	0.000	0.000

Figure 5- 38. Gas saturation distribution in the vertical well plane at time of 16400 hr (drawdown).

	1	2	3	4	5	6	7	8	9	10	11	12
1	0.792	0.792	0.792	0.792	0.792	0.792	0.792	0.792	0.792	0.792	0.792	0.792
2	0.000	0.000	0.000	0.000	0.389	0.388	0.388	0.389	0.000	0.000	0.000	0.000
3	0.000	0.000	0.000	0.000	0.006	0.006	0.006	0.006	0.000	0.000	0.000	0.000
4	0.000	0.000	0.000	0.000	0.003	0.003	0.003	0.003	0.000	0.000	0.000	0.000
5	0.000	0.000	0.000	0.000	0.001	0.001	0.001	0.001	0.000	0.000	0.000	0.000
6	0.000	0.000	0.000	0.000	0.001	0.001	0.001	0.001	0.000	0.000	0.000	0.000
7	0.000	0.000	0.000	0.000	0.000	0.000	0.000	0.000	0.000	0.000	0.000	0.000
8	0.000	0.000	0.000	0.000	0.000	0.000	0.000	0.000	0.000	0.000	0.000	0.000
9	0.000	0.000	0.000	0.000	0.000	0.000	0.000	0.000	0.000	0.000	0.000	0.000
10	0.000	0.000	0.000	0.000	0.000	0.000	0.000	0.000	0.000	0.000	0.000	0.000
11	0.000	0.000	0.000	0.000	0.000	0.000	0.000	0.000	0.000	0.000	0.000	0.000
12	0.000	0.000	0.000	0.000	0.000	0.000	0.000	0.000	0.000	0.000	0.000	0.000
13	0.000	0.000	0.000	0.000	0.000	0.000	0.000	0.000	0.000	0.000	0.000	0.000

Figure 5- 39. Gas saturation distribution in the vertical well plane at time of 19300 hr (buildup).

As in this study, Refs. 17 and 18 also report oscillations in the buildup derivative responses for horizontal wells in a fractured, vuggy, carbonate reservoir that contained a large gas cap. They found that the oscillations are a result of two-phase effects. Highresolution electronic gauges were used on the tested horizontal well and Fleming et al.[17, 18] constructed a numerical model to simulate the well test. The cyclic oscillations in the derivative responses, however, are more than those observed in Figs. 5-34 and 5-35 because of the difference in the reservoir heterogeneity as shown in Fig. 5-40. Figure 5-40 shows the log-log plot for the field and simulated data. It can be seen that the start of the oscillations at 3 hours of shut-in time coincides with the recession of a gas cap that develops during the production. They found that the oscillations corresponded to changes in gas saturation during the gas encroachment. The reservoir model in this study is a homogeneous system whereas the well tests discussed in Refs. 17 and 18 are from a naturally fractured reservoir. In general, the oscillations in the derivative responses increase as the degree of heterogeneity increases.

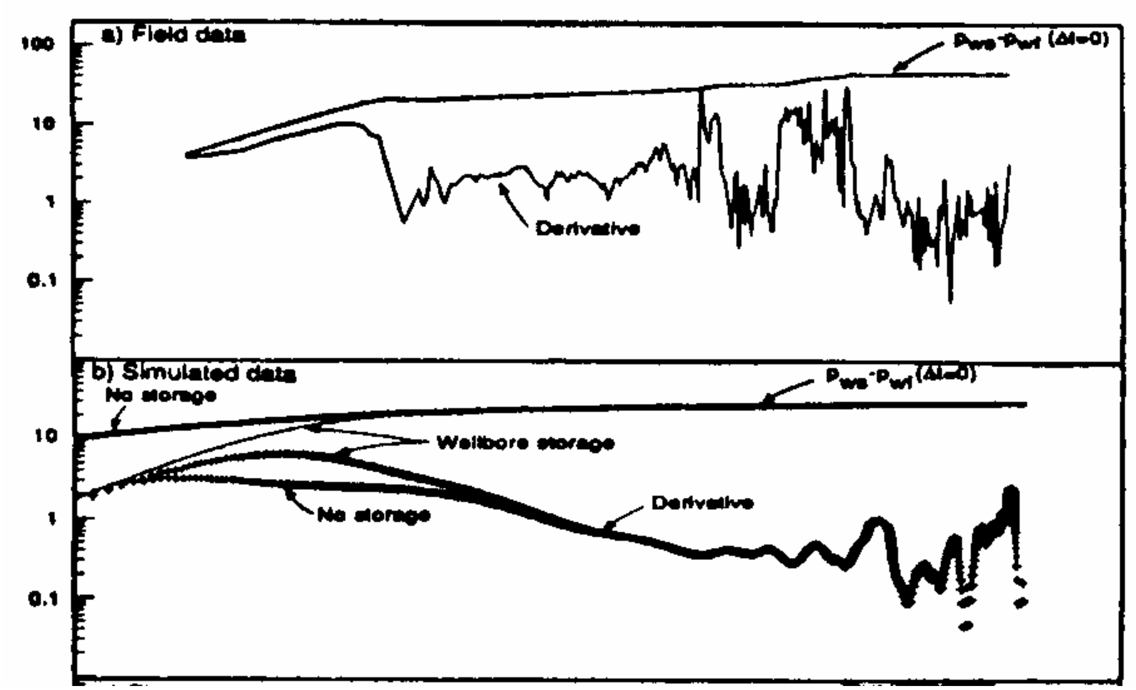

Figure 5- 40. Log-log plots of buildup pressure and derivative.[17-18]

Chapter 6

CONCLUSIONS AND RECOMMENDATIONS

The objectives of this study have been met through several tasks. The most important task was to find reliable representation of horizontal wells in numerical models to accurately simulate their pressure-transient behavior. Therefore, the conventional well indices and selection of time steps and grid refinements were studied and discussed. In addition, the application of transient well indices for horizontal wells were investigated and documented. The second important task was to study the pressure-transient responses of horizontal and curved wells in horizontal slab reservoirs and anticlines with and without gas cap. New results have been presented which should help to choose the appropriate models and the right assumptions for the pressure-transient analysis of such systems. Based on the results found in this study, several conclusions have been drawn and listed below.

1. For the simulation of horizontal well pressure-transient responses, log-distributed grid with 1 ft^2 y-z square wellblock should be used with the conventional well index to obtain closer match to the analytical solution at early times.

2. The selection of time-step does not affect the accuracy of the numerical model significantly.

3. Applying transient well index with coarse grids will improve the match with the analytical solution at early times. However, the use of fine grid has an adverse affect on the accuracy of the results with transient well index.

4. The results of the sensitivity runs show that the effect of the structure or gas encroachment becomes noticeable beyond the early-time radial flow where both transient well index and conventional well index yield accurate simulations.

5. The effect of the curvature and undulations of the well on the pressure-transient behavior is negligible unless the amplitude of the curvature is extremely large and approaching the upper of bottom boundaries. Thus, to analyze pressure-transient responses of curved and undulating wells, straight horizontal well models with an effective well length can be used. The effective well length is taken as the straight horizontal distance between the tips of the well. This conclusion is also valid in the presence of a gas cap and for finite wellbore conductivity.

6. Conventional single-phase flow horizontal well models for horizontal slab reservoirs can be used to analyze pressure-transient responses in anticlines and domes.

7. Two-phase numerical models should be used to interpret the pressure-transient responses of horizontal wells in slab reservoirs and anticlines in the presence of a gas cap.

8. For the pressure-transient analysis of horizontal wells, an anticline with a gas cap can be approximated by a horizontal slab reservoir with an equivalent gas cap volume of adjusted porosity.

9. Buildup responses of horizontal wells in the presence of a gas cap with long enough producing time for gas breakthrough display oscillations after the early-time radial flow. Under these conditions, detailed numerical models should be used for pressure buildup analysis of horizontal wells.

Based on this work, the following research is recommended for future investigations:

1. A numerical model should be developed to account for the gas in solution and gas condensate systems.

2. The effect of the ratio of the undulation amplitude to formation thickness should be documented and the maximum ratio for which the undulations can be ignored for pressure transient analysis purposes should be determined.

3. Potential of improving the transient well index by using the full horizontal well solution should be investigated.

4. The transient well index would allow larger well blocks. This should be extended to multiphase flow cases.

5. The use of corrected transmissibility and accumulation terms (CTAT) to improve horizontal well representation in numerical models should be studied.

NOMENCLATURE

A = area, ft^2.

b = reciprocal formation volume factor, scf/bbl.

B = formation volume factor, bbl/scf.

$\mathbf{c}$ = total compressibility, psi^{-1}.

C = wellbore storage coefficient, bbl/psia.

D = depth, ft.

f = friction factor.

h = reservoir thickness, ft.

HF = head loss friction, ft.

k = permeability, md.

k_r = relative permeability.

k_r^* = maximum relative permeability, md.

k_w = horizontal permeability in the normal direction of the well axis, md.

L = characteristic length in the system, ft.

L_h = horizontal well length, ft.

M_{wt} = molecular weight, lb/lb mole.

N_{max} = total number of time steps.

n_y = number of gridblocks in the y-direction.

n_z =number of gridblocks in the z-direction.

p = pressure, psia.

$\overline{p}$ = average pressure, psia.

p_{cog} = capillary pressure, psia.

P_{sp} = span pressure, psia.

P_{th} = threshold pressure, psia.

p_{wf} = flowing bottom-hole pressure, psia.

q = surface production rate, scf/d.

q_{wb} = wellbore loading/ unloading rate, bbl/d.

q_{sf} = sandface production rate, bbl/d.

r_b = radius of circle whose area is Δx × Δy, cm.

r_0 = equivalent wellbore radius, ft.

r_w = wellbore radius, ft.

$\tilde{r}$ = radial coordinate in the vertical plane (y-z) normal to the axis of the well, ft.

S = saturation.

s = skin.

s_z = pseudoskin.

t = time, hour.

T = temperature, ^{o}F.

u = sf(s).

v = velocity, ft/sec.

V = volume, ft^3.

WI = conventional well index, psia/bbl.

TWI = transient well index, psia/bbl.

x = distance in x-direction, ft.

y = distance in y-direction, ft.

z = distance in z-direction, ft.

z_w = horizontal well location, ft.

Z = gas compressibility factor.

Greek:

α = non-darcy coefficient.

$\hat{\alpha}$ = inverse of non-darcy coefficient.

ε_D = relative roughness of the well surface.

γ = density gradient, psi/ft.

ϕ = porosity, fraction.

μ = viscosity, cp.

ρ = density, lbm/ ft^3.

Δt = time step, hr.

ΔL = horizontal length, ft.

Δx = gridblock dimension in x-direction, ft.

Δy = gridblock dimension in y-direction, ft.

Δz = gridblock dimension in z-direction, ft.

Δt = time step, hr.

Subscript:

0 = wellblock location.

ϕ = formation.

b = base.

D = dimensionless.

e = external.

eq = equivalent.

g = gas.

i = x-direction.

j = y-direction.

k = z-direction.

n = old time.

n+1 = current time.

o = oil.

R = rock.

r = irreducible.

t = total.

well, w = wellbore.

x = x-direction.

y = y-direction.

z = z –direction.

REFERENCES

1. Peaceman, D.W.: ”Interpretation of Well-Block Pressures in Numerical Reservoir Simulation,” Transactions of AIME, 1978, 253.
2. Blanc, G., Ding, D.Y., Ene, A., Estebenet, T. and Rahon, D.: “Transient Productivity Index for Numerical Well Test Simulations,” in R. Schatzinger and J. Jordan, eds., Reservoir Characterization-Recent Advances, AAPG Memoir, 1999, 163.
3. Clonts, M. D. and Ramey, H. J., Jr.: “Pressure Transient Analysis for Wells with Horizontal Drainholes,” paper SPE 15116 presented at the 1986 California Regional Meeting, Oakland, CA, April 2-4.
4. Ozkan, E., Raghavan, R., and Joshi, S. D.: “Horizontal Well Pressure Analysis,” SPE Formation Evaluation (Dec. 1989), 567.
5. Goode, P.A., and Thambynayagam, R.K.M.: “Pressure Drawdown and Buildup Analysis of Horizontal Wells in Anisotropic Media,” SPE Formation Evaluation (Dec. 1987), 683.
6. Carvalho, R. S. and Rosa, A. J.: “A Mathematical Model for Pressure Evaluation in an Infinite-Conductivity Horizontal Well,” SPE Formation Evaluation (Dec. 1989) 567.

7. Kuchuk, F. J., Goode, P. A., Brice, B. W., Sherard, D. W., and Thambynayagam, R. K. M.: "Pressure-Transient Analysis for Horizontal Wells," Journal of Pet. Tech. (Aug. 1990) 974.

8. Kuchuk, F. J., Goode, P. A., Wilkinson, D. J., and Thambynayagam, R. K. M.: "Pressure-Transient Behavior of Horizontal Wells With and Without Gas Cap or Aquifer," SPE Formation Evaluation (March 1991), 86.

9. Ozkan, E. and Raghavan, R.: "Performance of Horizontal Wells Subject to Bottomwater Drive," SPE Reservoir Engineering (Aug. 1990), 375.

10. Ozkan, E. and Raghavan, R.: "New Solutions for Well-Test-Analysis Problems: Part 1 - Analytical Considerations," SPE Formation Evaluation (Sept. 1991), 359.

11. Ozkan, E. and Raghavan, R.: "New Solutions for Well-Test-Analysis Problems: Part 2 - Computational Considerations and Applications," SPE Formation Evaluation (Sept. 1991), 369.

12. Daviau, F., Mouronval, G., Bourdarot, G., and Curutchet, P.: "Pressure Analysis for Horizontal Wells," paper SPE 14251 presented at the 1985 SPE Annual Technical Conference and Exhibition, Las Vegas, Sept 22-25.

13. Odeh, A. S. and Babu, D. K.: "Transient Flow behavior of Horizontal Wells: Pressure Drawdown and Buildup Analysis," SPE Formation Evaluation (March 1990), 7.

14. Ozkan, E.: "Analysis of Horizontal Well-Responses: Contemporary vs. Conventional," SPE Reservoir Evaluation and Engineering (Aug. 2001), 260.

15. Azar-Nejad, F., Tortike, W. S., and Farouq Ali, S. M.: "Performance of Horizontal Wells with Irregular Geometry," paper SPE 36550 presented at the SPE Annual Technical Conference and Exhibition, Denver, CO, Oct. 6-9, 1996.

16. Goktas, B. and Ertekin, T.: "A Comparative Analysis of Pressure Transient Behaviour of Undulating and Horizontal Wells," paper SPE 81067 presented at the SPE Latin American and Caribbean Petroleum Engineering Conference, Port-of-Spain, Trinidad, West Indies, April 27-30, 2003.

17. Fleming, C. H., Perschke, D. R., Gilman, G. R., and Kazemi, H.: "Pressure Transient Testing of Horizontal Wells with an Overlying Gas Cap," paper SPE 28391 presented at the SPE Annual Technical Conference and Exhibition, New Orleans, LA, Sept. 25-28, 1994.

18. Fleming, C. H., Gilman, G. R., and Kazemi, H.: "Testing of Horizontal Wells with Overlying Gas Cap Journal of Pet. Tech (June 1996), 533.

19. Peaceman, D.W.: "Interpretation of Wellblock Pressures in Numerical Reservoir Simulation with Nonsquare Grid Blocks and Anisotropic Permeability," SPE Journal, June 1983, 513.

20. Babu, D.K., and Odeh, A.S.: "Productivity of a Horizontal Well," SPE Reservoir Engineering, Nov. 1989, 417.

21. Ding, Y. and Renard, G.: "A New Representation of Wells in Numerical Reservoir Simulation," SPE Reservoir Engineering, May 1994, 140.

22. Ding, Y., Renard, G., and Weill, L.: “Representation of Wells in Numerical Reservoir Simulation,” Paper SPE 29123 presented at SPE Symposium on Reservoir Simulation held in San Antonio, 12-15 Feb. 1995, 303.

23. Ding, Y.: “A Generalized 3D Well Model for Reservoir Simulation,” Paper SPE 30724 presented at SPE Annual Technical Conference and Exhibition held in Dallas, 22-25 Oct. 1995, 227.

24. G˙ Kta˙, B., and Ertekin, T.:” Implementation of a Local Grid Refinement Technique in Modeling Slanted, Undulating Horizontal and Multi-Lateral Wells,” Paper SPE 56624 presented at the SPE Annual Technical Conference and Exhibition held in Houston, Texas, 3-6 Oct. 1999.

25. Archer, Rosalind A., and Horne, Roland N.: ”The Green Element Method for Numerical Well Test analysis,” Paper SPE 62916 presented at the SPE Annual Technical Conference and Exhibition held in Dallas, Texas, 1-4 Oct. 2000.

26. Vicente, Ronlando, Sarica, C. and Ertekin, T.:” A Numerical Model Coupling Reservoir and Horizontal Well Flow Dynamics-Transient Behavior of Single-Phase Liquid and Gas Flows,” Paper SPE 65508 presented at the 2000 SPE Eastern Regional Meeting held in Morgantown, West Virginia, 17-19 Oct. 2000.

27. Archer, Rosalind A., and Yildiz, Tabiat T.: ”Transient Well Index for numerical Well Test Analysis,” Paper SPE 71572 presented at the SPE Annual Technical Conference and Exhibition held in New Orleans, Louisiana, 30 Sept.-3 Oct. 2001.

28. Dikken, B. J.: “Pressure Drop in Horizontal Wells and Its Effect on Production Performance,” JPT, Nov. 1990.
29. Suzuki, K.: “Influence of Wellbore Hydraulics on Horizontal Well Pressure Transient Behavior,” Paper SPE 24684 presented at the SPE Annual Technical Conference and Exhibition held in Washington, DC, Oct. 4-7, 1992.
30. Sarica, C., Ozkan, E., and Haciislamoglu, M.: “Influence of Wellbore Hydraulics on Pressure Behavior and Productivity of Horizontal Gas Wells,” Paper SPE 28486 presented at the SPE Annual Technical Conference and Exhibition held in New Orleans, LA, Sept. 25-26, 1994.
31. Ozkan, E., Sarica, C., Haciislamoglu, M. and Raghavan, R.: “Effect of Conductivity on Horizontal-Well Pressure-Behavior.” SPE Advanced Technology Series, Vol. 3, No. 1, March 1995, 85.
32. Ozkan, E., Sarica, C. and Haci, M.: “The influence of Pressure Drop along the Wellbore on Horizontal Well Productivity,” SPE Journal, Vol. 4, No. 3, Sept. 1999.
33. Ozkan, E. and Raghavan, R.: “ Estimation of Formation Damage in Horizontal Wells,” paper SPE 37511 presented at the Production Operation Symposium, Oklahoma City, OK, March 9-11, 1997.
34. Bentsen, R. G., and Anli, J.: “A New Displacement Capillary Pressure Model,” J. Cdn. Pet. Tech. (1976) 75.

35. Brooks, R. H., and Corey, A. T.: "Hydraulic Properties of Porous Media," Hydrology Papers, No. 3, Colorado State University, Ft. Collins, Colorado (1964).

36. Chaperon, I.: "Theoretical Study of Coning Toward Horizontal and Vertical Wells in Anisotropic Formations: Subcritical and Critical Rates," paper SPE 15377 presented at the SPE Annual Technical Conference and Exhibition, New Orleans, LA, Oct. 5-8, 1986.

37. Giger, F.: "Analytic 2D Models of Water Cresting before Breakthrough for Horizontal Wells," paper SPE 15378 presented at the SPE Annual Technical Conference and Exhibition, New Orleans, LA, Oct. 5-8, 1986.

38. Ozkan, E. and Raghavan, R.: "A Breakthrough Time Correlation for Coning toward Horizontal Wells," paper SPE 20964 presented at Europec 90, The Hague, The Netherlands, Oct. 22-24, 1990.

39. Umnuayponwiwat, S. and Ozkan, E.: "Water and Gas Coning toward Finite-Conductivity Horizontal Wells; Cone Build-up and Breakthrough," paper SPE 60308 presented at the SPE Rocky Mountain Regional/Low Permeability Reservoirs Symposium, Denver, CO. March. 12-15, 2000.